9-1-2015

THERMAL FATIGUE DAMAGE OF ASPHALT PAVEMENT

Md Islam

Student Name: Md Rashadul Islam
Candidate

Graduate Unit (Department): Civil Engineering
Department

This dissertation is approved, and it is acceptable in quality and form for publication:

Approved by the Thesis Committee:

Rafiqul A. Tarefder, Chairperson

Arup K. Maji, Member

Tang-Tat Ng, Member

Yu-Lin Shen, Member

THERMAL FATIGUE DAMAGE OF ASPHALT PAVEMENT

By

MD RASHADUL ISLAM

B.S. in Civil Engineering (2007)
Bangladesh University of Engineering and Technology (BUET), Dhaka, Bangladesh

Advanced Masters in Structural Analysis (2008)
University of Minho, Guimaraes, Portugal
Technical University of Catalonia, Barcelona, Spain

DISSERTATION
Submitted in Partial Fulfillment of the
Requirements for the Degree of
Doctor of Philosophy in
Engineering

The University of New Mexico
Albuquerque, New Mexico
July 2015

DEDICATION

To my wife, Jannatul Ferdous

ACKNOWLEDGMENTS

I cannot find enough words to express my deep and sincere gratitude to my supervisor, Professor Rafiqul A. Tarefder. Throughout the years to follow, Dr. Tarefder has been an exemplary guide, motivator, and mentor. Dr. Tarefder gave me confidence, opportunity and most importantly freedom in research. Dr. Tarefder's supervision is not limited to academic boundary of developing and execution of research; rather he is my role model in all aspects of my career.

I would like to express my sincere thanks to my dissertation committee members, Professor Arup Maji, Professor Percy Ng, and Professor Yu-Lin Shen for their valuable time, inputs and advice throughout my Ph.D. work. They helped me a lot to define my dissertation research topic. Their meticulous comments while my comprehensive examination gave me encouragements to perform such a cutting edge research.

I gratefully acknowledge the financial support from the New Mexico Department of Transportation (NMDOT) for conducting this research at the University of New Mexico (UNM). I also acknowledge the services of Civil Engineering Staff namely Rebekah Lucero, Brianne Lucero, Marcus Panozzo, Yolanda Sanchez, Nicole Bingham, Alicia Martinez and so on. I would also like to thank my colleagues and friends (especially, Mesbah, Mohi, Amina, Hasan, Asif and so on) who helped me to eventually get to this point; I will be forever grateful. Moral supports from Dr. Imran Hossain (Bradley University) are also appreciated.

THERMAL FATIGUE DAMAGE OF ASPHALT PAVEMENT

By

Md Rashadul Islam

B.S. in Civil Engineering (2007)

Bangladesh University of Engineering and Technology (BUET), Dhaka, Bangladesh

Advanced Masters in Structural Analysis (2008)

University of Minho, Portugal and Technical University of Catalonia, Spain

ABSTRACT

Fatigue damage can be defined by a decrease in stiffness of Asphalt Concrete (AC) under repeated traffic loading. For each cycle of traffic loading, tensile strain develops at the bottom of AC layer of an asphalt pavement. Some localized damages occur in the material at minute-scale due to this developed tensile strain. These damages cause decrease in stiffness (E) of AC. Damage caused by a single vehicle is small. However the accumulated damage is not small if a large number of vehicles are considered over the design life of an asphalt pavement. After certain level of damage accumulation, bottom-up fatigue cracking initiates and forms alligator cracking at the surface.

Like traffic loading, repeated day-night temperature cycle causes damages in AC. Damage due to a single day-night temperature fluctuation may be small. However the accumulated damage due to a large number of day-night temperature cycles may not be small. In this study, fatigue damage due to traffic loading is termed as traffic-induced fatigue damage, and fatigue damage due to temperature is termed as temperature-induced fatigue damage. The recently developed AASHTOWare Pavement Mechanistic-

Empirical (ME) Design Guide predicts the fatigue performance of AC based on repeated traffic-induced tensile strain at the bottom of AC layer. Cyclic thermal strain due to day-night temperature fluctuation is not considered due to the fact that there is no closed-form solution or model available for calculating thermal fatigue damage.

This study, for the first time, develops a closed-form equation for calculating the temperature-induced fatigue damage of AC. To develop the model, beam fatigue testing was conducted using different AC mixtures in the laboratory. The mechanical beam fatigue test data was correlated with the actual cyclic temperature loading test data. The model was then validated using an unknown test data. To that end, the developed model was calibrated for field conditions using the Falling Weight Deflectometer (FWD) test data. The developed model is used to evaluate fatigue damages of 34 Long-Term Pavement Performance (LTPP) test sections.

Fatigue damage predicted by the traditional AASHTOWare Pavement ME Design approach, which considers only traffic-induced fatigue damage, is compared to the fatigue damage by the developed model which considers both traffic- and temperature-induced fatigue. Results show that the error may decrease by up to 29% through the incorporation of temperature-induced fatigue damage in the AASHTOWare Pavement ME Design approach. This means the reliability of alligator cracking prediction can be improved through the use of the developed thermal fatigue model. It is therefore suggested to include the temperature-induced fatigue damage model, which is developed in this study, in the AASHTOWare Pavement ME Design Software.

TABLE OF CONTENTS

ACKNOWLEDGMENTS v
ABSTRACT vi
LIST OF FIGURES xii
LIST OF TABLES xiv
CHAPTER ONE 1
INTRODUCTION 1
1.1 Problem Statement 1
1.2 Hypothesis 2
1.3 Objectives and Scopes 4
1.4 Organization 6
CHAPTER TWO 8
LITERATURE REVIEW 8
3.1 General 8
3.2 Temperature-Induced Fatigue Damage 8
3.3 Asphalt Boundary Condition 15
3.4 Coefficients of Thermal Expansion and Contraction (α-value) 17
3.5 Determining Temperature at the Bottom of Asphalt 21
3.6 Thermal Strain 26
3.7 Development of Traffic-Induced Fatigue Model 27
3.7.1 Calibration of Regression Coefficients 27
3.7.2 Determining Damage Shift Factor 29
CHAPTER THREE 31
DETERMINING THERMAL STRAIN 31
3.1 General 31
3.2 Determining α-Value 31
3.2.1 Background 31
3.2.2 Calibration of Linear Variable Displacement Transducer 31
3.2.3 Sample Collection and Preparation 34
3.2.4 Testing 35

3.2.5 Results and Discussion 36
3.3 Further Study on α-value 38
3.3.1 Investigating the Effect of Cross-Anisotropy 38
3.3.1.1 Sample Collection and Preparation 39
3.3.1.2 Testing 39
3.3.1.3 Results and Discussion 40
3.3.2 Investigating the Effect of Air Void 41
3.3.2.1 Sample Collection and Preparation 41
3.3.2.2 Testing 42
3.3.2.3 Results and Discussion 42
3.3.3 Investigating the Effect of Aggregate Type 44
3.3.3.1 Sample Collection and Preparation 44
3.3.3.2 Testing 45
3.3.3.3 Results and Discussion 46
3.3.4 Investigating the Effect of Aggregate Gradation 48
3.3.4.1 Sample Collection and Preparation 48
3.3.4.2 Testing 49
3.3.4.3 Results and Discussion 50
3.4 Discussion on α-value 52
3.5 Determining Temperature Fluctuation 53
3.5.1 Developing Regression Models 53
3.5.1.1 Sensors Installation 53
3.5.1.2 Data Collection 54
3.5.1.3 Analysis 55
3.5.1.3.1 Temperature Variations 55
3.5.1.3.2 Predicting the Maximum Temperature 56
3.5.1.3.3 Predicting the Minimum Temperature 58
3.5.1.3.4 Predicting the Average Temperature 59
3.5.1.3.5 Model Validation 60
3.5.1.3.6 Discussion 62
3.5.2 Discussion on Determining Temperature Fluctuation 62
CHAPTER FOUR 63

TEMPERATURE-INDUCED FATIGUE MODEL DEVELOPMENT 63
4.1 General 63
4.2 Materials 64
4.3 Sample Preparation 66
4.4 Sample Volumetric Properties 66
4.5 Determining Equivalent Laboratory Test 67
4.6 Laboratory Testing 72
4.6.1 Frequency of Loading 74
4.6.2 Stiffness of Samples 78
4.7 Test Results and Model Development 79
CHAPTER FIVE 81
MODEL VALIDATION/CALIBRATION 81
5.1 General 81
5.2 Laboratory Validation/Calibration 81
5.2.1 Material 81
5.2.2 Sample Preparation 82
5.2.3 Testing 82
5.2.4 Results and Discussion 83
5.3 Field Validation/Calibration 83
5.3.1 Calibration Procedure 84
5.3.2 Determining Field Damage Index 84
5.3.3 Results 85
5.3.4 Calculating Laboratory Damage Ratio 87
5.3.5 Determining the Shift Factor 88
CHAPTER SIX 90
MODEL TESTING 90
6.1 General 90
6.2 Alligator Cracking Prediction Procedure 90
6.3 Model Application Procedure in the AASHTOWare Design Guide 92
6.4 Collecting Measured Cracking Data 97
6.5 Analysis of Predicted and Measured Cracking Data 101
CHAPTER SEVEN 107

CONCLUSIONS AND RECOMMENDATION 107
7.1 General 107
7.2 Conclusions 107
7.3 Recommendations for Further Study 109
REFERENCES 111
APPENDIX A 122
SAMPLE CALCULATION FOR DETERMINING ALLIGATOR CRACKING INCLUDING THERMAL FATIGUE DAMAGE 122
APPENDIX B 130
LTPP DATA FOR CHOSEN PAVEMENT SECTION 130
APPENDIX C 144
MEASURED AND PREDICTED ALLIGAOTR CRACKING DATA 144
APPENDIX D 150
DETERMINING THERMAL PROPERTIES OF ASPHALT CONCRETE 150
BIOGRAPHY 160

LIST OF FIGURES

Figure 1. Fatigue cracking in an asphalt pavement 2
Figure 2. Research methodology 6
Figure 3. Research procedure to compare temperature- and traffic-induced damages 11
Figure 4. Temperature and horizontal strain variations at the bottom of AC. 14
Figure 5. Thermal expansion and contraction on restrained AC sample 15
Figure 6. Boundary condition of asphalt concrete in pavement 17
Figure 7. Comparisons of measured temperature with other studies 25
Figure 8. Calibration of the LVDTs 32
Figure 9. Contraction mechanism of LVDT due to increase in temperature 33
Figure 10. CTC and CTE of LVDTs 34
Figure 11. Sample collection and preparation 35
Figure 12. Measuring the expansion-contraction due to temperature change 36
Figure 13. Temperature-dependent α-value 37
Figure 14. Measuring the thermal expansion-contraction (Vertical Direction) 39
Figure 15. Cross-anisotropic CTC and CTE values with temperature 41
Figure 16.Variations of the CTC and the CTE values with AV 43
Figure 17. Gradation of AC containing different aggregate types 45
Figure 18.CTC values with aggregate type 46
Figure 19.CTE values with aggregate type 48
Figure 20. 0.45 power charts of the three mixtures 49
Figure 21.CTC values with aggregate gradation 50
Figure 22.CTE values with aggregate gradation 51
Figure 23. Installed weather station 54
Figure 24. Installation of temperature probes 54
Figure 25. Temperature variations over the day on October 24, 2012 56
Figure 26. Predicted and measured temperatures at 50 mm depth of AC 60
Figure 27. Predicted and measured temperatures at 100 mm depth of AC 61
Figure 28. Schematic of fatigue test result 63
Figure 29. Gradations of aggregates used in AC 65
Figure 30. Beam sample preparation 66
Figure 31. Test scheme versus the ideal test setup 68
Figure 32. Correlation between the actual temperature and mechanical loading 69
Figure 33. Beam fatigue (mechanical) versus axial thermal fatigue damage 72
Figure 34. Four-point bending test 74
Figure 35. Effect of loading frequency on the fatigue life of AC 75
Figure 36. Decrease in stiffness for testing at 0.01 Hz and 1.16×10^{-5} Hz (20 °C) 76
Figure 37. Decrease in stiffness for testing at 0.01 Hz and 1.16×10^{-5} Hz (12 °C) 77
Figure 38. Decrease in stiffness with number of loading at 500 με 79
Figure 39. Beam fatigue test results for the three mixtures 80
Figure 40. Gradation of the mixture used for laboratory validation 82

Figure 41.Conduction of FWD test on I-40 pavement..... 85
Figure 42. Decrease in shoulder stiffness due to thermal fatigue loading 86
Figure 43. Methodology to determine the contribution of the developed model..... 96
Figure 44. US States from where LTPP sections were chosen (circled) 98
Figure 45. Number of section with cracking amount..... 99
Figure 46. Measured cracking data with AC thickness 99
Figure 47. Measured cracking data with the MATT..... 100
Figure 48. Standard error (prediction minus the measured cracking data)..... 102
Figure 49. Prediction of alligator cracking versus the measured cracking data..... 103
Figure 50. Prediction of alligator cracking versus the LTPP measured data 104
Figure 51. Prediction of cracking using the proposed cracking model (Eq. 35)..... 106

LIST OF TABLES

Table 1. *p*-values of multiple comparison tests using FSD method 26
Table 2. Damage shift factor used in damage ratio 30
Table 3. Measured CTC and CTE values at different temperature ranges 37
Table 4. *p*-values of the CTC/CTE of AC with different AVs 44
Table 5. *p*-values of the CTC/CTE of SP-III AC with different aggregates 47
Table 6. *p*-values of the CTC/CTE of a basalt mixture with different gradations 51
Table 7. Materials used to develop the model 64
Table 8. Test matrix 73
Table 9. Laboratory validation of the developed model 83
Table 10. Calculating laboratory damage ratio due to thermal fatigue loading 88
Table 11. Optimizing the cracking model (Eq. 35) to minimize the error 105

CHAPTER ONE

INTRODUCTION

1.1 Problem Statement

Fatigue damage is defined by the decrease in stiffness of Asphalt Concrete (AC) under repeated loading. Most of the past studies addressed fatigue damage due to repeated traffic loading (AASHTO 2008, Huang 2004, NCHRP 2004, Schwartz et al. 2013, Carvalho and Schwartz 2006, El-Basyouny and Witczak 2005a,b). Tensile strain develops at the bottom of AC of asphalt pavement when traffic wheel passes over AC. Some minute-scale damages occur due to this developed tensile strain. Under repeated traffic loading, micro-scale damage due to repeated tensile strain causes a decrease in AC material's stiffness (E). The damage is accumulated in AC over the design life of asphalt pavement. After certain level of damage accumulation, bottom-up fatigue cracking initiates, propagates through the AC layer, and shows at the surface as an alligator cracks (see Fig. 1). A network of fatigue cracks on the actual pavement surface looks like an alligator skin and therefore, fatigue cracking is also known as alligator cracking, as shown in Fig. 1(b).

Like traffic loading, repeated temperature cycle may cause some damages in AC. In places like New Mexico, the day-night air temperature difference is about 35 °F for many days (cycles) in a year. Damage due to one day-night temperature fluctuation may be small, but the accumulated damage due to a large number of day-night temperature cycles may not be small. This study hypothesized that the damage due to repeated day-night temperature cannot be neglected. In this study, fatigue damage due to traffic is termed as

traffic-induced fatigue damage, and fatigue damage due to temperature is termed as temperature-induced fatigue damage. While repeated cycles of temperature accumulates damages, it is possible that one cycle of temperature may cause significant amount of damage simply due to temperature induced strain reaches materials strength (strain). This aspect of temperature induced failure or crack can be counted separately, but not as temperature-induced fatigue damage.

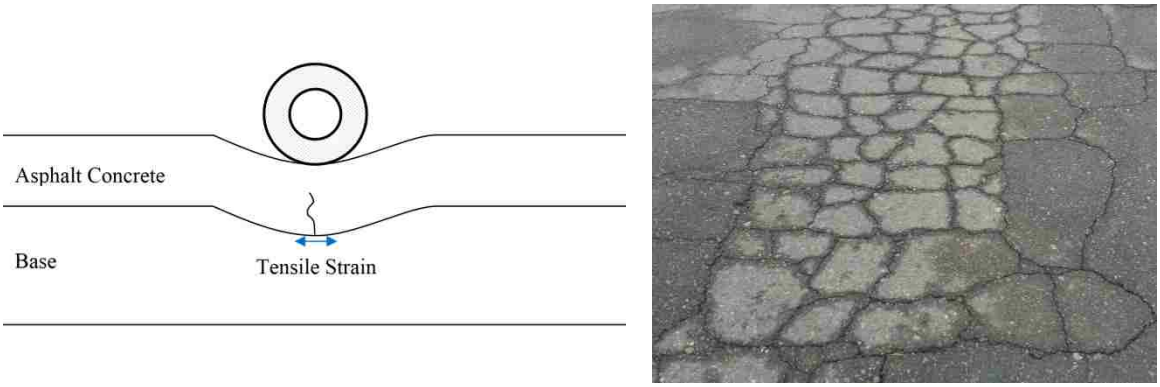

a) Tensile strain at the bottom of AC

b) Fatigue cracking in a pavement in the UNM campus

Figure 1. Fatigue cracking in an asphalt pavement

1.2 Hypothesis

In pavement design, the traffic-induced fatigue damage is calculated by dividing the actual number of traffic load (n) by the allowable number of traffic load, N_{fv} that an AC material can withstand by the following relationship (AASHTO 2008):

$$D_1 = \sum_{i=1}^{p} \sum_{j=1}^{m} \frac{n_{i,j}}{N_{fv,i,j}} \quad (1)$$

where D_1 is the damage ratio or damage index for specific traffic *n*, *n* is the number of load repetitions for axle type *j* in period *i*, N_{fv} is the allowable number of load repetitions, *p* is the number of seasons in each year and *m* is the number of axle groups. The allowable number of load repetition, N_{fv} is determined by the following relation (AASHTO 2008):

$$N_{fv} = 0.007566(10^{M})C_H(\frac{1}{\varepsilon_t})^{3.9492}(\frac{1}{E})^{1.281} \quad (2)$$

$$M = 4.84(\frac{V_b}{V_a + V_b} - 0.69) \quad (3)$$

where ε_t = tensile strain at bottom of AC at critical location; E = stiffness[1] of the AC; C_H = thickness correction factor; V_b = percent effective binder content and V_a = percent air void. It can be noted that while Eq. 2 is available for the traffic-induced fatigue damage, such equation does not exist for the temperature-induced fatigue damage, which is the main topic of discussion here.

It is hypothesized that temperature-induced fatigue damage can be measured and used in pavement reliability for better reliability of the prediction of the alligator cracking. If alligator cracking is predicted using Eqs. (1-3), there is always a discrepancy between the predicted and field measured values, which requires to calibrate the model to local conditions. This discrepancy can be reduced by using temperature-induced fatigue

[1] AC's dynamic modulus and stiffness are synonymous and therefore, they are used interchangeably in this study.

damage and traffic-induced fatigue damage. The functional form of temperature-induced fatigue damage equation is proposed following Eq. (2) as below:

$$N_{ft}=f(E, \varepsilon) \tag{4}$$

where N_{ft} is the allowable number of day-night temperature fluctuation that AC material can withstand before showing cracking; ε is the thermal strain at the bottom of AC due to day-night temperature difference; E is the stiffness of the AC material which depends on the temperature and frequency of temperature fluctuation.

It is known that thermal strain (ε) in AC can be expressed as:

$$\varepsilon = \alpha(\Delta T) \tag{5}$$

where α is the coefficient of thermal contraction and expansion of AC material; ΔT is the day-night temperature difference. Here, α-value is defined as the average of the Coefficient of Thermal Contraction (CTC) and the Coefficient of Thermal Expansion (CTE).

1.3 Objectives and Scopes

The main objective of this study is to develop a closed form equation or model to calculate the thermal fatigue damage in asphalt pavement. To achieve this objective, the following tasks are accomplished:

a) Measure CTC and CTE values of asphalt concrete in the laboratory.
b) Develop a regression model to determine temperature at any depth of AC given the pavement surface temperature.
c) Develop a fatigue model to determine the fatigue life of asphalt concrete under the temperature-induced fatigue damage.
d) Validate the developed temperature-induced fatigue model in the laboratory.
e) Calibrate the developed temperature-induced fatigue model under field conditions.
f) Evaluate the developed fatigue model using data available in the Long-Term Pavement Performance (LTPP) database, which were not used in model development.

The detailed research methodology is presented by a flow chart in Fig. 2. The major research task lies in developing the model described by Eq. (4). The second major task is to develop Eq. (5) to determine the thermal strain. To develop so, α-value is determined in the laboratory first. Then, a regression model to determine the day-night temperature fluctuation at any depth of AC is developed. Using the thermal strain value determined following the above procedure, laboratory fatigue test is conducted on three mixtures. Based on the laboratory test data, a regression model is developed to determine the fatigue life of AC under day-night temperature fluctuation. This model is then calibrated using the Falling Weight-Deflectometer (FWD) data for field compatibility. The contribution of the developed model is evaluated by comparing the alligator cracking prediction with the measured field data available in the LTPP database. Bottom up

alligator cracking predicted using the AASHTOWare Pavement ME Design approach, which considers traffic-induced fatigue damage only, is compared to that by the combined traffic- and temperature-induced fatigue.

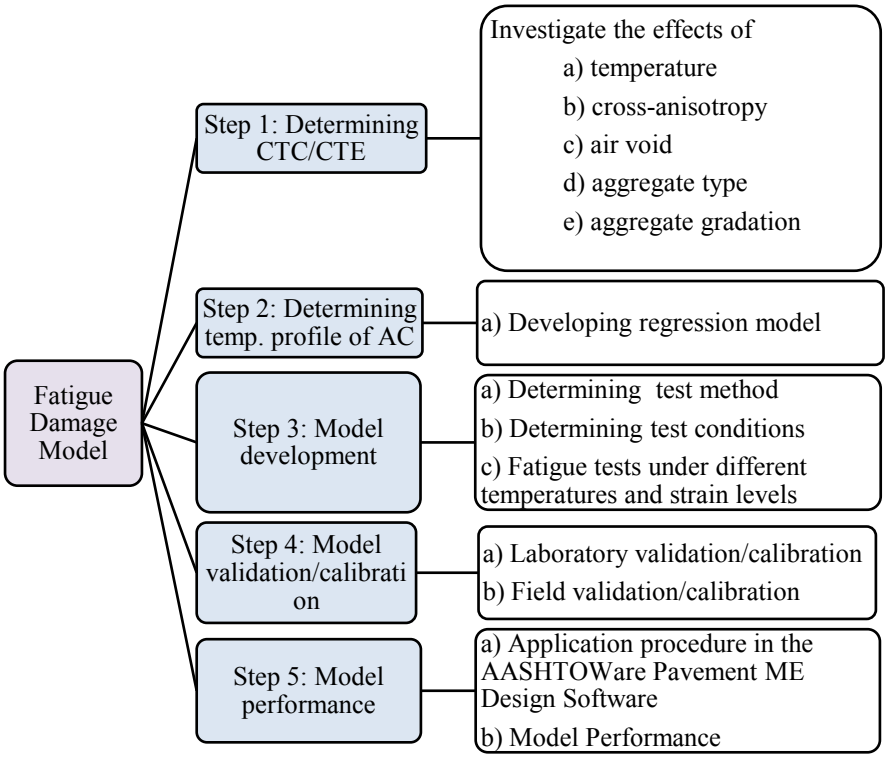

Figure 2. Research methodology

1.4 Organization

The organization of the dissertation can be described as follows:

Chapter One. It presents the problem statement, hypothesis and research objectives.

Chapter Two. The current pool of literature on the subject area is presented in Chapter Two.

Chapter Three. It deals with the procedure to determine the thermal strain at the bottom of AC. It presents the CTC and the CTE values of AC. It also presents the regression model to determine the temperature fluctuation at any depth of AC.

Chapter Four. It presents the laboratory testing to gather the test data which was used to determine the temperature-induced fatigue model.

Chapter Five. It deals with the model validation in the laboratory and model calibration under field conditions.

Chapter Six. The performance of the model is evaluated in this chapter.

Chapter Seven. It summarizes the findings of the study. Recommendations for future studies are also listed.

CHAPTER TWO

LITERATURE REVIEW

3.1 General

In this chapter, literature related to temperature-induced fatigue damage of AC is documented. Several studies attempted to develop such a model. However, most of those attempts were unsuccessful. The AC is considered fixed to the base layer in the current study; the researchers behind this consideration are also described. In addition, the developmental procedure of the traffic-induced fatigue damage which is currently being used is discussed.

3.2 Temperature-Induced Fatigue Damage

The concept of thermal fatigue damage in asphalt pavement is pretty old. Shahin and McCullough (1974) proposed the thermal fatigue model as follows:

$$N = k_1 \left(\frac{1}{\varepsilon} \right)^{k_2} \tag{6}$$

where N is the allowable load repetitions to cause fatigue cracking under thermal strain, ε and k_1 and k_2 are the regression constants based on constant strain test. They did not perform any laboratory test to develop the model; rather they assumed the regression constants. The model was validated based on the measured transverse cracking data from Ontario Test Roads and Ste. Anne Test Road. The model was not correlated with the alligator cracking data. However, the researchers did not report the values of the regression constants. In fact, accurate values of these two constants are unknown. In

addition, the allowable load repetition (N) as a function of stiffness of AC was not included in that model.

Huang (2004) described the model proposed by Shahin and McCullough (1974). As Shahin and McCullough (1974) did not report the values of the regression constants, Huang (2004) suggested using the traffic-induced fatigue model available in the literature as a replacement of the temperature-induced fatigue model. However, traffic-induced fatigue model should not be used in place of the temperature-induced fatigue model because there is a difference in frequency value between traffic loading and temperature loading.

Arabzadeh et al. (2015) presented thermal fatigue damage behavior of AC based on uniaxial fatigue testing on asphalt sample using mechanical loading. In that study, an experimental setup was developed in order to measure the thermal fatigue resistance of AC under strain-controlled testing. Different aggregates, gradations, asphalt binders and asphalt contents were studied. Uniaxial loading was mechanically applied to achieve constant amplitude sinusoidal strain at a frequency of 0.01Hz to simulate thermal fatigue behavior of AC. The strain amplitudes were determined using the measured thermal coefficients of the test specimens and the temperature differential corresponding to the climate of the city of Ankara. They studied the effects of aggregate type, gradation, binder etc. in fatigue resistance of AC. No temperature-induced fatigue model was developed in that study.

Tarefder and Islam (2013) measured traffic and temperature-induced fatigue damages using laboratory developed fatigue models for a pavement section on Interstate 40 (I-40) in the city of Albuquerque in the State of New Mexico in United States. The specific objectives of that study are mentioned below:

a) Predicting fatigue life (and damage) of I-40 pavement due to traffic loading based on laboratory developed fatigue model using the field measured stiffness and counted traffic.
b) Determining damage for temperature induced strain at the bottom of AC using the developed fatigue model for thermal load. Horizontal strains at the bottom of AC due to both diurnal and annual temperature fluctuations were considered.
c) Compare the above determined vehicle and thermal induced damages and evaluate the contribution of thermal strain in fatigue life of AC.

The work procedure to compare both vehicle and thermal induced damage is presented in Fig. 3. Firstly, fatigue life of I-40 pavement was predicted for vehicle load only which was the procedure of the AASHTOWare Pavement ME Design. Then, damages for diurnal and yearly thermal strains were included with vehicle induced damage. The contributions of vehicle, daily and yearly transverse longitudinal horizontal strains in the fatigue damage of AC were then evaluated.

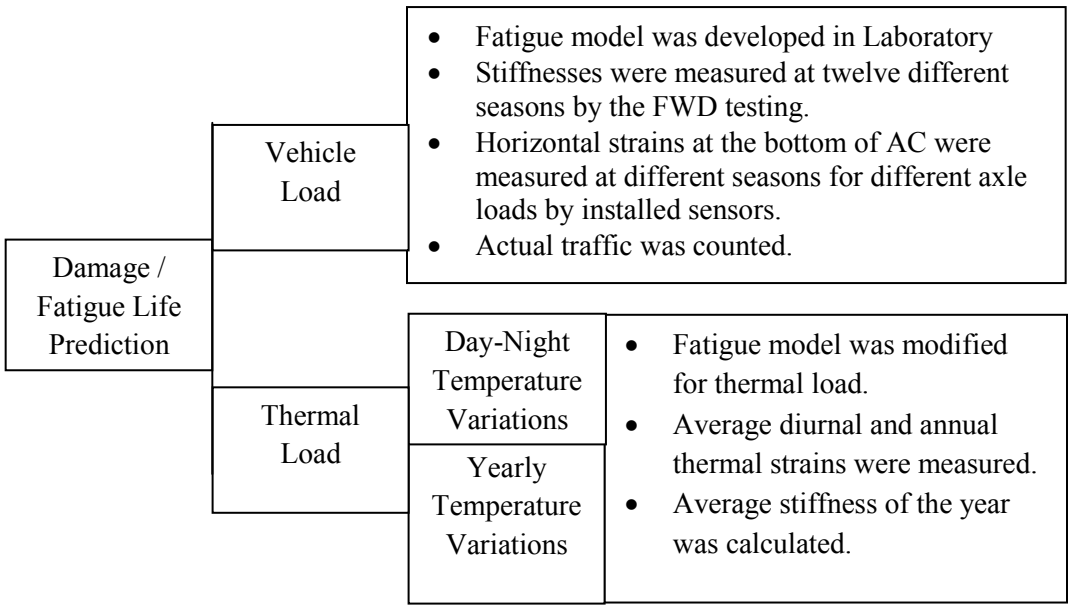

Figure 3. Research procedure to compare temperature- and traffic-induced damages

As a first step, fatigue life prediction models were developed for both vehicle and thermal loads based on stiffness and strain of AC collected from the I-40 section in New Mexico. A total of fourteen samples were tested at seven different strain levels at 20 °C to develop traffic-induced fatigue model. In the second step, traffic and thermal strains at the bottom of AC were measured by the Horizontal Asphalt Strain Gauges (HASGs). In the third step, using these strain values, fatigue damage at the bottom of asphalt concrete was determined. Both day-night and yearly temperature induced strains were considered. The laboratory developed model at a single temperature was used to determine the allowable number of load for different seasons. The laboratory test must have been conducted at different temperatures to account the seasonal effect. In addition, no calibration factor was determined to transfer the laboratory model to field condition. Another limitation of that study is that the temperature-induced fatigue model was assumed based on fatigue

test using three beams samples only. That study was also limited to a single pavement in New Mexico.

Islam et al. (2014a) compared traffic versus temperature-induced fatigue damages using the AASHTOWare Pavement ME Design fatigue model (Eq. 2) for the pavement section on I-40 in New Mexico. The traffic model provided by the AASHTOWare Pavement ME Design was used for both traffic- and temperature-induced fatigue damages following the recommendation of Huang (2004). The developed strains under traffic and temperature loading were determined using installed strain gauges at the bottom of AC. It was found that temperature produces a major portion of the total fatigue damage for the specific pavement site in New Mexico. The limitation of that study was that traffic-induced fatigue model was used for temperature-induced fatigue model. This is not appropriate as the frequencies of traffic and temperature loads are not equal. Separate fatigue model was required for determining temperature-induced fatigue damage.

Islam and Tarefder (2014a) separated thermal fatigue damage at the bottom of an asphalt concrete and hence, the fatigue life of asphalt concrete of I-40 pavement. Both the traffic- and temperature-induced fatigue models were developed testing at different temperatures. In addition, the effect of loading frequency on temperature-induced fatigue model was considered by testing at different frequencies and extrapolated for daily and yearly temperatures' frequencies. In the first step, fatigue damage of I-40 pavement was predicted for vehicle load only, which is the procedure of the AASHTOWare Pavement ME Design Guide to determine the fatigue life of AC. The fatigue model was developed

in the laboratory using beam fatigue testing. The developed model had input parameters of AC modulus and tensile strain at the bottom of AC. A shift factor was applied to the developed model to transfer the model from laboratory to field performance.

To determine AC moduli, firstly, the monthly average AC temperature was measured at twelve different months. Then, beam flexure tests (around 100 cycles) were conducted at these temperatures to determine the initial stiffness at twelve different months. Transverse horizontal tensile strains at the bottom of the AC were measured at different seasons for different axle loads from December 2012 to November 2013 by the HASGs. The transverse horizontal strain was considered instead of the longitudinal one as the transverse strain is 20% greater than the longitudinal strain (Islam and Tarefder, 2013a). The total traffic number for the year was determined from the data of installed Weigh-in-Motion (WIM) Data. Finally, fatigue damage due to traffic load was determined for one year of traffic loading.

In the second method, fatigue damages due to day-night and yearly longitudinal thermal strains were determined. Fatigue models were developed for both day-night and yearly thermal loads. The vehicle induced fatigue model could be used for predicting temperature induced fatigue damage, as the frequency of the thermal load is much smaller than that of the vehicle load. The fatigue model for day-night and yearly temperature cycles were different as each has different magnitude and frequency of loading. The developed model has an input parameter of frequency of loading only. Average day-night and yearly thermal strains are measured from December 1, 2012 to

December 31, 2013 using the HASGs as shown in Fig. 4. Fatigue damages due to day-night and yearly temperature-induced loads are determined for one year of day-night and yearly temperature cycles and results were compared with vehicle-induced damage obtained from the first method. Results showed the importance of thermal fatigue damage; however, there were still some limitations in that study such as field calibration, data extrapolation etc.

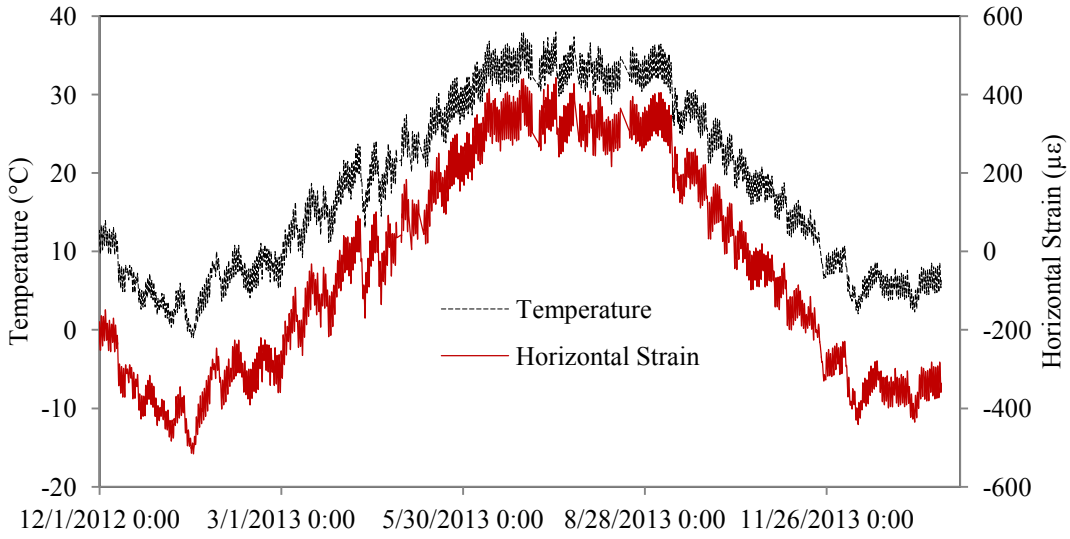

Figure 4. Temperature and horizontal strain variations at the bottom of AC.

In the revised study, Islam and Tarefder (2015a) developed a closed-form equation or model of temperature-induced fatigue damage of AC. To generate data, beam fatigue testing was conducted on three Superpave mixtures in the laboratory. The developed model was then used to evaluate fatigue damages of the several LTPP test sections. Fatigue damage determined by the traditional AASHTOWare Pavement ME Design approach (which considers traffic-induced fatigue damage only) was compared to that by

the combined traffic- and temperature-induced fatigue. Results showed that the error decreased by 31% through the incorporation of temperature-induced fatigue damage in the AASHTOWare Pavement ME Design approach.

The above discussion concludes that there is no well-established temperature-induced fatigue model in the literature to be accounted for alligator cracking. This reason motivated the author to develop temperature-induced fatigue model.

3.3 Asphalt Boundary Condition

It is important to investigate the research related to asphalt's boundary condition in real pavement. This is important to design a suitable test condition in the laboratory. If temperature changes occur in free asphalt samples, no damage is expected as the material expands and contracts freely. However, if cyclic temperature changes occur in restrained samples, repeated thermal stress will be developed inside the material as the material cannot expand and contract freely. Therefore, fatigue damage will occur if cyclic temperature change is applied to restrained samples. This can be explained by Fig. 5.

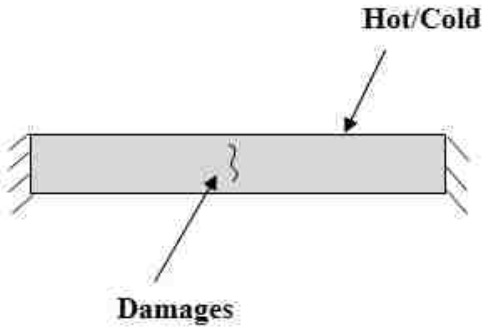

Figure 5. Thermal expansion and contraction on restrained AC sample

Past studies analyzed the pavement section under different boundary conditions. Zubeck and Vinson (1996) developed deterministic and probabilistic models to predict low-temperature cracking of asphalt concrete mixtures with the Thermal Stress Restrained Specimen Test (TSRST) results. In the TSRST test, the sample is fully restrained at the ends. This is because the field slab is considered full restrained. In fact, the calculation of the crack spacing is based on the theory that the pavement slab cracks when the pavement temperature reaches the cracking temperature of the mixture and the slab is fully restrained.

Kirkner and Shen (1999) developed the so called Fictitious Crack Model (FCM) to predict thermal cracking of asphalt pavements. They assumed the interface friction between the asphalt concrete and underlying layer is fixed and governed by the Coulomb's friction law. Frictional Restraint Model (FRM) was developed by Marastenu et al. 2004 and Timm et al. 2003 with the assumption that AC layer is free at one end and free at the other end. They also assumed that the AC layer is supported on elastoplastic foundation with frictional resistance. Rajbonshi and Das (2009) determined the crack spacing of transverse cracking of AC for single low temperature cracking using the same boundary conditions.

Recently, Al-Qadi et al. (2010) performed 3-D dynamic finite element analysis by using an implicit algorithm to simulate FWD test results using the fully bonded asphalt-base interface. Appea (2003) used same fully bonded asphalt-base interface to validate his model with the field instrumentation data. In another study, an axisymmetric model was

developed to determine the response of an instrumented pavement section under dynamic load by Howard and Warren (2009). They also used full restrained boundary conditions for all layers. From the above discussion, it can be concluded that any segment of asphalt concrete is fixed to the underneath base course, one end free and another end fixed as shown in Fig. 6. The free boundary condition typically arises from the construction joint or the accidental weakest point of pavement.

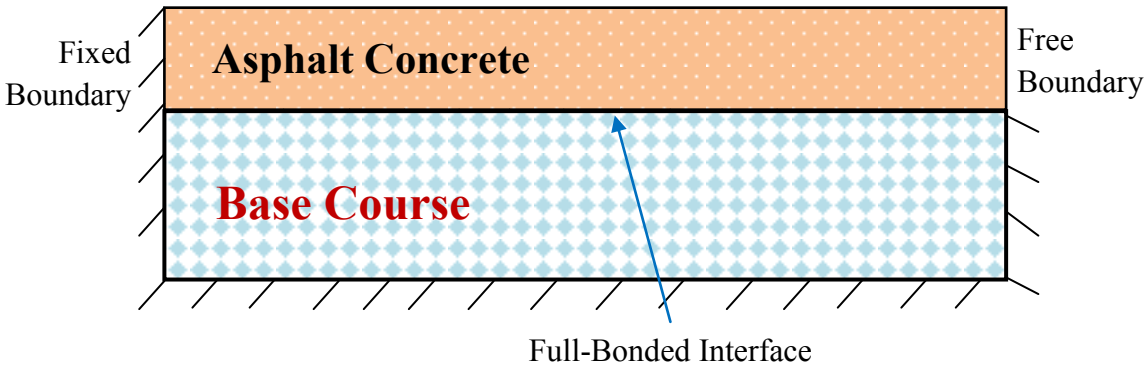

Figure 6. Boundary condition of asphalt concrete in pavement

3.4 Coefficients of Thermal Expansion and Contraction (α-value)

The α-value is essential to determine the thermal strain caused by temperature fluctuation as shown in Eq. 5. In one-dimensional (ID) material, if there is a temperature change (ΔT), the material elongates. Thus, α-value reports change in length due to unit change in temperature. More preciously, α-value is the strain per degree change in temperature.

Several studies were conducted in the past to study the CTC and the CTE of AC. Stoffels and Kawanda (1996) patched resistive strain gauges on cylindrical samples of 152.4 mm diameter and 51 mm thick to measure the decrease in sample diameter due to the

temperature decrease from 0 °C to -25 °C. Field collected cylindrical samples from different highway sections were tested. The CTC value was reported to be $1.33x10^{-5}$ to $2.97x10^{-5}$ per ˚C in the horizontal direction (perpendicular to the direction of compaction). It was observed that the measured strain varied linearly with temperature; the CTC value was not affected significantly by gauge position, gauge orientations and type of material.

Metha et al. (1999) used Linear Variable Differential Transformers (LVDTs) to determine the CTC of cylindrical core samples of 150 mm diameter 50 mm thick from 0 ˚C to -25 ˚C. The CTC value was reported to be $1.58x10^{-5}$ to $2.33x10^{-5}$ per ˚C. The researchers followed the work of Stoffels and Kawanda (1996) except they used LVDTs instead of resistive strain gauges.

Zeng and Shiels (1999) used AC beams of 51 mm x 51 mm x 340 mm dimensions and tested between -40 °C and +40 °C. The LVDTs were attached outside the environmental chamber. Based on a single asphalt mixture, the CTC and the CTE values were determined to be $1.35x10^{-5}$ and $2.62x10^{-5}$ per ˚C respectively. The researchers explored the effect temperature on the CTC and the CTE values and concluded that assumption of thermal linearity is not appropriate.

Mamlouk et al. (2005) used beam samples of 50 mm x 50 mm x 390 mm (field and laboratory compacted) inside an environmental chamber and the LVDTs were placed outside the chamber using rubber plug. The temperature range was 0 °C to 60 °C. The

CTC and the CTE values were determined to be 3.745×10^{-5} and 3.786×10^{-5} per ˚C respectively. The researchers used different types of materials (air voids ranged between 3.6 and 8.0 %.) and finally, concluded that the thermal coefficient values were dependent on material type. However, they did not correlate the changes of the CTC and the CTE values with material type and the large variation of air voids might have caused the variations in the results.

Xu and Solaimanian (2008) determined the CTC and the CTE values on cylindrical samples in the temperature range of -5 ˚C to 40 ˚C. Cylindrical specimens were subjected to temperature variations in an environmental chamber and specimen deformations were measured using extensometers. A finite element model was developed to simulate the thermal stresses and strains inside the specimen to evaluate the measured the CTC and the CTE. That study determined the CTC and the CTE values along the vertical direction.

Several researchers evaluated the effects of the aggregate type and its percentage on the CTC and the CTE values of Portland Cement Concrete (PCC) (Won 2005; Naik et al. 2011; Jahangirmejad et al. 2009). Those researchers reported that CTC and CTE values are significantly affected by the aggregate type and quantity. Based on the same logic, the CTC and the CTE values of AC should also be affected by the aggregate type. Typically, CTC or CTE of asphalt binder is 1.1×10^{-4} per °C and of rock ranges 0.4×10^{-5} to 1.3×10^{-5} per °C (Hardin 1995; Timm et al. 2010, Al-Ostaz 2007).

The above discussion clarifies that the researchers were investigated the CTC and CTE values in one direction, either horizontal (perpendicular to the direction of compaction) or vertical. Xu and Solaimanian (2008) determined the CTC and the CTE values along the vertical direction; all other researchers measured along the horizontal direction. In addition, the effect of cross-anisotropy (vertical versus horizontal directions) is still an unsolved issue. In addition, the effects of AV, aggregate geology, aggregate gradation etc. are still unknown issues. The present study proposes to investigate all these issues using both field and laboratory compacted asphalt samples so that the readers can use the proposed thermal model for a wide range of conditions.

Bayat and Knight (2010) and Al-Qadi et al. (2005) measured the thermal strain in their instrumentation section. However, the researchers did not determine the field α-value. In addition, no calibration procedure of the strain gauge was described by these researchers. The nonlinear behavior of α-value with temperature can also be an issue. In addition, the aggregate type, gradation and air void may also affect the results. Hence, their findings cannot be used in this study because, α-value depends on material temperature. Therefore, it can be said that there are no field CTC and CTE values in the literature which can be used to measure thermal strain in the field at different temperature ranges. This study determines the α-value at different temperatures to use it in different phases of the study.

The α-value can be determined using the following Eq.:

$$\alpha = \frac{\Delta L / L_o}{\Delta T} \tag{7}$$

where L_o is the original length of the samples, ΔL is the change in length due to change in temperature by ΔT. It can be determined by changing the temperature of an AC sample and measuring the corresponding change in length. The change in temperature can be applied using an environmental chamber and the change in sample length can be measured by Linear Variable Displacement Transducer (LVDT).

3.5 Determining Temperature at the Bottom of Asphalt

Determination of pavement temperature is essential to determine the thermal strain as shown in Eq. 5. It is also important in analyzing and interpreting FWD test data to backcalculate layer stiffness, in estimations of frost-thaw action and frost penetration, in calculations of cooling rates for freshly compacted asphalt layers, and in the assessment of diurnal and seasonal effects in structural response in flexible pavement (Wang 2012, Yavuzturk and Ksaibati 2002).

Studying the effects of temperature in flexible pavements started more than fifty years ago (Domaschuk et al. 1964, Littlefield 1967, Jones et al. 1968). For this purpose, it is essential to predict the temperature variations inside the pavement. Numerous studies have predicted temperature profiles in flexible pavement based on statistical, numerical and probabilistic methods developed based on climate and pavement data. The data were

usually collected through the LTPP under the Strategic Highway Research Program (SHRP). However, such statistical and probabilistic methods tend to underestimate high pavement temperature or overestimate low pavement temperature.

Wang (2012) developed an algorithm using thermal properties of Hot-Mix Asphalt (HMA), pavement depth and surface temperature to predict one-dimensional (1D) temperature profiles in a multilayered pavement system. The developed algorithm can be applied in estimating temperature profiles in a multilayered pavement system. Results were validated using field data measured during 1964 to 1965 from the study of Kallas (1966). This type of old data is not valid in today's asphalt conditions as significant changes have occurred in HMA mix design and compaction methods. In addition, the fitted value was not very good at greater depths (>0.15 m).

Khadrawi et al. (2012) developed a heat transfer model to predict transient thermal behavior of AC using the thermal properties of asphalt concrete, surface and ambient temperature and solar radiation. Pavement temperature at any depth could be predicted. However, the AC layer was assumed infinite in depth and typical thermal properties of AC were assumed. The model also needed to be field validated before using in any other sites.

Yavuzturk and Ksaibati (2002) analyzed a two-dimensional (2D) finite difference model that is capable of determining temperatures on an hour-by-hour basis at any arbitrary point in an asphalt pavement. The model considers thermal ambient conditions, such as

the ambient dry bulb temperature, global solar radiation intensity, pavement geometry and orientation, ambient wind conditions and pavement thermal properties. This model is not user-friendly for practicing pavement engineers and includes a lot of variables, which are very often difficult to obtain.

Diefenderfer (2002) developed two statistical models, referred herein as Diefenderfer Statistical Model (DSM), based on the instrumentation section in Virginia named the Virginia Smart Road (VSR), to predict the maximum and the minimum temperatures at any depth of the pavement. However, these models are quite inappropriate in New Mexico (NM) pavements as the HMA mixture design and geometry of NM pavements are not similar to VSR.

Some examples of other existing models are the SHRP LTPP Models (Diefenderfer 2002). These models were evaluated for validity for the Interstate 40 (I-40) pavement in NM. The maximum temperatures for the I-40 pavement at 263 mm depth were determined using these models and the results are plotted in Fig. 7. It is observed that the DSM and LTPP model produce much greater temperature at this depth whereas the SHRP model produces much lower temperature at this depth compared to I-40 pavement. It also shows that the measured temperature at the I-40 instrumented section is consistent. The equations of these models are presented in Eqs. (8) to (10).

$$\text{SHRP Model: } T_{pav(\max)} = T_{s(\max)}(1 - 0.0063d + 0.007d^2 - 0.0004d^3) \quad (8)$$

where $T_{pav(\max)}$ is the maximum pavement temperature (°F) at depth, d (in.), $T_{s(\max)}$ is the maximum surface temperature (°F).

LTPP Model: $T_{pav(\max)} = (T_{s(\max)} + 17.8)(1 - 0.00248d + 0.000011d^2 - 0.0024d^3) - 17.8$ (9)

$T_{pav(\max)}$ is the maximum pavement temperature (°C) at depth, d (m), $T_{s(\max)}$ is the maximum surface temperature (°C).

DSM Model: $T_{pav(\max)} = 0.686x_1 + 0.000567x_2 - 27.87x + 2.7875$ (10)

$T_{pav(\max)}$ is the maximum pavement temperature (°C) at depth, x_1 is the maximum air temperature (°C), x_2 is the calculated daily solar radiation (kJ/m^{2}day), and x is the depth from the surface (m).

Formal statistical analysis is conducted to evaluate the mean (average) temperatures and the measured data of these models. One-Way Analysis of Variance (ANOVA) is performed with null hypothesis that the mean (average) values of the temperature data are equal and the alternative hypothesis is that the mean values are not equal. The test yields the *p*-value (probability of null hypothesis to be true) closer to zero (much less than 0.05). Therefore, the null hypothesis is rejected in favor of the alternative hypothesis. This concludes that the mean values are not equal at 95% Confidence Interval (CI). ANOVA test requires that the data is normally distributed. This assumption is evaluated by the

formal normality test namely Shapiro-Wilk Normality test. The null hypothesis of this test is that the data are normally distributed and the alternative hypothesis is that the data are not normally distributed. This test produces *p*-value ranges between 0.64 and 0.72 for the four set of data presented in Fig. 7. As the *p*-value is much greater than 0.05, the alternative hypothesis is rejected in favor of the null hypothesis. Therefore, the normality assumption of the data is satisfied and the result produced in the ANOVA test is valid.

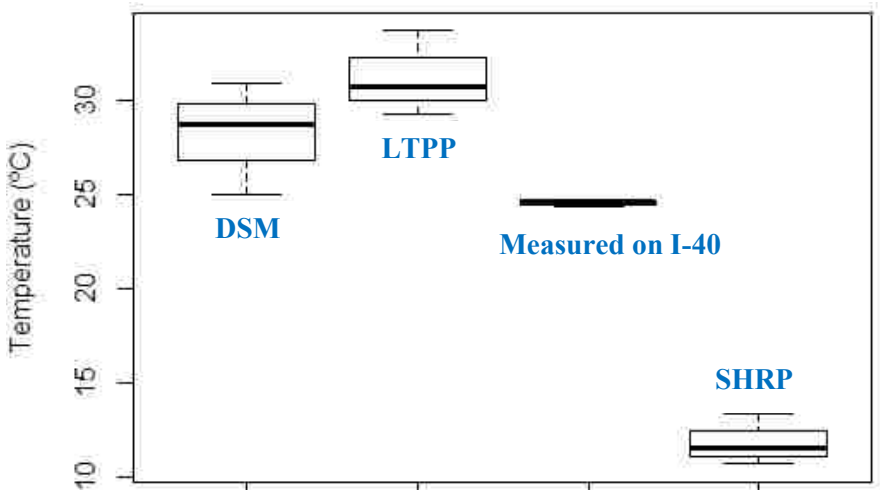

Figure 7. Comparisons of measured temperature with other studies

Pair-wise *t*-test was also conducted to evaluate which pair or pairs of means differ(s). Fisher's least Significant Difference (FSD) method yields the output listed in Table 1. The LTPP and the DSM models have *p*-value greater than 0.05 and thus, these two models produce the equal mean value at 95% CI. No other combination has the equal mean value. Therefore, no existing model perfectly represents the field condition of I-40 pavement in New Mexico. The reason is the climate conditions of New Mexico. This is a

rocky and arid area; where, typical day-night temperature fluctuation is so high, humidity and rainfall are so low.

Table 1. *p*-values of multiple comparison tests using FSD method

	DSM	LTPP	Measured
LTPP	0.097	-	-
Measured	0.0405	0.003	-
SHRP	0.000008	0.00002	0.00005

3.6 Thermal Strain

Though the AASHTOWare Pavement ME Design has not considered thermal fatigue damage yet, several researchers have reported a significant strain development and damage in pavements due to day-night temperature fluctuation. Bayat and Knight (2010) measured daily strain fluctuations as high as 650 με and yearly strain fluctuations as high as 2544 με per year at the bottom of AC in a test section in Canada. Al-Qadi et al. (2005) measured the daily thermal strain up to 350 με at the bottom of surface layer in an instrumented pavement section in Virginia. These measured strain values are quite large. Thousands of traffic repetitions occurs during one temperature cycle, it is possible that one cycle of temperature may cause significant amount of damage simply due to large amplitude of strain. Therefore, temperature-induced fatigue damage should be considered in addition to traffic-induced fatigue damage in determining the fatigue cracking in AC. In the study of Islam and Tarefder (2013b), it was found that temperature produced thermal strains are larger than traffic-induced tensile strain in a pavement section in New Mexico.

3.7 Development of Traffic-Induced Fatigue Model

Study on the development of the traffic-induced fatigue model, currently being used in the AASHTOWare Pavement ME Design Software, is essential. This is because the proposed temperature-induced fatigue model to be developed during this study may be included in the Pavement ME Design Software in future. Therefore, both models developed using similar logic and assumptions so that they are comparable. The traffic-induced fatigue model has been developed through the National Cooperative Highway Research Project (NCHRP), 1-37A (NCHRP 2004). Initially, it was named Design Guide (DG) 2002 which is now known as the AASHTOWare Pavement ME Design Guide.

3.7.1 Calibration of Regression Coefficients

Two available models were examined first: the Shell Oil model and the Asphalt Institute (AI) model (El-Basyouny and Witczak 2005a,b). By examining both the preliminary results of the Shell Oil and the Asphalt Institute models, it was clear that the Shell Oil model possessed more scatter and did not possess any definite trends to follow. The Asphalt Institute model had much less scatter and resulted in a definite trend between damage and cracking for sections greater than 4 in. to 6 in. AC layer and thin AC sections (less than 4 in.). Based on the initial study, it was concluded that the Asphalt Institute model was more acceptable model initially to use as the base model for the prediction of the fatigue damage percentage for the new model. For the AI's fatigue equation, the number of load repetitions to failure is shown in the following equation:

$$N_f = 0.00432x10^{M}\left(\frac{1}{\varepsilon_t}\right)^{3.291}\left(\frac{1}{E}\right)^{0.854} \quad (11)$$

Then a trial section has been assumed as follows:

$$N_f = 0.00432(k_1)(\beta_{f1})(10^{M})\left(\frac{1}{\varepsilon_t}\right)^{3.291\beta_{f2}}\left(\frac{1}{E}\right)^{0.854\beta_{f3}} \quad (12)$$

where N_f is the allowable number of traffic load repetition; *M is* discussed in Eq. (3); k_1, β_{f1}, β_{f2} and β_{f3} are calibration coefficients. Eighty-two LTPP sections were selected for the fatigue simulation because they contained fatigue-cracking data in the database. The 82 sections were located in 24 different states with different climatic locations. The asphalt concrete mix bottom-up, fatigue-cracking model was calibrated following the process noted here:

a) Calibration (performance) data were collected from the LTPP database for each field section.
b) Simulation (predictive) runs were performed using the DG software and a different set of calibration coefficients in the number of-load repetition model.
c) The predicted damage from each calibration coefficient combination was compared with the measured cracking observed in the field. The coefficient combination with the least scatter of the data and the correct trends was selected.
d) The predicted damage was correlated to the measured cracking in the field by minimizing the square of the errors.

The simulation runs were accomplished by running the software for a combination of values of the calibration factors β_{f2}, β_{f3}.The other constant, β_{f1} was considered unity and k_1 was assumed a function of the total asphalt concrete layer thickness. After the simulation, it was found that for β_{f1}=1, β_{f2}=1.2 and β_{f3} =1.5, the field measured cracking best correlated with the predicted cracking. Finally, k_1 was found to be:

$$k_1 = \frac{1}{0.000398 + \frac{0.003602}{1 + e^{11.02 - 3.49h}}} \tag{13}$$

where h is the total AC thickness.

3.7.2 Determining Damage Shift Factor

The next step of the calibration process was to derive an appropriate shift function relating predicted damage to the measured alligator fatigue cracking. The correlation between the alligator cracking and damage was based on two assumptions:

a) A sigmoidal function form is the best representative of the relationship between cracking and damage. This is an extremely reasonable assumption, because the relationship must be "bounded" by 0 ft^2 cracking as a minimum and 6,000 ft^2cracking as a maximum.

b) An alligator cracking value of 50% cracking of the total area of the lane (6,000 ft^2) occurs at a damage percentage of 100%.

The fatigue cracking–damage transfer function used in the calibration of the DG alligator (bottom-up) fatigue cracking was assumed to take on the form of a mathematical sigmoidal function. The model form selected was parameter was obtained from the relationship between the rate of cracking and the thickness of the AC layer. The rate of cracking was calculated from only 26 sections (of 82 sections) that developed significant cracking. This shift factor was found manually for each group to satisfy the assumption that 50% of the fatigue cracking occurs at 100% damage. The relationship between the amount of fatigue cracking and the damage factor was found to be:

$$FC(\%) = \left(\frac{6000}{1 + e^{2C_2 - C_2 \log D\%}} \right) x \left(\frac{1}{60} \right) \tag{14}$$

where C_2 can be expressed as:

$$C_2 = -2.40874 - 39.748(1 + h)^{-2.856} \tag{15}$$

In addition to the above correlation, the correlation required the damage shift factors adopted for each thickness group are shown in Table 2.

Table 2. Damage shift factor used in damage ratio

AC Thickness (in.)	Damage Shift Factor
<2	0.000398
2-4	0.002934
4<	0.004

CHAPTER THREE

DETERMINING THERMAL STRAIN

3.1 General

As a first step of developing the model, it was needed to determine the thermal strain developed at the bottom of AC due to day-night temperature fluctuations. This chapter discusses the procedure to determine the probable thermal strain in asphalt.

3.2 Determining α-Value

3.2.1 Background

LVDT is made up of steel and membrane which also expand and contact with temperature change. Therefore, LVDT needs to be calibrated first before using it to measure change in sample length. The calibration of LVDT is described in the following section.

3.2.2 Calibration of Linear Variable Displacement Transducer

Temperature affects the response of deformation measuring device, LVDTs due to the expansion and contraction of steel used in the sensor. When temperature increases, both the AC material and the sensor's components expand and vice-versa. The effects of thermal expansion and contraction of steel must be considered to determine the accurate thermal strain, more specifically, to determine the exact CTC and CTE values of the AC.

The LVDTs were also calibrated using a zerodur (whose CTC and CTE values are almost zero) in the laboratory as shown in Fig. 8. The LVDTs were glued to the zerodur and the

whole system was kept inside an environmental chamber. Temperature increase from -20 ˚C to 50 ˚C and decrease from 55 ˚C to -20 ˚C were made at a rate of 0.5 ˚C/min and the corresponding deformation (strain) variations in the LVDTs were recorded using a data acquisition system. The chamber temperature and the inside sample temperature were monitored continuously. The test was continued until both the chamber temperature and the inside sample temperature coincided each other. The total process of the temperature increase and decrease took about 12 hours. The test was repeated in another day to cross check the reliability of the data.

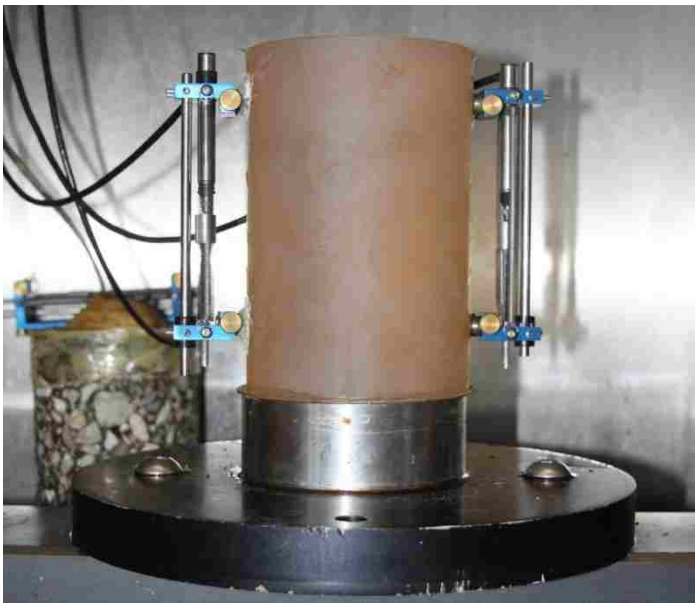

Figure 8. Calibration of the LVDTs

It was observed that the LVDTs showed negative (contraction) results upon increase in temperature. This can be explained using Fig. 9, where the mechanism of contraction has been explained. The zerodur does not expand due to increase in temperature, whereas, the LVDT steel rods used in the LVDT expand. As the ends of the LVDT are glued to the

zerodur, the sensor spring must contract to accommodate the expansion of steel rods. Therefore, upon increase in temperature, LVDT shows contraction output if the material (here, zerodur) does not expand. In Fig. 9, the gauge length is L, which does not change as the zerodur does not expand nor contract. Upon increase in temperature, the length of two steel components, L_1 and L_2 become $L_1+\Delta L_1$ and $L_2+\Delta L_2$ respectively. Consequently, the spring length is reduced by $\Delta L_1+\Delta L_2$, which results the contraction strain of $(\Delta L_1+\Delta L_2)/L$ due to an increase of temperature by ΔT.

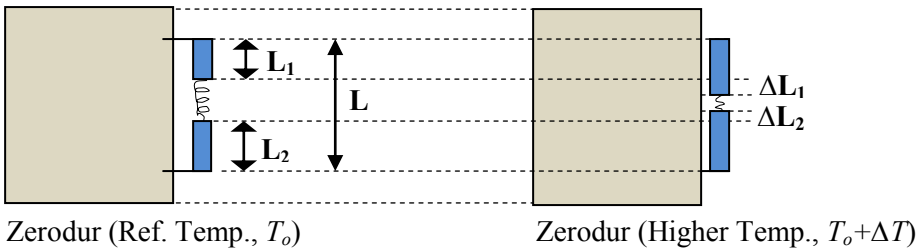

Figure 9. Contraction mechanism of LVDT due to increase in temperature

Fig. 10 plots the strains due to the increase and the decrease in temperatures between the range of -20 ˚C and 50 ˚C. It shows that the resulting strains follow almost straight lines with temperature. The contraction strain due to unit increase in temperature is termed as the CTE of LVDT and the expansion strain due to unit decrease in temperature is termed as the CTC of LVDT. From the best fit straight curve, it is found that the CTC and CTE values of LVDT are 2.56×10^{-5} per ˚C and 2.13×10^{-5} per ˚C respectively. The second test at another day yields the similar results. These values should be adjusted with the values obtained from the actual AC sample testing.

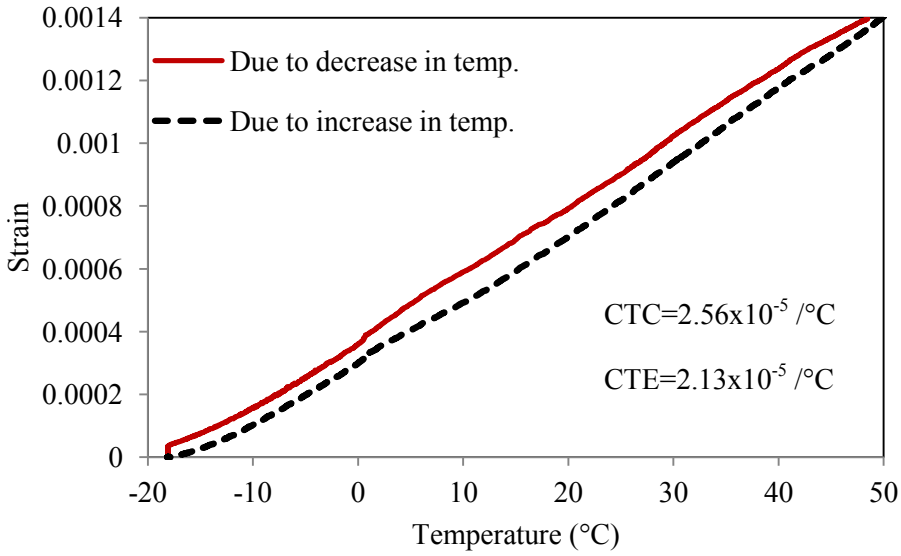

Figure 10. CTC and CTE of LVDTs

3.2.3 Sample Collection and Preparation

Field collected cylindrical core sample of 100 mm diameter and 50 mm height were used to investigate the effect of temperature on CTC and CTE values of AC. The field cores were collected in collaboration with the New Mexico Department of Transportation (NMDOT) from the I-40 section in New Mexico. The sample was collected from the pavement section before the highway was open for traffic. The coring of a sample from the section is shown in Fig. 11(a). The cores were cut into 100 mm diameter and 50 mm height samples as shown in Fig. 11(b) using the laboratory saw in the laboratory.

a) Collecting the field core

b) Sample cutting in the laboratory

Figure 11. Sample collection and preparation

The bulk and the theoretical maximum densities were determined following the AASHTO T 166-07 (2007) and the AASHTO T 209-05 (2007) tests protocols respectively. The AVs of the samples were measured between 5.1 to 5.4% with an average value of 5.2%. The mixture used in the pavement is a widely used dense graded Superpave (SP) mix, type SP-III with the maximum aggregate size of 25 mm. The mixture contained 35% Reclaimed Asphalt Pavement (RAP) materials. Performance Grade (PG) binder, PG 76-22 was used an amount of 4.4% by the weight of the mixture. About 5% of materials passed through the No. 200 sieve size (0.075 mm).

3.2.4 Testing

A total of three samples were tested in the temperature range of -20 ˚C to 55 ˚C. Two LVDTs were glued at the surfaces of the cylindrical thin samples as shown in Fig. 12. The LVDTs measured the change in diameter of the sample upon change in temperature. One cooling cycle and one heating cycle were used with five increments (change of 15 ˚C) of each. After each temperature change, there was about four hours of waiting period

to ensure temperature equilibrium inside the specimens. The cooling or heating rate used was at a rate of 0.5 °C per min. Continuous record of temperatures and deformations throughout the test were made using the LVDTs and temperature probes. Each cooling or heating cycle took about 30 hours to complete.

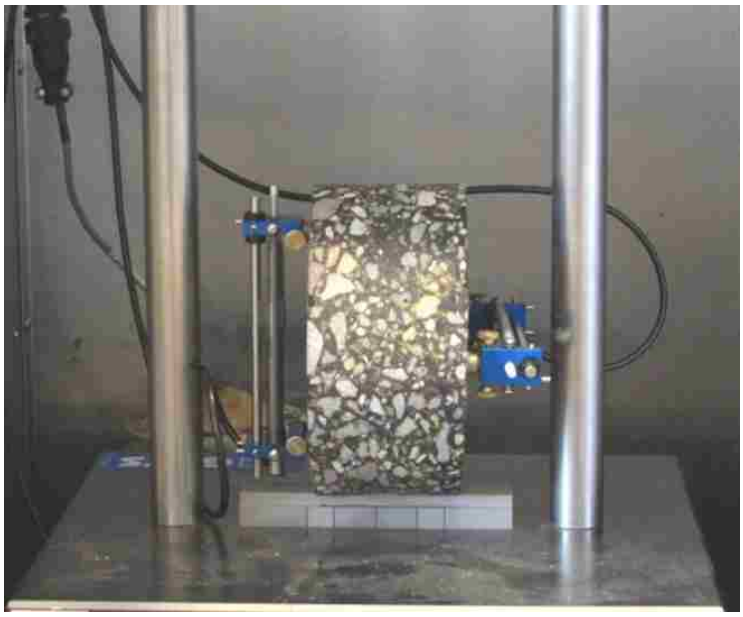

Figure 12. Measuring the expansion-contraction due to temperature change

3.2.5 Results and Discussion

The decrease in thermal strain with respect to the decrease in temperature was considered the CTC and the increase in thermal strain with respect to the increase in temperature was considered the CTE. The laboratory CTC and CTE values (averages of the three samples) are listed in Table 3. It can be seen that the CTC and CTE values are not constant at different temperature. For instance, the CTC value varies from 0.33×10^{-5} to 3.11×10^{-5} per °C at different temperature. The CTE value ranges 2.38×10^{-5} per °C to 3.12×10^{-5} per °C. Similar observation was also made in the study of Islam and Tarefder (2014b). In that

study, field CTC/CTE values were determined using field strain sensors. The Standard Deviations (SDs) of the values range 6 to 11%. The average of the CTC and the CTE values is considered the α-value and plotted in Fig. 13. It shows that the α-value is also non-linear with temperature. The α-value increases with temperature; reaches to a peak and then decreases with the increase in temperature. The α-value at any temperature can be determined using the developed by best fit curve of the data presented in Fig. 13.

Table 3. Measured CTC and CTE values at different temperature ranges

Temperature Range (°C)	CTC and CTE (10^{-5} per °C)		
	CTC	CTE	Avg. of CTC and CTE (α-value)
-20 to -5	0.33	3.12	1.73
-5 to 10	1.92	2.81	2.37
10 to 25	2.94	2.38	2.66
25 to 40	3.11	2.56	2.84
40 to 55	2.57	2.63	2.60

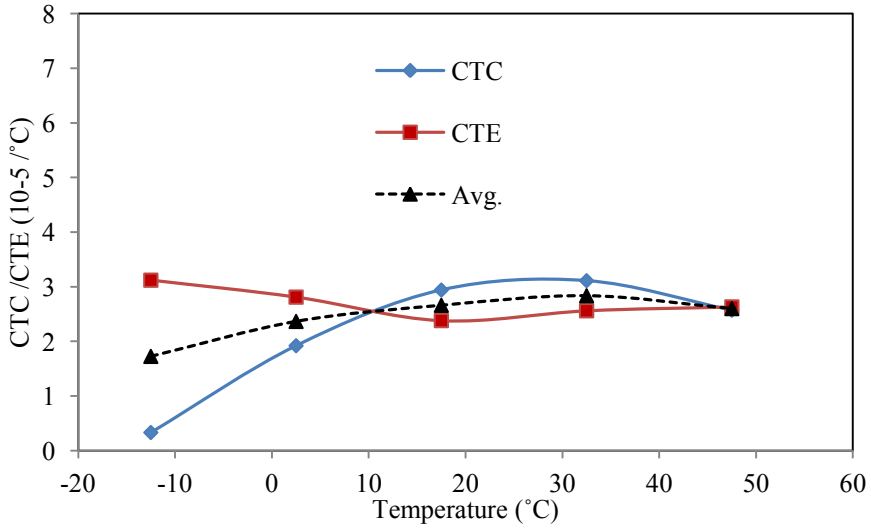

Figure 13. Temperature-dependent α-value

The α-values (με/°C) at the different temperatures (°C) can be determined using the following Eq. which was developed using the best fit curve of the measured data:

$$\alpha = -0.006T^2 + 0.356T + 22.633 \quad (16)$$

This model was used to determine the thermal strain at the bottom of AC which is discussed later.

3.3 Further Study on α-value

3.3.1 Investigating the Effect of Cross-Anisotropy

AC is not isotropic material. The recent studies by the author and his group prove that AC material is at least cross-anisotropic (Islam et al. 2014b, Ahmed et al. 2013, Ahmed et al. 2014, Tarefder et al. 2013, Tarefder et al. 2014). However, the difference of CTC and CTE values in the vertical and the horizontal directions is not mentioned in the literature. This study hypothesizes that the CTC and the CTE values of AC in vertical and horizontal directions are not equal considering the compaction force and particle arrangement. The CTC and the CTE values in the vertical direction were measured using cylindrical samples of 100 mm and 150 mm high. Cylindrical samples of 100 mm diameter and 50 mm thickness were used to measure these values along the horizontal direction as discussed in the previous section.

3.3.1.1 Sample Collection and Preparation

The samples were collected from the I-40 instrumented section as described earlier. The samples were then cut into 100 mm diameter and 150 mm height. The AVs of the samples were measured between 4.9 and 5.5% with an average value of 5.3%.

3.3.1.2 Testing

Three replicates samples were tested in the temperature range of -20 °C to 55 °C. Two LVDTs were glued at the curved surface of the cylindrical samples. While testing, the sample was laid down to avoid the gravity action as shown in Fig. 14. The LVDTs measured the change in the length of the sample upon change in temperature. The heating or the cooling schemes were the same as the horizontal samples as discussed earlier.

Figure 14. Measuring the thermal expansion-contraction (Vertical Direction)

3.3.1.3 Results and Discussion

The CTC and CTE values in both the vertical and the horizontal directions at different temperature are presented in Fig. 15. It can be observed from Fig. 15(a) that the horizontal CTC value is smaller than the vertical one except at one point. However, the horizontal CTE value is smaller than the vertical one between the temperature of -20 °C and 55 °C and follows parallel. Both the CTC and CTE values along horizontal direction are measured to be 4.7% smaller than the vertical values.

The reason for the horizontal CTC and CTE values being smaller than vertical values may be the particle arrangement. The flat and elongated particles lie horizontally upon applying compaction pressure. Referring the surface area point of view, the binder content of a single aggregate on a horizontal direction (i.e. flat and elongated face) is greater than that of vertical direction (i.e. short face). Then, if one imaginary line is assumed in vertical direction and one in horizontal direction, it can be observed that the binder amount along the vertical line is greater than that of the horizontal line. This explanation applies to both coarse and fine aggregates. However, the authors did not conduct any microscopic study. By visual inspection, it was observed that number of aggregates showing the long and elongated face on the surface of AC sample is actually greater compared to showing the short face of aggregate. The CTC and CTE values of binder are roughly 10 to 30 times greater than the aggregate (Hardin 1995, Timm et al. 2010, Al-Ostaz 2007). Therefore, a very small decrease in binder content might cause the decrease in the CTC and the CTE values. A statistical test is required to evaluate the results whether the change in the CTC and CTE values are significant or not.

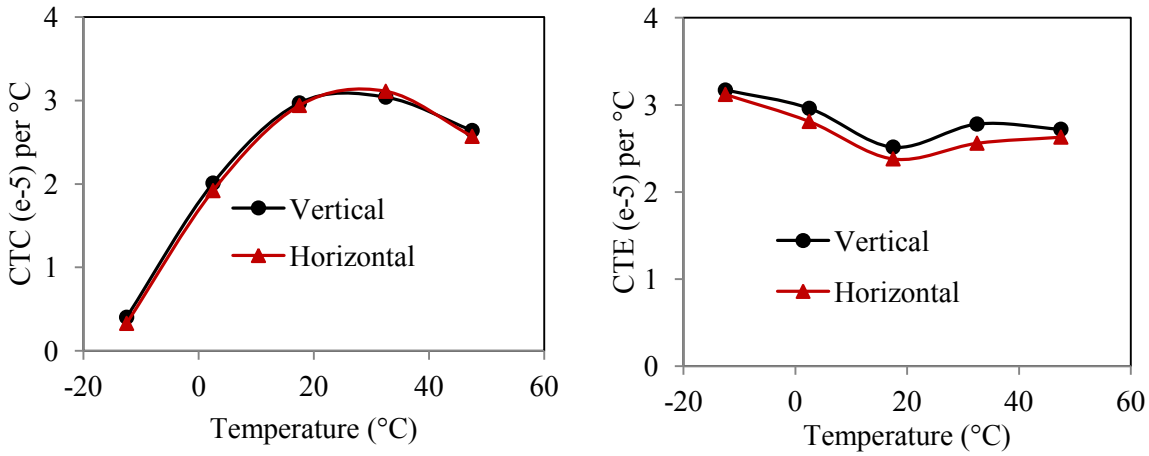

a) CTC with temperature b) CTE with temperature

Figure 15. Cross-anisotropic CTC and CTE values with temperature

ANOVA test was conducted to evaluate the decrease in the CTC and CTE values along horizontal direction using the test data between 25 °C and 40 °C. The null hypothesis was that the average values were equal and the alternative hypothesis was that the average values were not equal. The *p*-values (probability of null hypothesis to be true) of the tests of CTC and CTE values were found to be 0.13 and 0.365 respectively. As both of these values are greater than 0.05 (5%), the null hypothesis is true. Therefore, the values are statistically equal at 95% CI. Conclusions can be made that the CTC and the CTE values are equal both in the horizontal and vertical directions.

3.3.2 Investigating the Effect of Air Void

3.3.2.1 Sample Collection and Preparation

Laboratory compacted cylindrical thin samples of 150 mm diameter and 50 mm thick were used to investigate the effect of Air Void (AV). Cylindrical samples of 150 mm diameter and 170 mm height were prepared following AASHTO T 312-07 (2007) test

protocol and then, cut into the desired size using a laboratory saw. The loose mixture was collected from the I-40 instrumented section at the time of construction. It is a SP-III mixture with 35% RAP and PG 76-22 binder was used by 4.4% of the weight of the mix. Three sets (three samples of each) of samples were prepared; the average AVs are 1.4%, 5.5% and 9.7% with SDs of 0.3%, 0.4% and 0.4% respectively.

3.3.2.2 Testing

The samples were tested in the temperature range between 20 °C and 40 °C. The CTC and the CTE values were measured along the horizontal direction of the samples. The variations of thermal expansion and contraction at this temperature range were considered linear. At the two extreme temperature points, there were about four hours of waiting period to ensure temperature equilibrium inside the specimens. The cooling or heating was conducted at a rate of 0.5 °C per min, which was the same in the whole study. Continuous record of temperatures and deformations throughout the test were made using the LVDTs and temperature probes.

3.3.2.3 Results and Discussion

The measured CTC and CTE values (average) for all the three different types of samples are plotted in Fig. 16. The average CTC values are $3.35x10^{-5}$, $3.19x10^{-5}$ and $2.84x10^{-5}$ per °C of the air void of 1.4%, 5.5% and 9.7%, respectively, with the SDs of 0.30 $x10^{-5}$, 0.14 $x10^{-5}$ and 0.17 $x10^{-5}$ per °C. That means the CTC value decrease with increase in AV. Similar observation has been made on the CTE values. There is greater void space inside the material of the higher AV. As the individual particle elongates, it occupies the void

space at least a little bit without affecting the dimensions of the whole sample. This may be the reason for the lower values of the CTC and the CTE. However, statistical tests are needed to evaluate this decreasing behavior.

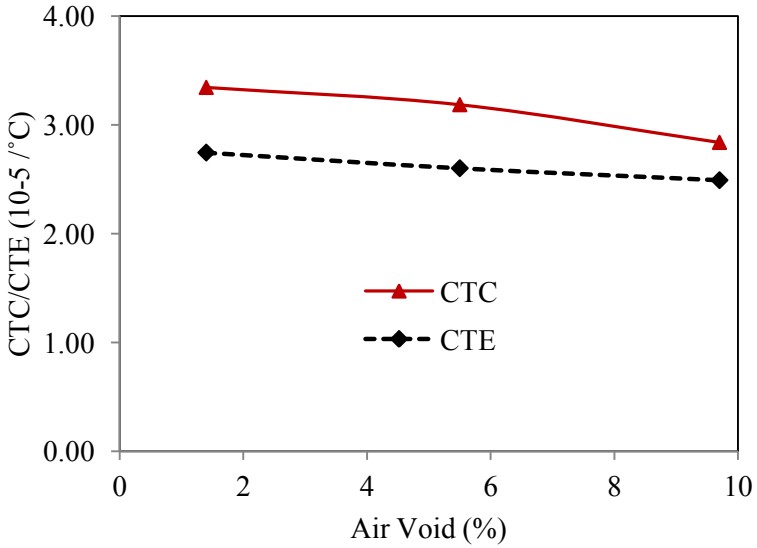

Figure 16.Variations of the CTC and the CTE values with AV

Pairwise *t*-tests were conducted to evaluate the decrease in the CTC and CTE values with AV. The null hypothesis was that the average values of the CTC and the CTE of any pair were equal and the alternative hypothesis was that the average values were not equal. The *p*-values of the test results are listed in Table 4. It shows that all the *p*-values are greater than 0.05 for all pairs. Therefore, the null hypothesis is true and all the CTC and CTE values are equal (regardless of the air voids of the samples) at 95% CI. Finally, it can be concluded that the CTC and CTE values are not affected significantly by the AV of the sample, although Fig. 16 shows the decreasing behavior.

Table 4. *p*-values of the CTC/CTE of AC with different AVs

		AV-1.4%	AV-5.5%
CTC	AV-5.5%	0.294	-
	AV-9.7%	0.279	0.622
CTE	AV-5.5%	0.276	-
	AV-9.7%	0.413	0.310

3.3.3 Investigating the Effect of Aggregate Type

3.3.3.1 Sample Collection and Preparation

AC is composed of asphalt both binder and aggregate. Therefore, the CTC and CTE values of AC should be affected if the aggregate type (expansion and contraction behavior) changes (Won 2005; Naik et al. 2011; Jahangirmejad et al. 2009). Three types of aggregates were used in this study to evaluate the aggregate effect. These are basalt, river deposits and gravel-sand which are very widely used in the construction of highways in the state of New Mexico, USA. The average bulk specific gravities were measured to be 2.75, 2.67 and 2.63 and water absorptions capacities are 1.5%, 0.5% and 0.9% of the basalt, river deposits and gravel-sand respectively (AASHTO T 84-00 (2007), AASHTO T 85-91 (2007). The physical properties of the three aggregates such as, flat and elongated pieces of aggregates, fine aggregate angularity, combined sand equivalent etc. were maintained the same for all the mixtures. The raw materials were collected from the NMDOT and all the quality insurance was made in the laboratory.

Cylindrical samples of 150 mm diameter and 170 mm height were prepared following AASHTO T 312-07 (2007) test protocol in the laboratory. The samples were then cut into cylindrical thin samples of 150 mm diameter and 50 mm height using a laboratory saw. The mixture was a SP-III mixture and PG 70-22 binder was used by 4.5% of the weight of the mixture. The average AV of the samples was 5.1% (with SD of 0.3%). The gradation of the aggregate is presented in Fig. 17. All the three types of mixtures were prepared following this gradation chart.

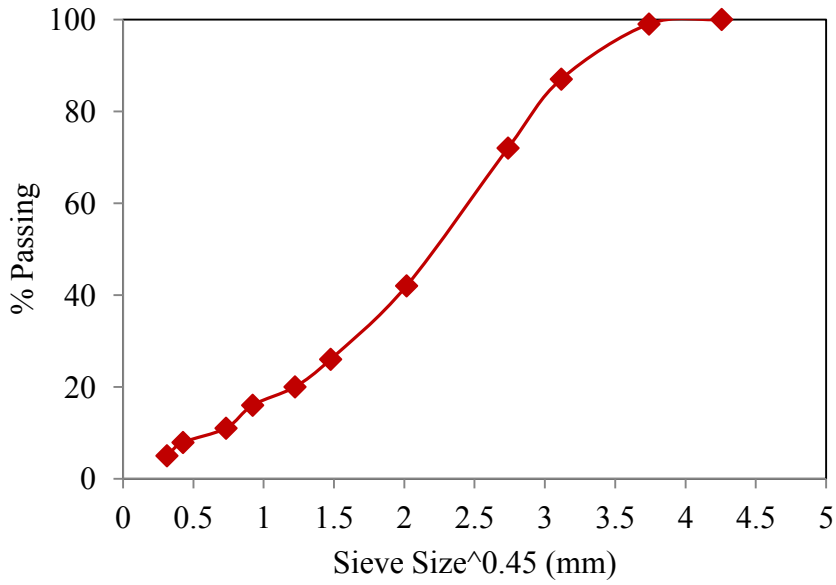

Figure 17. Gradation of AC containing different aggregate types

3.3.3.2 Testing

A total of nine samples (3 types, 3 replicates of each) were tested to determine the CTC and CTE values between the temperature range of 20 °C and 40 °C in the horizontal direction. At the two extreme temperature points, there were about four hours of waiting

period to ensure equilibrium temperature all over the specimens. The cooling or heating was conducted at a rate of 0.5 ˚C per min.

3.3.3.3 Results and Discussion

The CTC values are presented in Fig. 18. The average CTC values are $3.28x10^{-5}$, $3.06x10^{-5}$ and $2.88x10^{-5}$ per °C with SDs of $0.06x10^{-5}$, $0.04x10^{-5}$ and $0.08x10^{-5}$ per °C of the mixtures with river deposits, basalt and gravel-sand respectively. That means that the mixture with river deposits has the highest value of CTC and the mixture with gravel-sand has the lowest. All of these mixtures have same conditions except the aggregate types. Therefore, the aggregate type plays this role to cause a change in the CTC value.

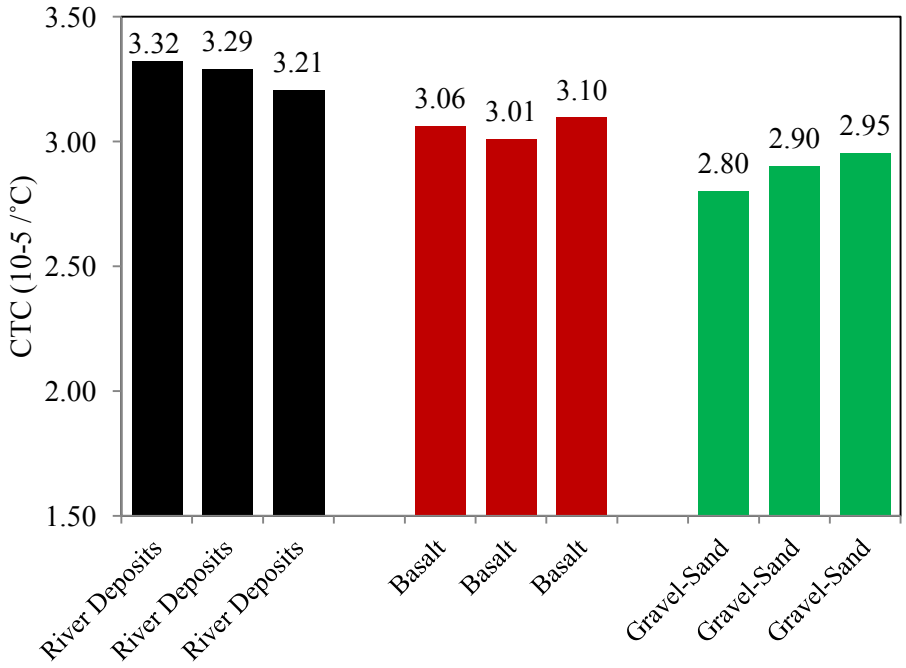

Figure 18.CTC values with aggregate type

Pair wise *t*-tests were conducted to evaluate the change of the CTC value with the aggregate type. The null hypothesis was that the average values of CTC of any pair of mixtures were equal and the alternative hypothesis was that the average values were not equal. The *p*-values of the test results are listed in Table 5. It shows that all the *p*-values are smaller than 0.05 (5%). Therefore, the null hypothesis is rejected and all the CTC values are not equal at 95% CI. Finally, it can be concluded that the CTC values are affected significantly by the aggregate type of the sample as shown in Fig. 18.

Table 5. *p*-values of the CTC/CTE of SP-III AC with different aggregates

		Basalt	River Deposits
CTC	River Deposits	0.008	-
	Gravel and Sand	0.038	0.003
CTE	River Deposits	0.0003	-
	Gravel and Sand	0.041	0.002

The CTE values are presented in Fig. 19. The average CTE values are 3.73×10^{-5}, 2.39×10^{-5} and 2.23×10^{-5} per °C with SDs of 0.04×10^{-5}, 0.03×10^{-5} and 0.001×10^{-5} per °C of the mixtures with river deposits, basalt and gravel-sand respectively. That means that the mixture with river deposits has the highest value of CTE and the mixture with gravel-sand has the lowest. The similar behavior was observed for the CTC values.

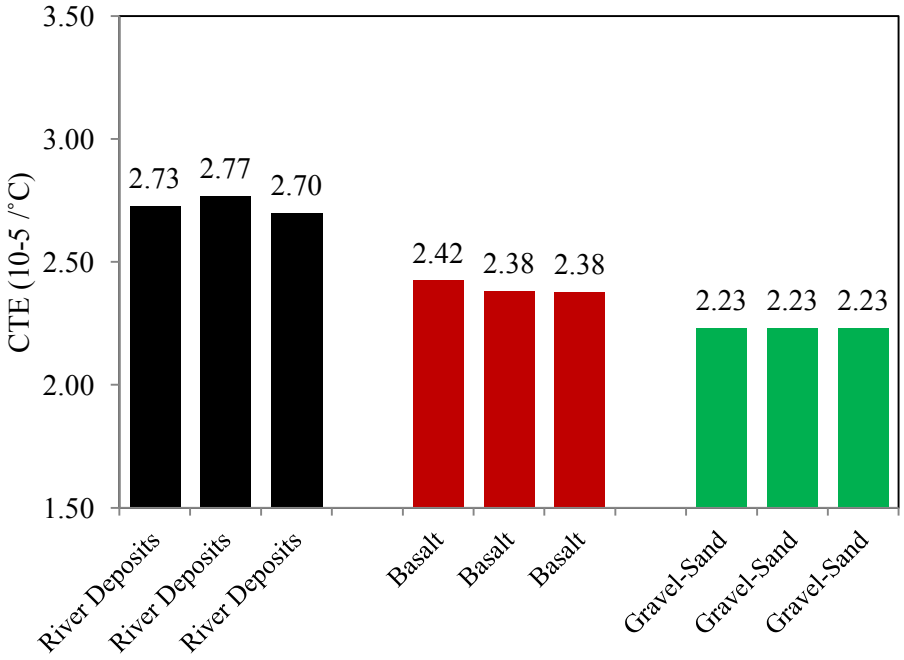

Figure 19.CTE values with aggregate type

The *p*-values of the pair wise t-test results are also listed in Table 5. It shows that all the *p*-values are smaller than 0.05 (5%). Therefore, the null hypothesis is rejected and all the average CTE values are not equal at 95% CI. Finally, it can be concluded that both the CTC and the CTE values are affected significantly by the aggregate type of the sample.

3.3.4 Investigating the Effect of Aggregate Gradation

3.3.4.1 Sample Collection and Preparation

Three types of gradations (SP-II, SP-III and SP-IV) were used to evaluate the effect of aggregate gradation on the CTC and CTE of asphalt concrete. The mixtures contain PG 70-22 binder of 4.7% of the weight of the mixture. The gradations of the mixtures are presented in Fig. 20. Plant produced loose mixtures (SP-II, SP-III and SP-IV) were collected from ongoing construction site in collaboration with NMDOT. It was ensured

that all the three mixture had the same physical properties except the aggregate gradation. The average AV of the samples is 4.9% (with SD of 0.4%). Cylindrical samples of 150 mm diameter and 170 mm height were prepared following AASHTO T 312-07 (2007) test protocol. The samples were then cut into cylindrical thin samples of 150 mm diameter and 50 mm height.

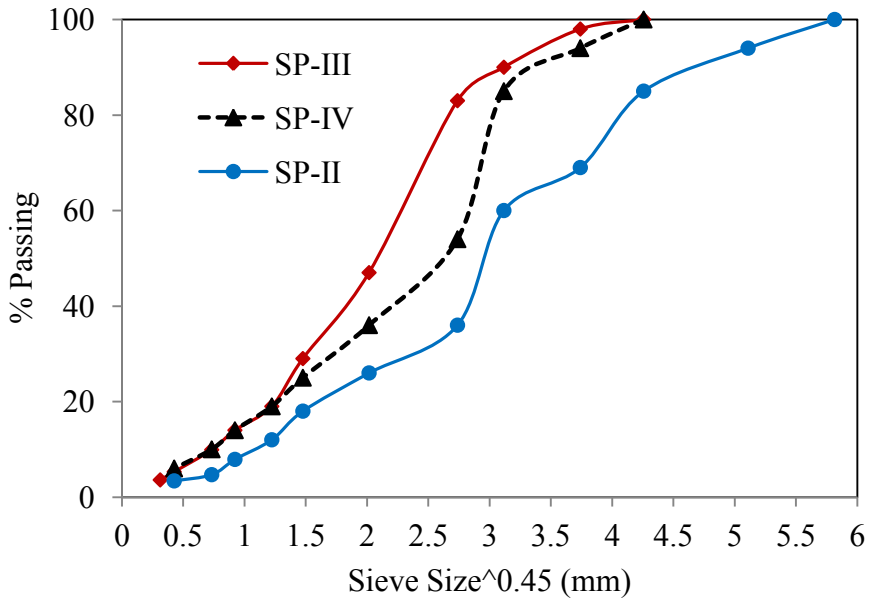

Figure 20. 0.45 power charts of the three mixtures

3.3.4.2 Testing

A total of nine samples (3 types, 3 replicates of each) were tested between the temperature range of 20 ˚C and 40 ˚C in the horizontal direction. The test parameters were similar with the other test programs described earlier.

3.3.4.3 Results and Discussion

The CTC and the CTE values are plotted in Figs. 21 and 22 respectively. The average CTC values are $3.2x10^{-5}$, $3.28x10^{-5}$ and $3.38x10^{-5}$ per °C with SD of $0.14x10^{-5}$, $0.19x10^{-5}$ and $0.15x10^{-5}$ per °C for the SP-II, SP-III and SP-IV mixture respectively. The average CTE values are $2.45x10^{-5}$, $2.8x10^{-5}$ and $2.36x10^{-5}$ per °C with SD of $0.25x10^{-5}$, $0.02x10^{-5}$ and $0.18x10^{-5}$ per °C for the SP-II, SP-III and SP-IV mixture respectively. It can be seen that there is no regular pattern between the CTC and the CTE values.

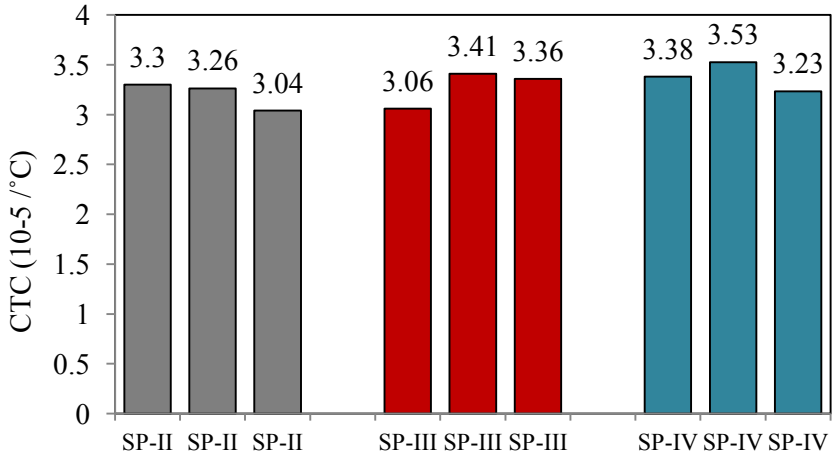

Figure 21.CTC values with aggregate gradation

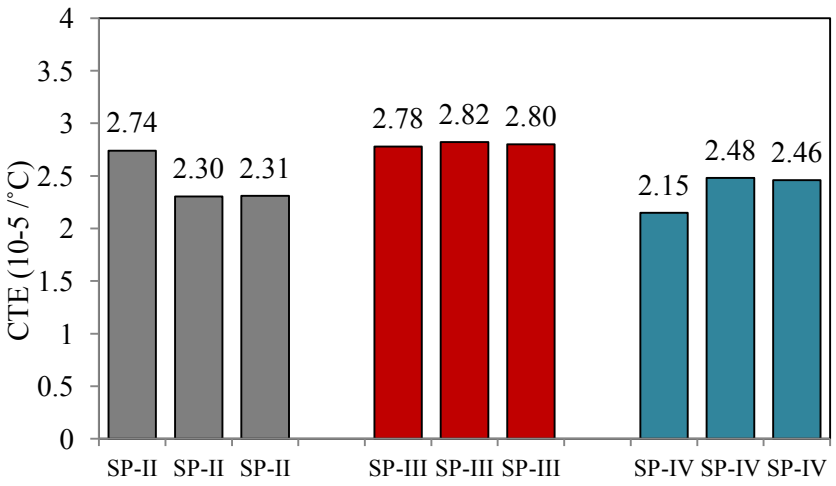

Figure 22.CTE values with aggregate gradation

Statistical pair wise *t*-tests were conducted to evaluate the change of the CTC and CTE values with aggregate gradation. The *p*-values of the test results are listed in Table 6. It shows that all the *p*-values are greater than 0.05 (5%). Therefore, the null hypothesis is true and all the CTC and the CTE values are equal at 95% CI. Finally, conclusion can be made that aggregate gradation has no effect on the CTC and the CTE values of AC as long as the volumetric contents of the aggregate and the binder remain the same.

Table 6. *p*-values of the CTC/CTE of a basalt mixture with different gradations

		SP-III	SP-II
CTC	SP-II	0.605	-
	SP-IV	0.502	0.204
CTE	SP-II	0.138	-
	SP-IV	0.054	0.657

3.4 Discussion on α-value

The CTC and CTE values, which are needed to determine the thermal strain, have been determined using laboratory testing for a wide range of temperatures. These results are also available in the study of Islam and Tarefder (2015b). Based on the findings of the study the following conclusions can be made:

- CTC and CTE values of asphalt mixture are non-linear with temperature. CTC value is concave downward and CTE value is concave upward between the temperature range of -20 °C and 55 °C. The temperature-dependent α-value (με/°C) can be presented by the following equation:

$$\alpha = -0.006T^2 + 0.356T + 22.633$$

- CTC and CTE values of asphalt mixture along the horizontal and vertical directions of compaction are statistically equal.
- The air void and aggregate gradation have no effect on CTC and CTE values of AC; however, aggregate type has a significant effect on these values.

Unless the details of the mixtures are available, the above mentioned model was used to determine the α-value (με/°C) for any mixture. Typically, α-value of AC mixture is not available in the LTPP database for lack of test evidence.

3.5 Determining Temperature Fluctuation

Temperature variation (ΔT) at the bottom of AC is required to measure the thermal strain caused by temperature fluctuation as shown in Eq. 5. Two types of models to determine the temperature at the bottom of AC were developed. The statistical model was developed based on regression analysis of a full year data from the I-40 instrumentation section. The second model, Finite Element Model (FEM), was developed but not used in any of the analyses in the study. It utilizes the thermal properties of AC material such as thermal conductivity (k), specific heat capacity (C) and the coefficient of heat convection. The FEM method is described in Appendix D.

3.5.1 Developing Regression Models

Regression models were developed to predict temperature at any depth of AC using the collected data from the I-40 pavement. The maximum, minimum and average AC temperature at any depth can be determined using the developed models. This study also verifies the developed models with further field data and statistical analysis.

3.5.1.1 Sensors Installation

Two types of sensors were installed to measure temperature related parameters such as solar radiation, air temperature and pavement temperature. The weather station measures air temperature, solar radiation, wind speed, humidity, etc. Fig. 23 shows the installed weather station. It also shows the installed cabinet box for the data acquisition system and data gathering computer. The system is powered by solar system.

Figure 23. Installed weather station

Figure 24. Installation of temperature probes

Six temperature probes were installed at different depths in the pavement. The probes were bundled together such that after installation these remained at the surface, at 50, 100, 263, 340 and 490 mm depth. The bundled probes are shown in Fig. 24. A 25 mm diameter hole was drilled with electric drill machine. Then, the hole was cleaned with a vacuum cleaner. The probes were then inserted into the hole as straight as possible keeping the top one at the same level to the surface. The temperature probes were installed around 300 mm outside the shoulder. The installed temperature probes' functionality was checked by connecting the probes to the data acquisition system.

3.5.1.2 Data Collection

The temperature and the solar radiation data were collected for one year, from October 15, 2012 to October 14, 2013. Based on the data, regression analysis was conducted to develop temperature prediction models to determine the maximum, the minimum and the average temperature at any depth of AC. The models were then validated using further data collected from October 15, 2013 to January 21, 2014.

3.5.1.3 Analysis

3.5.1.3.1 Temperature Variations

The pavement surface heats up during the day and cools down at night. Therefore, temperatures of the pavement materials vary at all times. The air and the pavement temperatures at various depths are shown in Fig. 25. The air temperature is the minimum around 8:00 am and the maximum around 15:00 pm. However, the minimum and the maximum temperatures at the bottom of the asphalt concrete are observed around 11:00 am and 21:00 pm respectively. These values are measured at 8:30 am and 16:30 pm, respectively, at 90 mm depth. Fig. 25 also shows that the average temperature may occur in pavement either about 12:00 am or 12:00 pm. The maximum and the minimum temperatures with depth of AC can be used to determine the asphalt grade needed with depth of AC. These can also be used to correlate pavement temperature with structural responses such as stress-strain due to wheel load and material properties such as stiffness of AC. In addition, determination of the maximum, the minimum and the average temperatures of a pavement may offer a close understanding of the continuous temperature variation of the pavement.

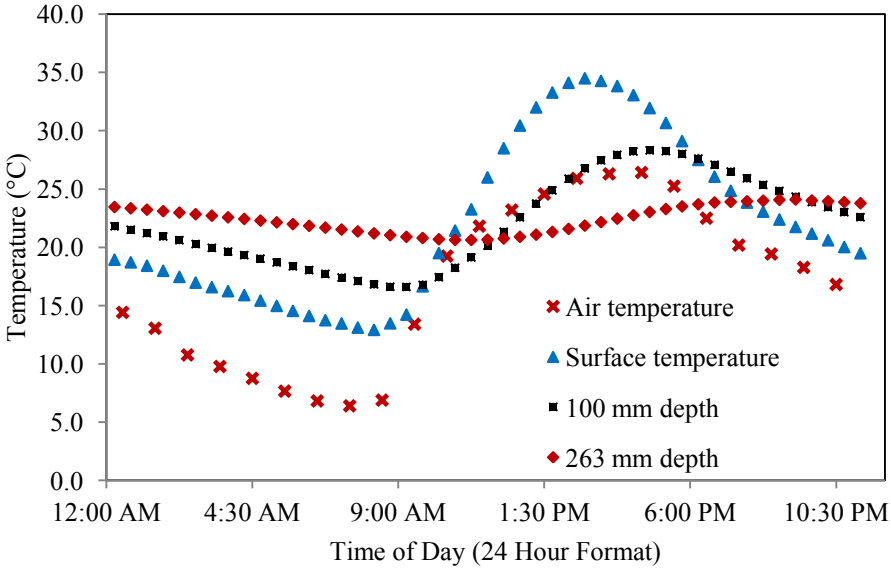

Figure 25. Temperature variations over the day on October 24, 2012

The temperature at any depth of the pavement is largely dependent on the surface temperature, solar radiation and the depth of the pavement. Linear regression analysis was conducted to determine the best-fit regression model to predict the temperature at any depth. The independent variables are solar radiation, pavement surface temperature and pavement depth. The dependent variable is pavement temperature at a particular depth.

3.5.1.3.2 Predicting the Maximum Temperature

The maximum temperature at any depth of the pavement depends on the maximum surface temperature and the concerned depth of the pavement. Solar radiation may affect the maximum temperature. This is why, it is also considered as an independent variable.

Based on regression analysis, the following two models, Eqs. (17) and (18) were developed.

$$y_{max} = 2.5 + 0.91x_{max} - 25.6x - 0.004S_{max} \quad (17)$$

$$y_{max} = 0.8 + 0.87x_{max} - 25.6x \quad (18)$$

where y_{max} = predicted daily maximum pavement temperature (°C) at any depth of AC

x_{max} = daily maximum surface temperature (°C)

x = concerned depth from surface (m)

S_{max} = daily maximum solar radiation (W/m^2)

The maximum surface temperature can be determined from the maximum air temperature using the following relationship:

$$x_{max} = 1.33a_{max} + 3.21 \quad (19)$$

where a_{max} = daily maximum air temperature (°C).

The coefficients of determination (R^2) of all equations (Eqs. (17) to (19)) were between 0.96 and 0.98, which are very close to unity. The R^2 value shows sufficient evidence for the correlation is strong. Eq. (17) predicts the maximum temperature at any depth of the

pavement using the maximum surface temperature, the maximum solar radiation and the concerned depth. However, solar radiation may not be at maximum at the time of the maximum surface temperature. Thus, the effect of solar radiation may not contribute significantly. Therefore, another regression model (Eq. (18)) is developed excluding solar radiation. This model produces a similar output to the previous model (Eq. (17)) and the weightage of solar radiation is very small. The models also show that the maximum temperature at any depth of AC is always smaller than the maximum surface temperature.

3.5.1.3.3 Predicting the Minimum Temperature

The minimum temperature of the pavement at any depth depends on the minimum surface temperature and the concerned depth. The minimum temperature usually occurs late at night or in the morning when solar radiation is insignificant. This is why solar radiation was excluded to develop the model to determine the minimum temperature at any depth of the AC. The regression model for predicting the minimum temperature (y_{min} in °C*)* is shown in Eq. (20). The model was strongly correlated as depicted by the R^2 value of 0.99.

$$y_{min} = 1.84 + x_{min} + 20x \tag{20}$$

where x_{min} = daily minimum surface temperature (°C) and can be found from:

$$x_{min} = 0.925a_{min} + 6.76 \tag{21}$$

x = concerned pavement depth (m) and a_{min} is the minimum air temperature.

This model indicates that it can never be colder inside the pavement than the minimum surface temperature and that the minimum temperature is always greater further down in the pavement.

3.5.1.3.4 Predicting the Average Temperature

The regression model to determine the daily average temperature (y_{avg}) at any depth of the AC (°C) was developed using the average surface temperature, the average solar radiation and the depth. The average surface temperature can also be related with the average air temperature. Another issue is that average temperature may occur in daytime or nighttime. The regression models are shown in Eqs. (22) and (23).

$$y_{avg} = 1.1 + 0.93x_{avg} + 3.65x + 0.0002S_{avg} \quad (22)$$

$$y_{avg} = 1.1 + 0.94x_{avg} + 3.65x \quad (23)$$

where x_{avg} is the daily average surface temperature (°C), S_{avg} is the average solar radiation (W/m^2). Both of the equations have the R^2 value of 0.69. Both these equations can be used to predict the average temperature. Eq. (23) excludes solar radiation; however, it is observed that both of these equations produce the similar outputs as the weightage of solar radiation is very low. Therefore, it is better to use the shorter model, Eq. (23). Eq. (22) can only be used if the x_{avg} occurs in daytime because S_{avg} is only available in daytime. The average surface temperature (°C) can be correlated with the average air temperature (°C) (with the R^2 value of 0.92) by Eq. (24).

$$x_{avg} = 1.136 a_{avg} + 4.956 \quad (24)$$

3.5.1.3.5 Model Validation

The predicted models were compared with the measured data. Figs. 26 and 27 plot the predicted, the minimum, and the maximum values with the measured ones at two different depths, 50 mm and 100 mm. It was observed that for both of these depths, the models predict temperature values very close to the measured data. The predicted models, for some cases, produce lower temperature than the measured minimum, and greater temperature than the measured maximum. Formal statistical tests were conducted to evaluate these differences.

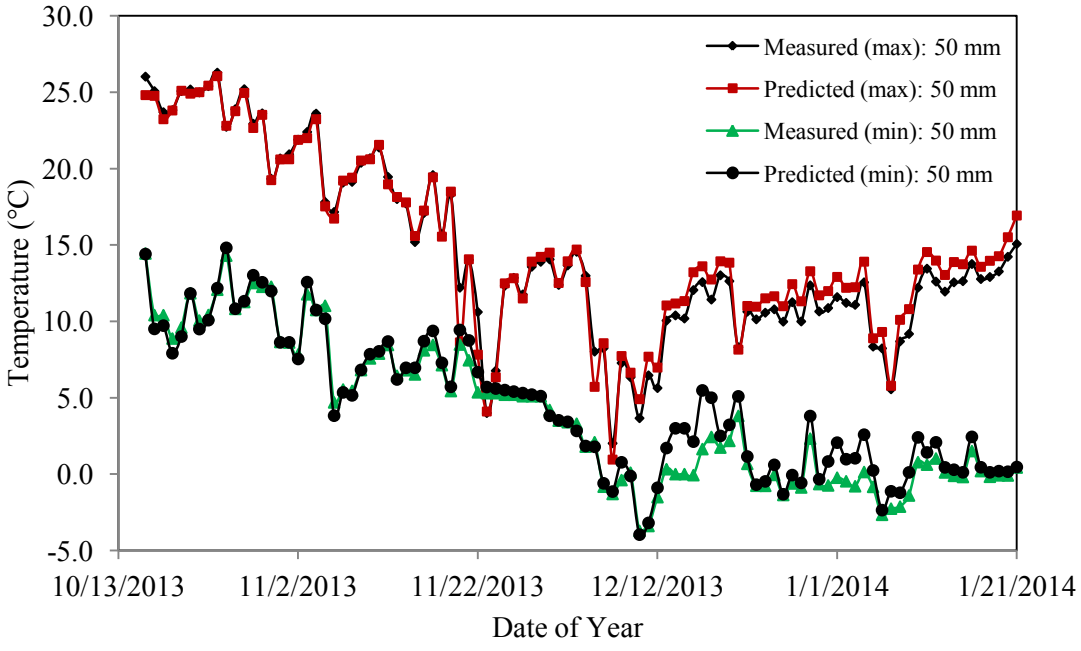

Figure 26. Predicted and measured temperatures at 50 mm depth of AC

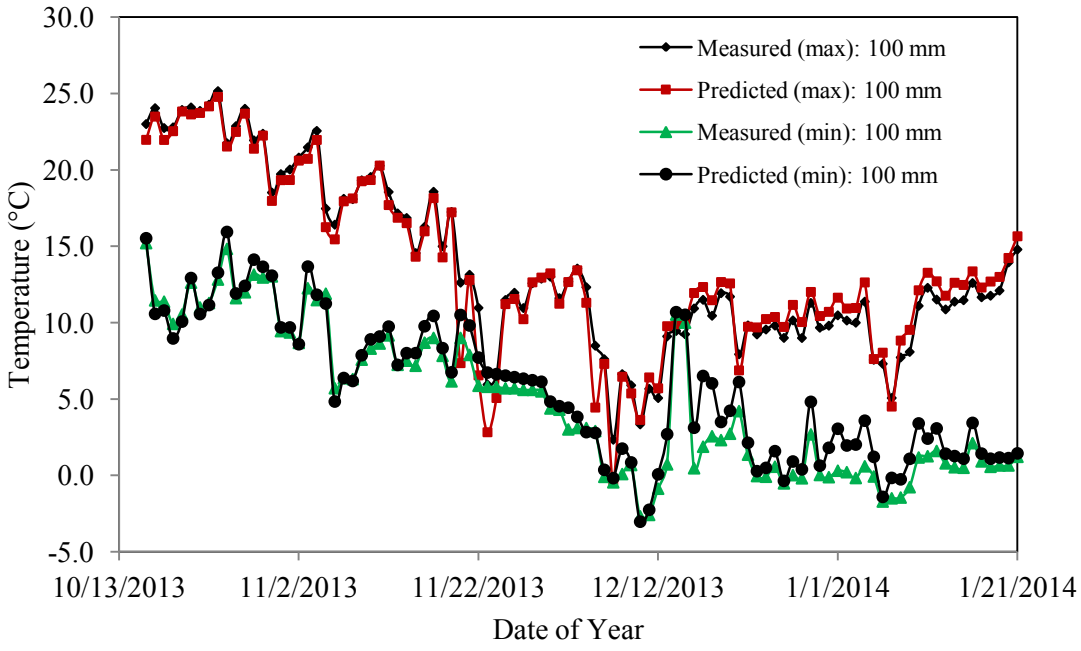

Figure 27. Predicted and measured temperatures at 100 mm depth of AC

ANOVA test was conducted to evaluate the developed models. The null hypothesis was that the mean values are equal and the alternative hypothesis was that the means are not equal. The minimum, the average and the maximum predicted and measured temperatures at 50 mm depth for the period of October 15, 2013 to January 21, 2014 were compared. The ANOVA test produces *p*-values of 0.96, 0.12 and 0.89 for the minimum, the average and the maximum predicted and measured temperatures respectively. All the *p*-values were much greater than 0.05. The alternative hypothesis is therefore rejected in favor of the null hypothesis at 95% CI. Therefore, the mean values of the predicted and measured minimum temperatures at 50 mm depth are equal, which verifies the developed model.

3.5.1.3.6 Discussion

This study developed regression models to determine the maximum, the minimum and the average temperatures at any depth of AC in an asphalt pavement. The maximum, the minimum and the average temperatures at any depth of AC can be determined if the surface or the air temperature is available. However, the actual temperature of the pavement at specific period of time was not investigated. In addition, the models were developed based on temperature measurements obtained from a single pavement section in New Mexico.

3.5.2 Discussion on Determining Temperature Fluctuation

Two types of models were developed to determine the temperature at any depth of AC in a pavement. Both of the models need the surface temperature as an input. Thus, the inside pavement temperature can be found using these two models if the surface temperature is known. These results are also available in the study of Islam et al. (2015a). The AASHTOWare Pavement ME Design Software also shows the temperatures at surface and different layers of AC (not at the bottom of AC). The surface temperature can be used to determine the temperature at the bottom of AC. In the current study, only the regression model has been used for its simplicity.

CHAPTER FOUR

TEMPERATURE-INDUCED FATIGUE MODEL DEVELOPMENT

4.1 General

The development of the closed form equation (Thermal Fatigue Model) for determining allowable number of cycle (N_{ft}) due to specific temperature fluctuation is discussed in this chapter. The fundamental form of Eq. 2 is presented in Fig. 28. For a given ε, N_{ft} was determined as a function of E. Now, E varies with given temperature and frequency. Therefore, laboratory beam fatigue tests were conducted at different temperatures, frequencies and strain levels to generate the data. However, the beam fatigue test (by the mechanical loading) was correlated with the axial fatigue test (by actual temperature loading).

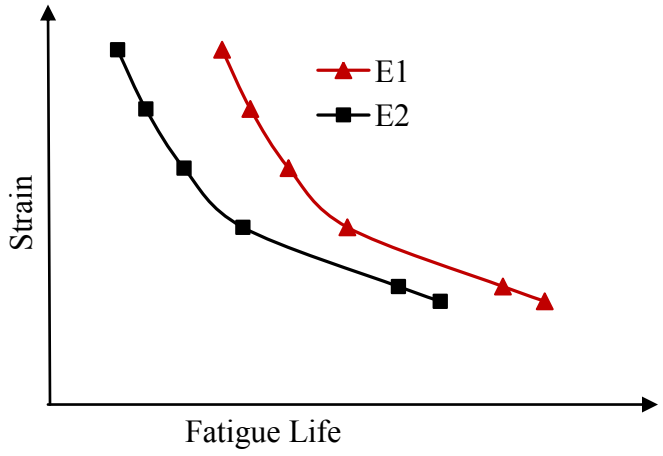

Figure 28. Schematic of fatigue test result

4.2 Materials

Three different SP mixtures, listed in Table 7, were used to develop the temperature-induced fatigue model in the current study. The mixtures are described below:

Mixture 1: This mixture was collected while paving the I-40 instrumentation section in cooperation with the NMDOT. It was a SP-III HMA mixture with basalt aggregate. The mixture had a binder of PG 76-22 an amount of 4.4% by the weight of the mixture. The specific gravity of the binder was 1.014.

Table 7. Materials used to develop the model

Mixture No.	Mixture Type	HMA/WMA	Binder Type	Binder Content (%)	Aggregate Type
1	SP-III	HMA	PG 76-22	4.4	Basalt
2	SP-III	HMA	PG 70-22	4.7	River deposits
3	SP-IV	WMA	PG 76-22	4.7	Gravel

The bulk specific gravity (G_{mb}) testing was performed on AC beam samples according to the AASHTO T 166-07 (2007) standard. For the aggregates, it ranged between 2.571 and 2.868. This mixture had 35% RAP materials from two sites in NM, Budagers and West Central. The G_{mb} of RAP materials varied from 2.685 to 2.751. The theoretical maximum specific gravity (G_{mm}) of the loose HMA mixtures was determined by using the AASHTO T 209-05 (2007) standards and found to be 2.573. The nominal maximum aggregate size of the aggregate was 19 mm.

Mixture 2: It was a SP-III HMA mixture with river deposit aggregate. The mixture has a binder of PG 70-22 an amount of 4.7% by the weight of the mixture. The

nominal maximum aggregate size of the aggregate was 19 mm. This mixture has 25% RAP material. The specific gravity of the binder was 1.037. The G_{mb} of the aggregates ranged between 2.533 and 2.599. The G_{mb} of RAP material was 2.649. The G_{mm} of the loose HMA mixtures was determined to be 2.459.

Mixture 3: It was a SP-IV Warm Mix Asphalt (WMA) mixture with gravel aggregate. The mixture had a PG binder of PG 76-22 an amount of 4.7% by the weight of the mixture. The nominal maximum aggregate size of the aggregate was 12.5 mm. This mixture has 35% RAP material. The specific gravity of the binder was 1.02. The G_{mb} of the aggregates ranged between 2.573 and 2.624. The G_{mb} of RAP material was 2.801. The G_{mm} of the loose HMA mixtures was determined to be 2.505. The gradations of these mixtures are shown in Fig. 29.

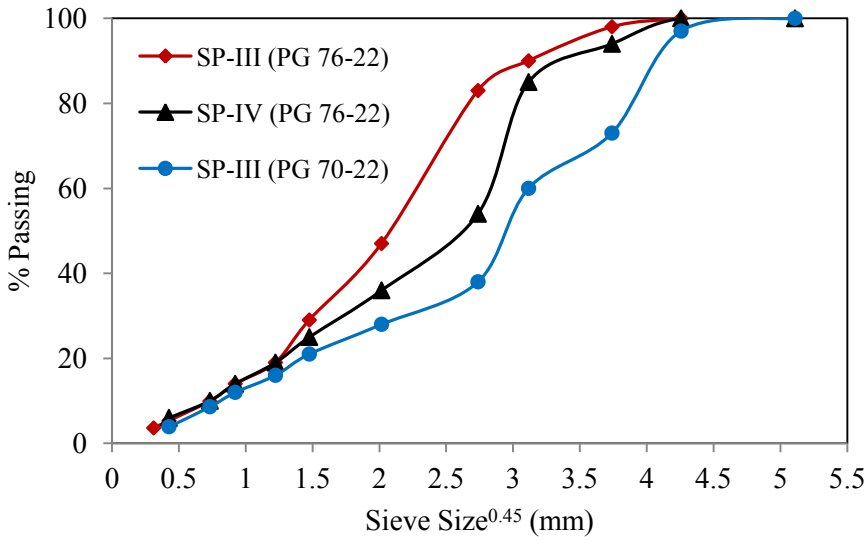

Figure 29. Gradations of aggregates used in AC

4.3 Sample Preparation

The dimensions of the AC beam samples used in laboratory testing are approximately 380 mm x 63 mm x 50 mm (15 in. x 2.5 in. x 2 in.). Samples were compacted to dimensions (450 mm x 150 mm x 75 mm) greater than those shown above using an asphalt beam compactor (due to mold size). The AASHTO T 312 (2007) standard was followed while heating and transferring the HMA mixture. HMA mixtures were heated to 150 °C for no more than one hour and were then compacted using a kneading compactor as shown in Fig. 30(a). Once cooled, the compacted HMA specimens were then cut into two beams (15 in. x 2.5 in. x 2 in.) using a laboratory saw, as shown in Fig. 30(b).

a) Compaction of mixture

b) Cutting the slabs

c) Prepared samples

Figure 30. Beam sample preparation

4.4 Sample Volumetric Properties

The air voids of the samples ranged between 5.2% and 6.1% with an average value of 5.6%. This large air void range was beneficial to the study. This is because, difference in air void produced difference in initial stiffness and fatigue life which yielded better correlation between fatigue life and stiffness.

4.5 Determining Equivalent Laboratory Test

Change in temperature causes thermal expansion and compression of AC in axial mode. Therefore, it is ideal to develop the fatigue model by applying cyclic temperature (causing thermal expansion and compression) on constrained sample and measure the stiffness after different cycles of thermal expansion and compression. However, applying cyclic temperature load on a restrained sample is extremely difficult and time consuming. Therefore, the relationship between the damages caused due to the beam fatigue test by the mechanical loading and axial fatigue test by the temperature loading was developed first. Then mechanical load in a beam fatigue fashion was applied to create similar effect of thermal expansion and contraction.

For further clarification, Fig. 31 shows the ideal test schematic where a temperature difference (ΔT) is applied on the restrained beam sample. This applied ΔT creates thermal stress axially in the restrained sample. In the current study, an equal amount of stress is created using beam fatigue test by applying equivalent strain (ε) produced by ΔT. The equivalent strain (ε) can be computed by the product of α and ΔT if only 1D is considered at this stage. Note that α-value is temperature dependent. Biaxial tension in AC slab may be considered in future studies.

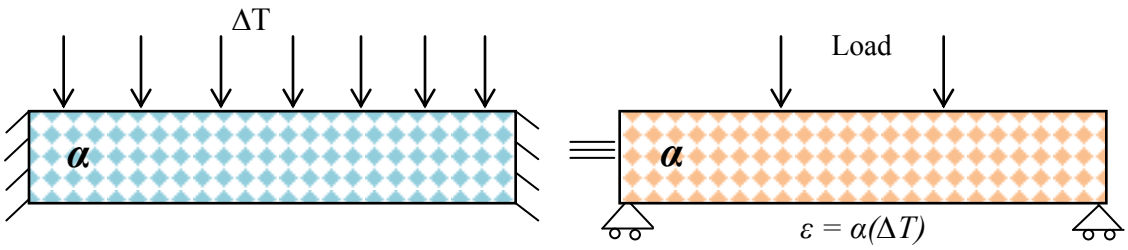

Figure 31. **Test scheme versus the ideal test setup**

The correlation between the beam fatigue test by the mechanical loading and axial fatigue test by the temperature loading was investigated in the laboratory. Four beam samples were sealed and restrained with wood as shown in Fig. 32. Then, the restrained samples were exposed to temperature load in a precise environmental chamber. Each temperature cycle consists of 12 hours of heating and 12 hours of cooling with reference to the mean temperature. The first 2 hour period is required for the temperature to reach to the inside of the sample. The mean temperature was 20 °C; an increase and decrease of 10 °C from 20 °C were applied for 10 cycles (one temperature cycle per day).

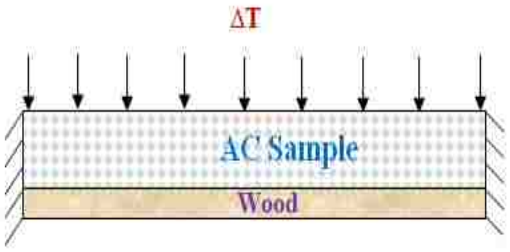

a) Schematic of the restrained sample

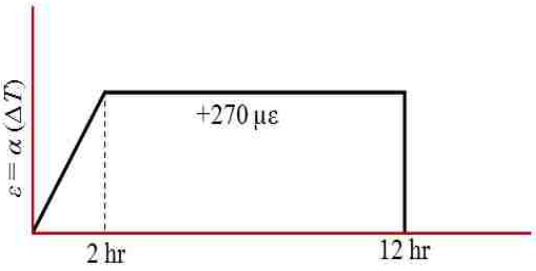

b) Applied temperature loading

c) Restraining the samples with wood

d) Applying cyclic temperature

Figure 32. **Correlation between the actual temperature and mechanical loading**

The average α-value at 20±10 °C has been obtained to be 27 με/°C. The expansion and contraction of the restraining wood was measured to be 7.4 με/°C. This means the effective thermal strain obtained by the sample is 19.6 με/°C (27-7.4 με/°C). The area under the 12 hour period loading, shown in Fig. 32(b), is 2156 με-hour. The stiffnesses of the conditioned samples were measured after 10 days of temperature loading.

On the other hand, equivalent strain (540 με peak-to-peak) was applied to other four beam samples using the beam fatigue test apparatus at 1.16×10^{-5} Hz (one cycle per day)

sinusoidal loading at 20 °C for 10 cycles. The area under the 12 hour period loading is 2063 με-hour, which is 4% less than 2156 με-hour applied in temperature loading. The stiffnesses of the restrained samples before loading and after 10-day of the beam fatigue loading were measured. Note that the α-values (με/°C) at the different temperatures (°C) have been determined using the following Eq. 16 which has been developed for the same mixture:

Fig. 33(a) shows the stiffness ratios of samples for both the beam fatigue by the mechanical loading and axial fatigue by the temperature loading tested at an average temperature of 20 °C. Here, stiffness ratios means the ratio of stiffnesses after and before the 10-day loading; Regarding the temperature of 20 °C, the beam fatigue by the mechanical loading was conducted at 20 °C and the axial fatigue by the temperature loading was conducted at an average temperature of 20 °C. Fig. 33(a) shows that the stiffnesses of AC samples decreases to 86.7% and 87.2% due to the axial fatigue test by the temperature and beam fatigue test by the mechanical loading respectively. The decrease in stiffness is almost equal for both cases (86.7% versus 87.2%).

Statistical *t*-test was conducted to evaluate these two damage ratios with the null hypothesis of "true difference between the means of stiffness ratios of beam fatigue test by the mechanical loading and axial fatigue test by the temperature loading is zero". The *p*-value (probability of null hypothesis to be true) was found to be 0.84 which is 1580% greater than 0.05 (5%). Therefore, the null hypothesis is true and these two values (86.7% and 87.2%) are statically equal at 95% CI. Finally, in the rest of the study it is considered

that the damages due to the beam fatigue test by the mechanical loading and axial fatigue test by the temperature loading are equal. It might be possible that the difference between the beam fatigue test by the mechanical loading and axial fatigue test by the temperature loading is significant after large number of cycles. However, the developed model was calibrated with field condition which can take care of the uncertainty.

The above mentioned test was also conducted at 12 °C; an increase and decrease of 10 °C from 20 °C were applied for 10 cycles (one temperature cycle per day). The average α-value at 20±10 °C was obtained to be 25.6 με/°C. The effective thermal strain obtained by the sample is 18.2 με/°C (25.6-7.4 με/°C). The area under the 12 hour period loading is 2002 με-hour. On the other hand, equivalent strain (520 με peak-to-peak) was applied to other four beam samples using the beam fatigue test apparatus at 1.16×10^{-5} Hz (one cycle per day) sinusoidal loading at 12 °C for 10 cycles. The area under the 12 hour period loading is 1986 με-hour, which is 1% less than 2002 με-hour applied in temperature loading. The stiffnesses of the restrained samples before loading and after 10-day of the beam fatigue loading were measured.

Fig. 33(b) shows the stiffness ratios of samples for both the beam fatigue by the mechanical loading and axial fatigue by the temperature loading tested at an average temperature of 12 °C. At this temperature, only three samples have been tested for both the beam fatigue by the mechanical loading and axial fatigue by the temperature loading. Fig. 33(b) shows that the stiffnesses of AC samples decreases to 82% and 82.4% due to

the axial fatigue test by the temperature and beam fatigue test by the mechanical loading respectively. The decrease in stiffness is almost equal for both cases (82% versus 82.4%).

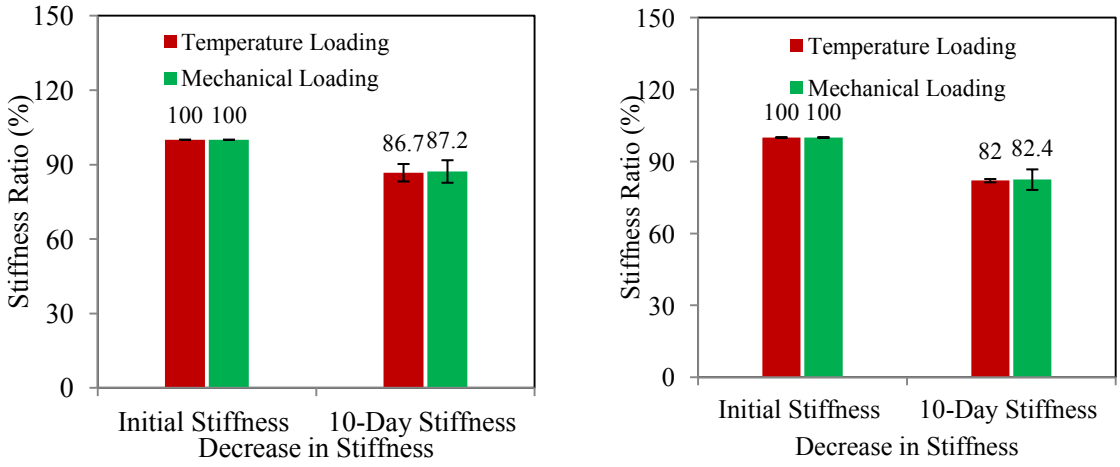

a) At 20 °C b) At 12 °C

Figure 33. Beam fatigue (mechanical) versus axial thermal fatigue damage

4.6 Laboratory Testing

Prior to testing, each sample was conditioned to test temperature, 20 °C, using an environmental test chamber for 2 hours. Beam fatigue tests were conducted at three different temperatures (-10 °C, 20 °C and 40 °C) and at three different strain levels (200 με, 500 με and 1000 με) at 0.01 Hz of sinusoidal loading. The usage of sinusoidal loading means the day-night temperature cycle was considered sinusoidal with the horizontal axis at the middle of loading. The possible residual stress in AC slab which might occur due to the sudden decrease in temperature while compaction was not considered. In addition, each day temperature was considered heating and each night temperature was considered cooling although the AC slab might be in cold zone in whole winter and hot zone in whole summer. The temperature range and strain levels used in the

study cover the variations possibly occur in real pavement. The reason for testing at 0.01 Hz of loading is described later.

A total of 75 beam samples were tested to develop the model. Two to five replicate samples were tested to obtain consistent results. The test matrix is shown in Table 8. Tests which took more than 15 days (13,000 of cycles) to finish, were stopped and the data were extrapolated using the Weibull Function. This function shows excellent performance to predict the number of cycle to cause failure of a sample using extrapolation (Prowell et al. 2008, Tarefder and Barlas 2013). Sometimes the tests were conducted at 1 Hz and deduced the results for 0.01 Hz. The full test program took almost three years to finish. The sample geometry and support conditions were adopted following the AASHTO T 321-07 (2007) test standard.

Table 8. Test matrix

Strain Level	40 °C	20 °C	-10 °C
200 με	x	x	x
500 με	x	x	x
1000 με	x	x	x

The test setup and a typical test result are shown in Fig. 34. The samples were clamped to the loading frame in a way they were compacted. If the upside of the beam sample is turned into down it may produce erroneous stiffness as observed in of the previous studies (Islam et al. 2012, Islam et al. 2014a).

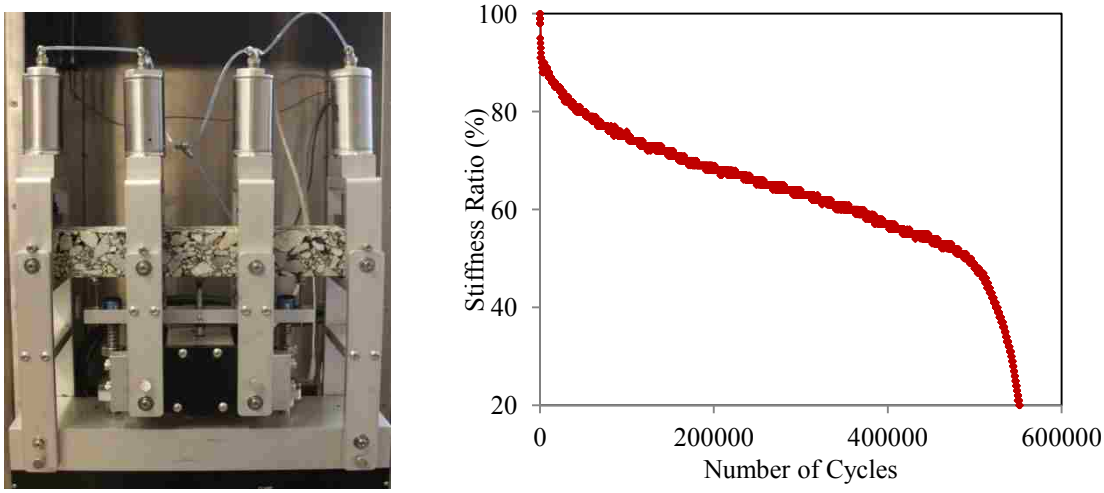

a) Test setup b) Test results

Figure 34. Four-point bending test

4.6.1 Frequency of Loading

It is a well established phenomenon that behavior of AC is frequency dependent. However, recent study shows that performance of AC is also frequency dependent (Islam et al. 2015b). Therefore, careful consideration of loading frequency is essential. The reason of conducting the tests at 0.01 Hz (instead of 1.16×10^{-5} Hz) is described herein. The fatigue life of AC decreases with the decrease in frequency of loading at any strain level. This behavior was also observed by Mannan et al. (2015). However, the fatigue life becomes stable at the frequency of equal or lower than 0.01 Hz as shown in Fig. 35. Fig. 35(a) shows the fatigue life of AC tested at different strain levels. It can be observed that fatigue life becomes stable at a frequency of 0.01 Hz or less for any strain level. For instance, the fatigue lives of AC samples are 3740, 2570, 970, 701 and 713 at frequencies of 10 Hz, 1 Hz, 0.1 Hz, 0.01 Hz and 0.001 Hz, respectively, tested at 20 °C and 1000 με of loading. That means the fatigue lives are almost equal (701 versus 713) at 0.01 Hz and

0.001 Hz of loading. It is considered that the fatigue life at lower frequency of loading (for example, $1.16x10^{-5}$ Hz) is equal to that of 0.01 Hz of loading.

Similar observation was made when the tests were conducted at different temperatures as shown in Fig. 35(b). The fatigue life becomes stable at a frequency of 0.01 Hz or less for different temperatures at 500 με of loading. This behavior may due to the healing behavior of AC. At low frequency of loading, load sustains on sample for longer time and damage produces is higher due to viscoelastic nature of AC. On the other hand, material gets greater time to heal at slower loading rate. Combining these two effects, the fatigue life becomes stable at a frequency of 0.01 Hz or less. Finally, the fatigue life of AC at $1.16x10^{-5}$ Hz may be obtained reasonably if the test is conducted at 0.01 Hz or less.

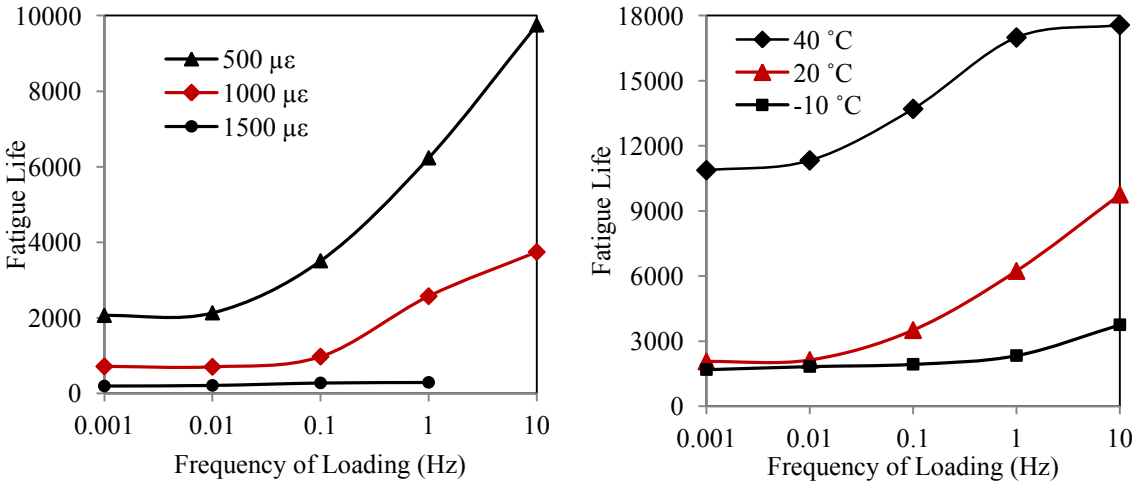

a) Allowable load repetitions at different strain levels at 20 °C.

b) Allowable load repetitions at different temperatures at 500 με.

Figure 35. Effect of loading frequency on the fatigue life of AC

To confirm the above statement further beam fatigue tests were conducted on AC samples at 0.01 Hz and $1.16x10^{-5}$ Hz of loading for ten cycles at 20 °C and 12 °C. A total of four samples were tested for each frequency of loading. The stiffness ratios (ratio of stiffnesses before and after the 10-cycle loading) at 20 °C are presented in Fig. 36. It shows that the stiffnesses of AC samples decreases to 86.1% and 87.2% due to 0.01 Hz and $1.16x10^{-5}$ Hz of loading for ten cycles, respectively, at 20 °C. The decrease in stiffness is almost equal for both cases (86.1% versus 87.2%).

Statistical *t*-test was conducted to evaluate these two damage ratios with the null hypothesis of "true difference between the means of stiffness ratios of beam fatigue tests at 0.01 Hz and $1.16x10^{-5}$ Hz loading is zero". The *p*-value (probability of null hypothesis to be true) was found to be 0.66 which is 1220% greater than 0.05. Therefore, the null hypothesis is true and these two values (86.1% and 87.2%) are statically equal at 95% CI. Finally, in the rest of the study it is considered that the damage due to the beam fatigue at 0.01 Hz and $1.16x10^{-5}$ Hz of loading at 20 °C is considered the equal.

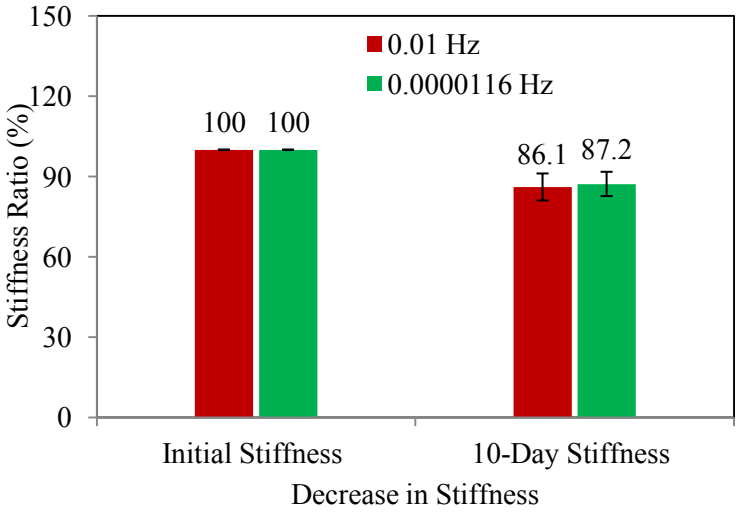

Figure 36. Decrease in stiffness for testing at 0.01 Hz and $1.16x10^{-5}$ Hz (20 °C)

The stiffness ratios (ratio of stiffnesses before and after the 10-cycle loading) at 12 °C are presented in Fig. 37. It shows that the stiffnesses of AC samples decreases to 81.9 % and 82.4% due to 0.01 Hz and $1.16x10^{-5}$ Hz of loading for ten cycles, respectively, at 12 °C. The decrease in stiffness is almost equal for both cases (81.9% versus 82.4%).

Statistical *t*-test was conducted to evaluate these two damage ratios with the null hypothesis of "true difference between the means of stiffness ratios of beam fatigue tests at 0.01 Hz and $1.16x10^{-5}$ Hz loading is zero". The *p*-value (probability of null hypothesis to be true) was found to be 0.21 which is greater than 0.05. Therefore, the null hypothesis is true and these two values (81.9% and 82.4%) are statically equal at 95% CI. Finally, in the rest of the study it is considered that the damages due to the beam fatigue at 0.01 Hz and $1.16x10^{-5}$ Hz of loading at 12 °C are equal.

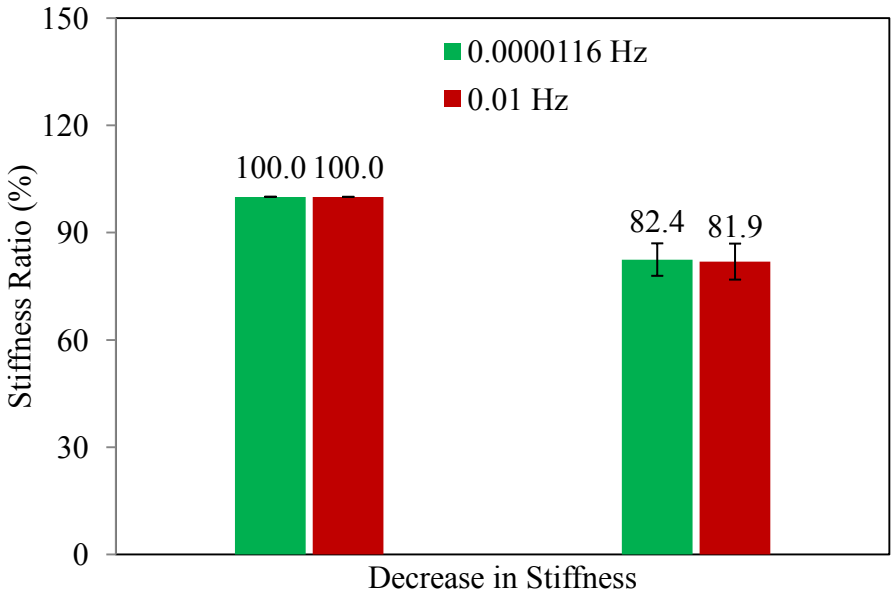

Figure 37. Decrease in stiffness for testing at 0.01 Hz and $1.16x10^{-5}$ Hz (12 °C)

4.6.2 Stiffness of Samples

The stiffness of AC is frequency dependent. The fatigue lives of AC may be equal at 0.01 Hz and $1.16x10^{-5}$ Hz of loading. However, the stiffnesses of AC are not equal at 0.01 Hz and $1.16x10^{-5}$ Hz of loading. Therefore, the stiffnesses of the three types of samples at different temperatures were determined using the beam fatigue apparatus at $1.16x10^{-5}$ Hz of loading. In summary, fatigue life and stiffness of beam samples were measured testing at 0.01 Hz and $1.16x10^{-5}$ Hz of loading respectively.

Now the question is about the initial stiffness of samples. According to the AASHTO T 321 (2007) test protocol, the stiffness at the 50^{th} cycle of loading is considered the initial stiffness. The first 50 cycles is neglected to consider the initial setup and stabilization of the test program. However, one might expect significant damage at the first 50 cycles of loading especially at low frequency of loading.

The effect of low frequency of loading at 20 °C and 500 με is presented in Fig. 38; where the decreases in stiffness ratios are plotted due to loading from 0.0001 Hz to 10 Hz. The vertical dash line cuts the stiffness ratio at the 50^{th} cycle of loading. It can be observed that the stiffnesses decrease to about 84%, 80%, 72%, 68% and 64% for the frequencies of 10 Hz, 1 Hz, 0.1 Hz, 0.01 Hz and 0.001 Hz respectively. The decrease in stiffnesses especially at 0.1 Hz, 0.01 Hz and 0.001 Hz are quite large. In addition, the test stabilizes within 5 cycles of loading at low frequency of loading such as 0.01 Hz. Therefore, this study considers the initial stiffness at the 5^{th} cycle of loading for the testing at 0.01 Hz.

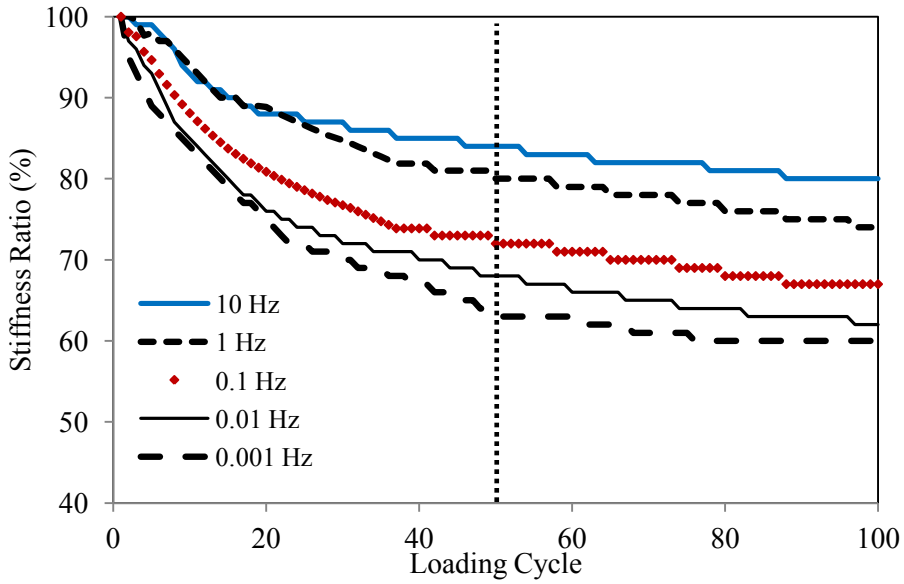

Figure 38. Decrease in stiffness with number of loading at 500 με

4.7 Test Results and Model Development

Fig. 39 presents the beam fatigue test results for all the three mixtures. It shows that the fatigue life of AC decreases with an increase in applied strain. This is expected; larger load produced more damage. For instance, the fatigue lives of SP-III (PG 76-22) mixture at 1000 με and 200 με are 643 and 90250, respectively, at 20 °C. Regarding the effect of temperature, the fatigue life decreases at lower temperature and vice versa. This is also expected; stiffness of AC is higher at lower temperature and stiffer material fails earlier in controlled-strain fatigue test. For example, the fatigue lives of the above mentioned mixtures are 953 and 306 at 40 °C and -10 °C, respectively, at 1000 με of loading. Similar effect was observed for all three mixtures. Another feature of the test data presented in Fig. 39 is that the test data is scattered. This is because, the results are obtained from testing AC samples at three different temperatures.

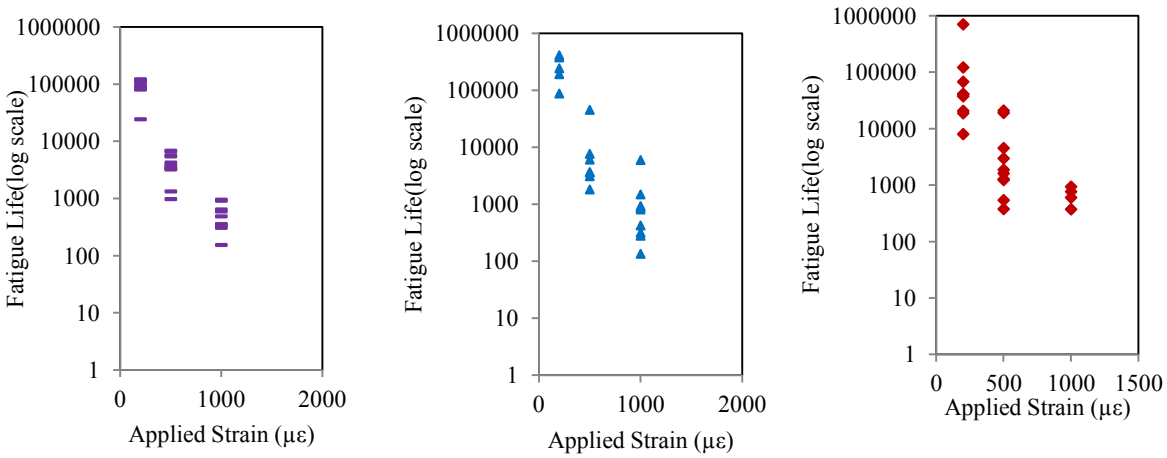

a) SP-III (PG 76-22) b) SP-III (PG 70-22) c) SP-IV (PG 76-22)

Figure 39. Beam fatigue test results for the three mixtures

A nonlinear least square algorithm was scripted to fit the data presented in Fig. 39. The best regression model is found as follows:

$$N_{ft} = 1.272x10^{-6}\left(\frac{1}{E}\right)^{0.4168}\left(\frac{1}{\varepsilon}\right)^{3.458} \quad (25)$$

$$N_{ft} = 1.272x10^{-6}\left(\frac{1}{E}\right)^{0.4168}\left(\frac{1}{\alpha(\Delta T)}\right)^{3.458} \quad (26)$$

$$N_{ft} = 1.272x10^{-6}\left(\frac{14.696}{E(atm)}\right)^{0.4168}\left(\frac{1}{\alpha(\Delta T)}\right)^{3.458} \quad (27)$$

where E is in psi, $E(atm)$ is in atmospheric pressure, and ε is in strain. The R^2 of the model is 0.79. The model is similar to the AASHTOWare Pavement ME Design model; however, the powers of E and ε are smaller than those of the traffic-induced fatigue model used in the AASHTOWare Pavement ME Design Software.

CHAPTER FIVE

MODEL VALIDATION/CALIBRATION

5.1 General

The thermal fatigue damage was developed using the test data on three different asphalt mixtures. An unknown mixture, which was not used in the model development, was used to validate the model in the laboratory.

5.2 Laboratory Validation/Calibration

The developed model was validated/calibrated in the laboratory using a different asphalt mixture. The fatigue life of the mixture for a particular strain level and temperature was predicted using the developed model. Then, the fatigue life of the mixture for that particular strain level and temperature was measured in the laboratory using the beam fatigue test. Comparing the model prediction and laboratory measurement the developed model was calibrated/calibrated.

5.2.1 Material

The mixture used to verify the developed model was a SP-III limestone mixture with no RAP material in it. The three materials used for developing model had RAP material. The mixture had a PG binder of PG 70-22 an amount of 4.2% by the weight of the mixture. The nominal maximum aggregate size of the aggregate was 19 mm. The specific gravity of the binder was 1.034. The G_{mb} of the aggregates ranged between 2.615 and 2.64. The G_{mm} of the loose HMA mixtures was determined to be 2.478. The gradation of this mixture is shown in Fig. 40.

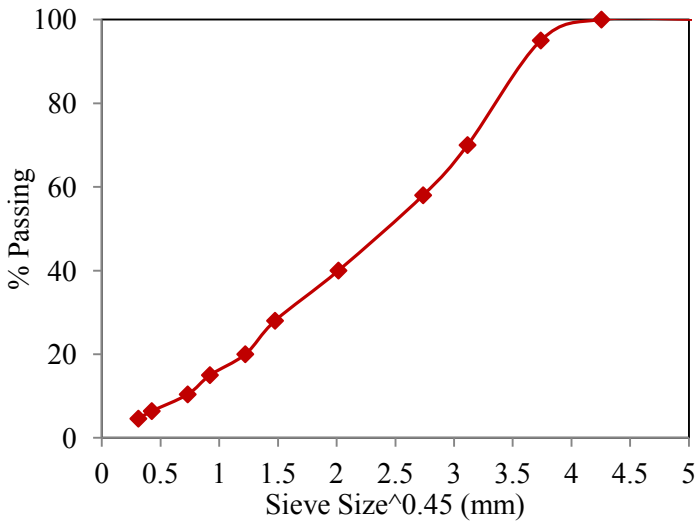

Figure 40. Gradation of the mixture used for laboratory validation

5.2.2 Sample Preparation

Beam samples of approximately 380 mm x 63 mm x 50 mm (15 in. x 2.5 in. x 2 in.) were prepared following the same procedure described in section of "4.3 Sample Preparation". Samples were compacted to dimensions (450 mm x 150 mm x 75 mm) greater than those shown above using an asphalt beam compactor (due to mold size). HMA mixtures were heated to 150 °C for no more than one hour and were then compacted using a kneading compactor. Once cooled, the compacted AC specimens were then cut into two beams (15 in. x 2.5 in. x 2 in.) using a laboratory saw.

5.2.3 Testing

Beam fatigue tests were conducted at 20 °C and 500 με at 0.01 Hz of sinusoidal loading. The sample geometry and support conditions were adopted following the AASHTO T 321-07 (2007) test standard. Prior to testing, each sample was conditioned to test temperature, 20 °C, using an environmental test chamber for 2 hours.

5.2.4 Results and Discussion

The stiffness and fatigue life of the fourth mixture measured using the beam fatigue test is shown in Table 9. The fatigue life of the mixture was also predicted using the developed model. The measured and the predicted fatigue lives were compared to validate the laboratory developed model.

Table 9. Laboratory validation of the developed model

Sample ID	Strain Tested	Measured Stiffness	Measured Fatigue Life	Predicted Fatigue Life	*p*-value of the *t*-test
	(με)	psi			
1	500	338913	1673	1639	
2	500	275403	2195	1787	
3	500	301213	1421	1721	0.32
4	500	311895	1856	1696	
5	500	333065	2248	1651	

Statistical *t*-test was conducted to evaluate these two fatigue lives (measured and predicted) with the null hypothesis of "true difference between the means of measured fatigue life and predicted fatigue life is zero". The *p*-value (probability of null hypothesis to be true) was found to be 0.32 which is greater than 0.05. Therefore, the null hypothesis is true and the measured and the predicted fatigue lives are statically equal at 95% CI. Finally, the developed temperature-induced fatigue model is true for the fourth mixture also.

5.3 Field Validation/Calibration

Field calibration of the laboratory developed model is essential as the laboratory sample size, boundary conditions and other factors are not same to real field condition.

Calibration was done by determining the thermal fatigue damage in a field pavement and comparing the damage to that calculated by the developed model.

5.3.1 Calibration Procedure

Field calibration was conducted by imposing a shift factor (*k*) in the laboratory developed temperature-induced fatigue model as shown in Eq. (28):

$$N_{ft} = (k)1.272x10^{-6}(\frac{1}{E})^{0.4168}(\frac{1}{\varepsilon})^{3.458} \quad (28)$$

where the *k* can be expressed as follows:

$$k = \frac{D_{R(lab)}}{D_{R(field)}} \quad (29)$$

Where $N_{R(lab)}$ and $N_{(field)}$ are the damage index in the laboratory and in the field respectively.

5.3.2 Determining Field Damage Index

To determine the thermal fatigue damage in field, FWD test was conducted on the shoulder (non-trafficked) of I-40 in New Mexico, shown in Fig. 41. The test on shoulder was started in October 2013, once in a month (first week), every hour from 9 am to 3 pm. A total of five points were selected on which fifteen drops are applied at three load levels on each point. The temperatures of the AC at four different depths (surface, 2 in., 4 in. and bottom of AC) were measured using the installed temperature probes at the section. The FWD data was backcalculated using the backcalculation software, ELMOD.

Figure 41.Conduction of FWD test on I-40 pavement

5.3.3 Results

The stiffness results are presented in Fig. 42. It shows that the stiffness of AC decreases from 679 ksi (at 18.34 °C) to 660 ksi (at 18.31 °C) from October 2013 to October 2014. Note that the straight lines in Fig. 42 do not mean that the stiffness decreases linearly with the age; the lines show the starting and end points only. Similarly, the stiffness of AC decreases from 1271 (at 6.54 °C) ksi to 1214 ksi (at 6.54 °C) from December 2013 to December 2014. For January 2014 to January 2015, the stiffness of AC decreases from 1035 ksi (at 4.59 °C) to 997 ksi (at 4.66 °C) respectively. Note that the FWD test could not be conducted in November 2014 due to equipment issue. A one-year damage period has been considered.

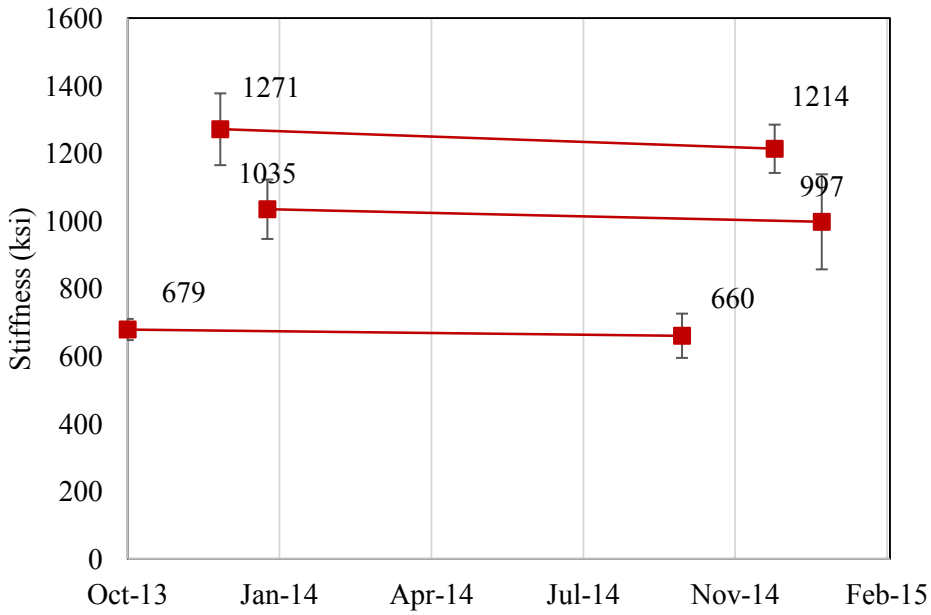

Figure 42. Decrease in shoulder stiffness due to thermal fatigue loading

The field damage ratio ($D_{R(field)}$) was calculated using the following Eq.

$$D_{R(field)} = \frac{\Delta E}{0.5E_o} \tag{30}$$

where ΔE is the decrease in stiffness in one year period and E_o is the stiffness at the starting month. The reason for 0.5 (or 50%) in the denominator is that AC usually fails when the initial stiffness is decreased by 50% (AASHTO T 321-07 2007). The $D_{R(field)}$ has been calculated as 0.05596, 0.08969 and 0.07282 considering the data of October 2013-2014, December 2013-2014, and January 2014-2015 respectively, using Eq. 30. The average $D_{R(field)}$ is found to be 0.07283.

5.3.4 Calculating Laboratory Damage Ratio

The laboratory damage ratio ($D_{R(lab)}$) can be calculated using the following Eq. which is similar to Eq. 1, used by the AASHTOWare Pavement ME Design Software to calculate the traffic-induced fatigue damage index (D_1):

$$D_{R(lab)} = \sum_{i=1}^{q} \frac{n_i}{N_{ft,i}} \tag{31}$$

where N_{ft} is the allowable number of temperature load repetitions in period *i* and *q* is the number of periods in each year. Calculation of $D_{R(lab)}$ for the I-40 shoulder (for which $D_{R(field)}$ has been determined) is shown in Table 10. The monthly average temperature of AC was measured using the installed temperature probes. This average temperature is needed to determine the α-value for that temperature using Eq. 16. Then, the developed thermal strain ($\varepsilon = \alpha \Delta T$) was calculated using the α-value and the measured monthly-average day-night temperature fluctuation (ΔT). It would be better to calculate the daily day-night ΔT instead of monthly average which is very time consuming. The stiffness of AC materials at 1.16×10^{-5} Hz was determined in the laboratory. The damage ratio for each month has calculated for each month and finally summed up to 0.00083 per year. It would also have been better to calculate the damages at different depths and determine the average damage, which would be pursued in future research.

Table 10. Calculating laboratory damage ratio due to thermal fatigue loading

Month	Average Temperature of AC	α (Eq. 16)	Monthly Avg. ΔT	Strain ($\varepsilon = \alpha(\Delta T)$)	E at 1.16x10^{-5} Hz	N_{ft}	n	$\frac{n}{N_{ft}}$
	°C	με/°C	°C	με	psi			
January	4.49	24	2.7	65	150649	2648281	31	1.17E-05
February	9.22	25	3.5	89	146726	910819	28	3.07E-05
March	16.08	27	4.12	110	94430	517287	31	5.99E-05
April	22.30	28	4.7	130	76636	323987	30	9.26E-05
May	28.73	28	4.9	137	52057	316674	31	9.79E-05
June	35.55	28	5.4	150	40263	258310	30	0.000116
July	35.69	28	5.3	147	38276	281770	31	0.00011
August	34.95	28	5.03	140	41359	324844	31	9.54E-05
September	30.66	28	4.6	128	46073	414597	30	7.24E-05
October	22.04	28	4.2	116	61880	524119	31	5.91E-05
November	16.02	27	3.7	99	109798	705391	30	4.25E-05
December	7.90	25	3.6	90	161396	831433	31	3.73E-05
	$D_{R(lab)} = \sum_{i=1}^{q} \frac{n_i}{N_{ft,i}}$ per year							0.00083

5.3.5 Determining the Shift Factor

The laboratory to field calibration factor, k of the developed model (N_{ft}) was found to be 0.01134 using the Eq. 29. Finally, the developed model became as follows, which was calibrated for field condition:

$$N_{ft} = (k)1.272x10^{-6}(\frac{1}{E})^{0.4168}(\frac{1}{\varepsilon})^{3.458}$$

$$N_{ft} = 1.4423x10^{-8}(\frac{1}{E})^{0.4168}(\frac{1}{\varepsilon})^{3.458} \text{ or}$$

$$N_{ft} = 1.4423x10^{-8}(\frac{1}{E})^{0.4168}(\frac{1}{\alpha(\Delta T)})^{3.458} \text{ or}$$

$$N_{ft} = 1.4423x10^{-8}(\frac{14.696}{E(atm)})^{0.4168}(\frac{1}{\alpha(\Delta T)})^{3.458}$$

There are several limitations in the field calibration of the developed temperature-induced fatigue model. Firstly, the environmental factors on AC damages were neglected based on the previous laboratory findings (Islam and Tarefder 2015c, Islam and Tarefder 2015d). Those studies showed that the damage due to aging, environmental factors such as moisture, freeze-thaw etc. are prominent during the initial stage of conditioning. For example, the effect of aging on the stiffness of AC occurs during the first year of conditioning; the FWD test on the pavement was started when the pavement was more than two years. The second issue is that the calibration was conducted using a single pavement. The damage is typically high at the beginning and slows down with time. However, the Miner's law assumes the damage as linear. This might be a reason, the field damage is found higher (k value lower than 1) than the laboratory determined damage. Long-term monitoring of the damage was needed for better comparison.

CHAPTER SIX

MODEL TESTING

6.1 General

The developed temperature-induced fatigue model was used to predict alligator cracking to evaluate its performance and possible contribution in research. The errors of predicting alligator cracking under traditional approach and using the developed model were compared. The detail of the procedure is discussed step by step.

6.2 Alligator Cracking Prediction Procedure

Before discussing the predicted alligator cracking, it is better first to discuss the procedure for the prediction of the alligator cracking using the traditional AASHTOWare Pavement ME Design Software. The design starts with inputting the data in a user-friendly window. Then the analysis is run, and the output is presented in Excel worksheets. The procedure, which is needed to predict cracking for flexible pavements, follows certain steps which are summarized below:

a) **Organize the input data.** All inputs needed for the analysis are tabulated. In the current study, the inputs of the simulations were obtained from the LTPP database. Few cases where data is not available in the LTPP database, the default AASHTOWare Pavement ME Software values were used. Regarding the Poisson's Ratio (v), the AASHTOWare Pavement ME Design Guide uses two types of v-value; a constant value of 0.35 or the relationship between the v-value and the dynamic modulus. A study by the author shows that v-value is not

constant for AC (Islam et al. 2015d). Thus, the consideration of *v*-value of 0.35 is not so reasonable. This is why, the current study uses the relationship between the *v*-value and the modulus.

b) **Process traffic data**. The processed traffic data is then processed to determine equivalent number of single, tandem, and tridem axles produced by each passing of tandem, tridem, and quad axles at different periods of analysis.

c) **Process temperature data**. The hourly pavement temperature profiles are generated using the Enhanced Integrated Climatic Model (EICM) for each month.

d) **Process monthly moisture data.** The effects of seasonal changes in moisture conditions on base and subgrade modulus are also determined using the EICM model.

e) **Sub-layering of pavement structure**. The pavement structure is subdivided into smaller sublayers to account for changes in temperature and frequency in the asphalt layers. The unbound layers are also subdivided to determine the moisture-dependent layer modulus and subsequently the distresses.

f) **Calculate stress and strain.** The developed tensile strains are then calculated for each load, load level, load position, and temperature difference for each month within the design period at the bottom of each asphalt layer. The complex modulus of AC is expressed as a function of the mix properties, temperature, and time of the load pulse. Knowledge of the predicted tensile strain at any point, along with the layer dynamic modulus and fatigue life repetition relationship, allows for the direct calculation of the damage for any asphalt layer.

g) **Calculate fatigue cracking.** Calculate the cracking for each layer from the predicted damage.

6.3 Model Application Procedure in the AASHTOWare Design Guide

The AASHTOWare Pavement ME Design Guide uses field calibrated model to predict the alligator cracking in asphalt pavement. The field calibration was conducted in two steps. In the first step, the predicted alligator cracking data using the Asphalt Institute's Model was compared with the field measured cracking data from LTPP. By minimizing the errors, a revised model was generated. That revised model is currently being used by the AASHTOWare Pavement ME Design Guide. Secondly, different shift factors (ranges 0.000398 to 0.004) based on the thickness of AC were used in the AASHTOWare Pavement ME Design Guide while calculating the Damage Ratio (D_1) (El-Basyouny and Witczak 2005a,b). Note that 'Damage Ratio' is very often termed as 'Damage Index' or simply, 'Damage' in the literature. Then an empirical model is used to predict the amount of alligator cracking using damage index and thickness of asphalt layer of the pavement. The AASHTOWare Pavement ME Design model to correlate the damage with the amount of cracking is presented earlier (Eq. 14) as follows:

$$FC = (\frac{1}{60})\frac{C_4}{1+e^{-2C_2+C_2\log(D_1\%)}}$$

where C_2 can be expressed as:

$$C_2 = -2.40874 - 39.748(1+h)^{-2.856}$$

where *FC* is the area of alligator cracking (percentage of total lane area); *h* is the AC thickness (in.) and C_4 is a regression coefficient (typically 6000). The summation of the measured alligator cracking was divided by the total area of the lane (12 ft. *x* 500 ft. = 6,000 ft^2) to calculate the measured percentage area cracked.

The AASHTOWare Pavement ME Design Software calculates the traffic-induced fatigue damage index (D_1) using Eq. 1 as discussed earlier. After calculating the damage ratio ($D_2 = \sum_{i=1}^{q} \frac{n_i}{N_{ft,i}}$) for thermal fatigue, the total damage index (*D*) can be calculated as:

$$D = D_1 + D_2 \tag{32}$$

Note that both D_1 and D_2 are multiplied by the damage shift factor, ranges 0.000398 to 0.004 based on the thickness of AC. Then, the amount of fatigue cracking (considering thermal fatigue also) can be determined using the following Eq.:

$$FC = (\frac{1}{60}) \frac{C_4}{1 + e^{-2C_2 + C_2 \log(D\%)}} \tag{33}$$

This means the current study proposes to replace the traffic-induced damage index, D_1 by the total damage index, *D*. To summarize, the whole procedure can be written as:

Step 1: Take the average temperatures at the different periods (say, months) of analysis.

Step 2: Calculate the α-values at the different periods of analysis using Eq. 16.

Step 3: Predict the maximum temperature (y_{max}) (Eq. 18) and the minimum temperature (y_{min}) (Eq. 20) at the bottom of AC using the surface maximum and the minimum temperatures obtained from the AASHTOWare Pavement ME Design output. Then, the average temperature fluctuation for that period can be determined by $\Delta T = y_{\max} - y_{\min}$.

Step 4: Determine the developed thermal strain, $\varepsilon = \alpha \Delta T$.

Step 5: Take the stiffness of AC from the AASHTOWare Pavement ME Design output. It is ideal to determine the stiffness for 1.16×10^{-6} Hz.

Step 6: Predict the allowable number of load repletion for temperature fluctuations for a specific period using the developed model

$$(N_{ft} = 1.4423 x 10^{-8} (\frac{1}{E})^{0.4168} (\frac{1}{\varepsilon})^{3.458}).$$

Step 7: Determine the damage ratio ($D_2 = \sum_{i=1}^{q} \frac{n_i}{N_{ft,i}}$) for thermal fatigue damage.

Step 8: Apply the damage shift factor from Table 2. This is because, it is applied by the AASHTOWare Pavement ME Design in the traffic related fatigue damage.

Step 9: Determine the total damage index ($D = D_1 + D_2$).

Step 10: Determine the amount of alligator cracking

$$(FC = (\frac{1}{60}) \frac{C_4}{1 + e^{-2C_2 + C_2 \log(D\%)}}).$$

The contribution of the model has been determined by analyzing randomly chosen LTPP test sections. The research methodology to determine the contribution of the model is presented in Fig. 43 which can be described as follows:

Step 1. Measured performance data were collected for all the 34 chosen sections from the LTPP database.

Step 2. Simulation runs were performed using the AASHTOWare Pavement ME Software to determine the performance predicted by the AASHTOWare Pavement ME Software. The inputs of the simulations were obtained from the LTPP database. Few cases where data is not available in the LTPP database, the default AASHTOWare Pavement ME Software values were used. The obtained prediction from this step is due to the traffic-induced fatigue damage.

Step 3. The predicted damage by the AASHTOWare Pavement ME Software was correlated to the measured cracking obtained from the Step 1. The Root Mean Square of Error (RMSE) was then determined using the MATLAB.

Step 4. Manual calculation was made to predict the performance based on Eq. 28 using the D instead of the D_1. The predicted damage was correlated to the measured cracking from the Step 1. This prediction represents the prediction obtained by using both traffic- and temperature-induced fatigue damages.

Step 5. The predicted damage from the Step 4 considering both the traffic- and temperature-induced fatigue was correlated to the measured cracking obtained from the Step 1 to determine the RMSE using the MATLAB.

Step 5. The RMSE, from the Step 3 and the Step 5 were compared to determine the performance of the developed model.

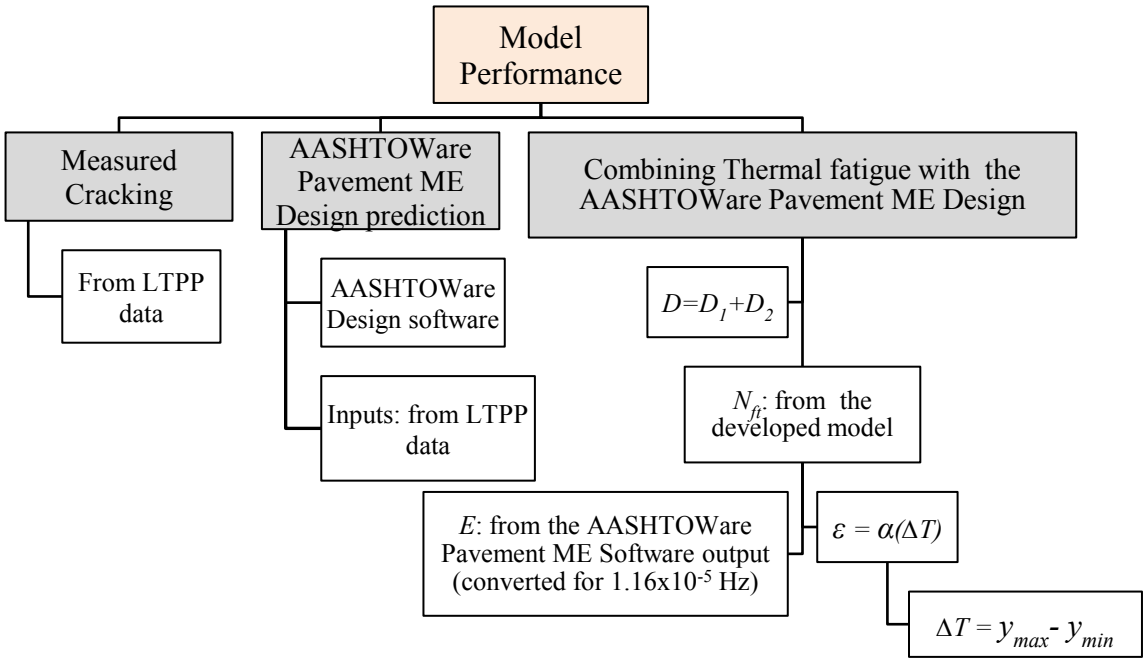

Figure 43. Methodology to determine the contribution of the developed model

The day-night temperature difference (ΔT) is required to determine the thermal strain due to the day-night temperature fluctuations. The AASHTOWare Pavement ME Design Software does not analyze the temperature at the bottom of AC. The maximum (y_{max}) and the minimum (y_{min}) temperatures (ºC) at the bottom of AC in any day were determined using the following models (Eqs. 18 and 20) as discussed earlier.

$$y_{max} = 0.8 + 0.87x_{max} - 25.6x$$

$$y_{min} = 1.84 + x_{min} + 20x$$

where x_{max} = daily maximum surface temperature (°C) obtained from the AASHTOWare Pavement ME Design Software output; x_{min} = daily minimum surface temperature (°C) obtained from the The AASHTOWare Pavement ME Design Software output and x = AC thickness (m). The α-values (με/°C) at the different temperatures were determined using the following Eq. 16 which is presented again:

$$\alpha = -0.006T^2 + 0.356T + 22.633$$

6.4 Collecting Measured Cracking Data

Data were obtained from the LTPP website (www.infopave.com) (LTPP 2015). While choosing the LTPP sections, the field sections were selected randomly to ensure that a well-balanced matrix of pavement parameters, climate, traffic and most importantly, fatigue cracking was present. These projects included varying climates, traffic levels, subgrade soils, and pavement structural cross-sections. Few cases, some parameters were not found; these values were assumed the default ones from the AASHTOWare Pavement ME Design Guide.

The test sections cover a diverse range of site features. All data required for executing the models, including the model inputs and measures of fatigue distress, were extracted, reviewed for accuracy and completeness, and incorporated into a project database. These data elements included performance observations (measurements of distress), material properties, traffic and climatic characteristics, pavement cross-section, foundation, and

many others. Fig. 44 shows the 19 States from where 34 LTPP sections were chosen. It covers almost the whole US and different climates, AC thickness and amount of cracking.

Figure 44. **US States from where LTPP sections were chosen (circled)**

Fig. 45 shows the frequency distribution of alligator cracking for the chosen sections. It shows that 169 data points have cracking values between 0 and 5%.

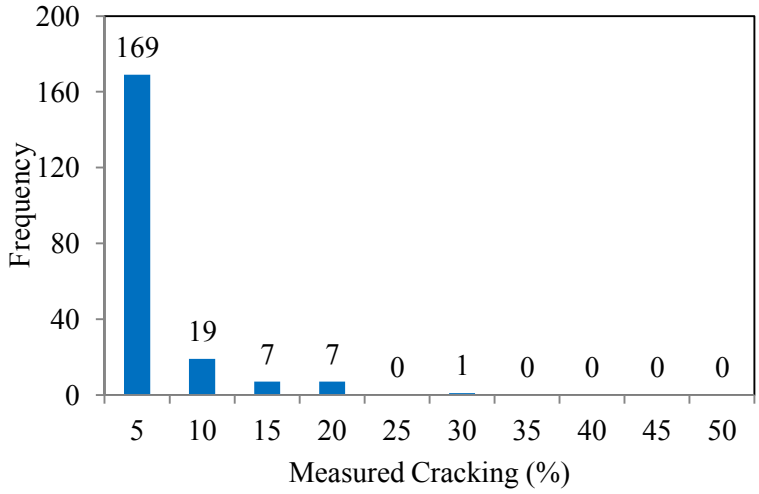

Figure 45. Number of section with cracking amount

The measured cracking with the thickness variations of the chosen sections are shown in Fig. 46. It shows that the chosen array of section has almost all kinds of AC thickness.

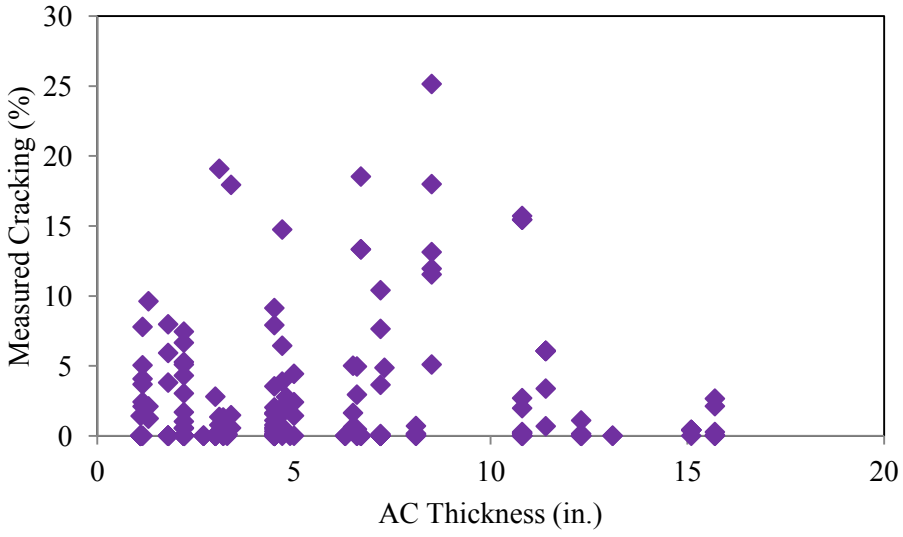

Figure 46. Measured cracking data with AC thickness

The measured cracking data are also correlated with the Mean Annual Average Temperature (MAAT) as shown in Fig. 47. It shows that the MAAT varies between 2.9 °C and 24.1 °C. This is important that the chosen section covers a wide range of air temperature. Another feature is that the cracking data is not correlated with the MAAT.

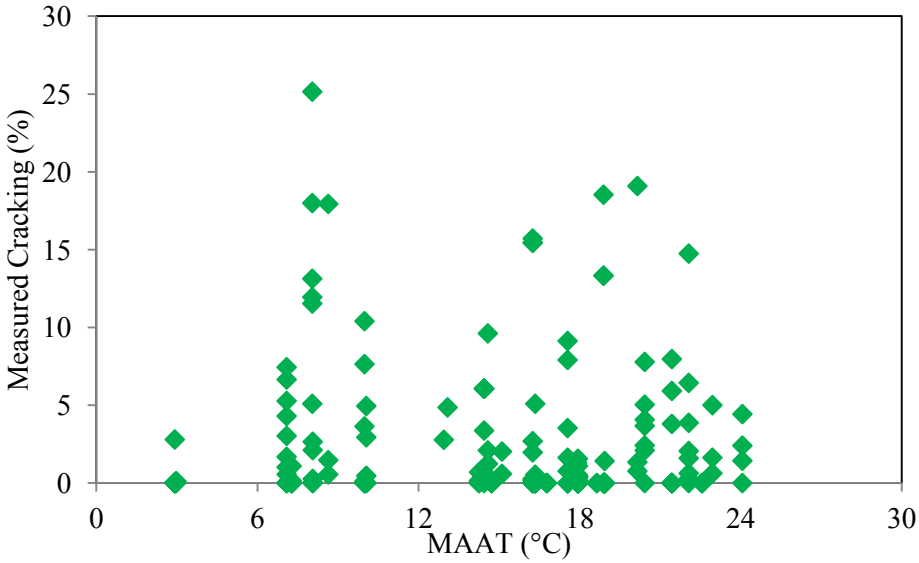

Figure 47. Measured cracking data with the MATT

The LTPP database provided the alligator fatigue–cracking data according to the severity level (low, medium, and high severity) for each LTPP section. The total fatigue cracking without using any weights for each severity category was used as the total alligator cracking data was used while calibrating the AASHTOWare Pavement ME Design Guide. For the bottom-up cracking, the summation of the measured alligator cracking was divided by the total area of the lane (12 ft × 500 ft = 6,000 ft^2) to calculate the percentage area cracked.

6.5 Analysis of Predicted and Measured Cracking Data

The standard errors (predicted cracking-measured cracking) of alligator cracking using both approaches are presented in Fig. 48. Negative value means the measured amount of alligator cracking is greater than the predicted amount of cracking. Fig. 48(a) shows that the error increases with the damage for the traditional AASHTOWare Pavement ME Design approach. It is negligible at the beginning; however, it increases with damage/service life of pavement. The error deviates the maximum value of -24% for the traditional AASHTOWare Pavement ME Design approach which is very unsafe for pavement design. The standard error (S) of estimate of the data is presented using the following best fit equation:

$$S = 1.13 + \frac{13}{1 + e^{7.57 - 15.5 \log D}} \tag{34}$$

In addition, the error continues increasing (positive direction) sharply after certain value of damage which is too much conservative. On the other hand, incorporation of thermal fatigue damage with the traditional AASHTOWare Pavement ME Design produces much consistent error with damage/service life of pavement as shown in Fig. 48(b). This approach produces a standard deviation value of 3.87% of the error and it is almost consistent for all damage values (throughout the service life of pavement). Therefore, considering the thermal fatigue damage, pavement design is way safer compared to the traditional AASHTOWare Pavement ME Design approach. In addition, the standard error using this approach is mostly positive. This means the predicted amount of cracking is greater than the measured amount of cracking; which is conservative. Considering this

positive sign and small value of the standard error, the current study proposes to neglect this error.

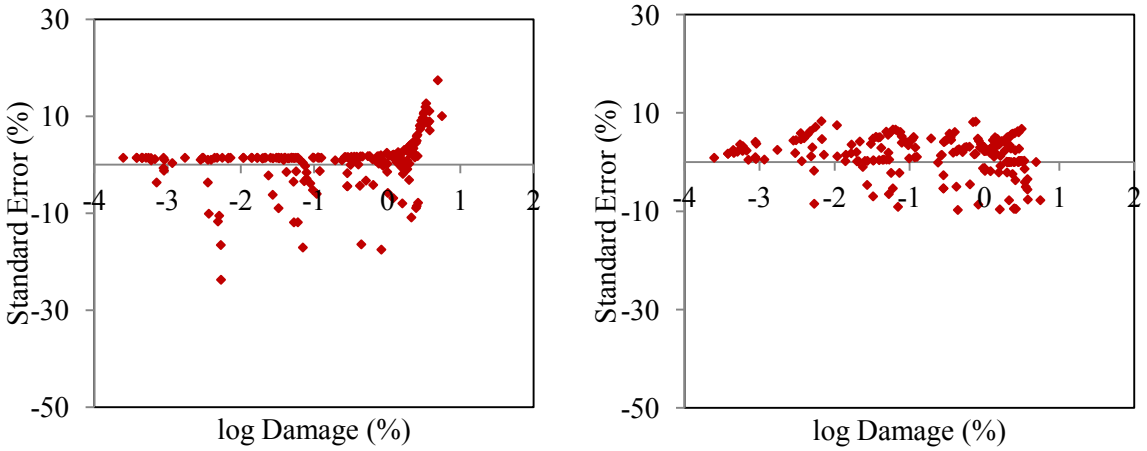

a) Error using traffic loading only (AASHTOWare approach)

b) Error using both traffic- and temperature-induced fatigue

Figure 48. Standard error (prediction minus the measured cracking data)

The predicted cracking data using the AASHTOWare Pavement ME Design approach is presented in Fig. 49. It shows the prediction of alligator cracking using Eq. 14. It can be observed that the predicted cracking is typically below the predicted cracking. The Root Mean Square of Error (RMSE) is 4.812.

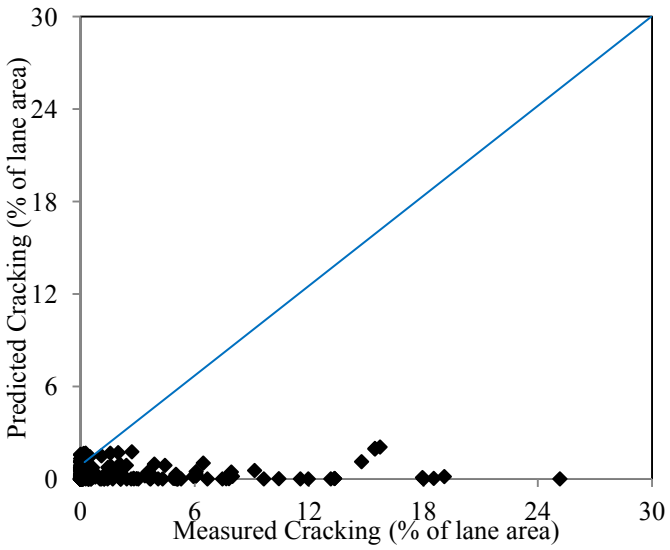

Figure 49. Prediction of alligator cracking versus the measured cracking data

The predicted cracking data combining the temperature-induced fatigue damage with the AASHTOWare Pavement ME Design is presented in Fig. 50. The prediction of the alligator cracking has been calculated using Eqs. (32) and (33). The visual inspection shows that the cracking prediction is less scattered for the prediction of cracking using both the traffic and the temperature as shown in Fig. 50. The RMSE of the alligator cracking predicted by combining the temperature-induced fatigue damage with the AASHTOWare Pavement ME Design is 4.151. This means the RMSE decreases by 14% after the incorporation of temperature-induced fatigue damage with the AASHTOWare Pavement ME Design Software.

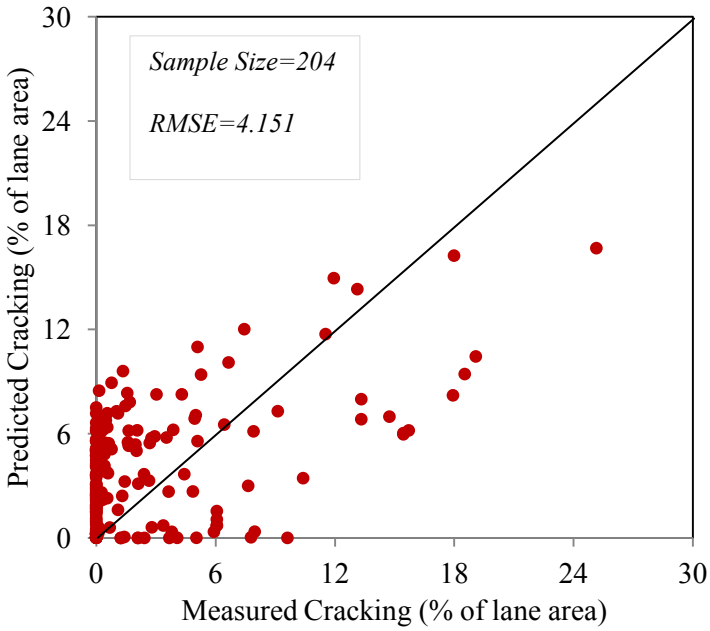

Figure 50. Prediction of alligator cracking versus the LTPP measured data

The above prediction of cracking in Fig. 50 is obtained by using the cracking model shown in Eq. 33. All the coefficients of Eq. 33 were kept unchanged. If the coefficients of Eq. 33 are modified to accommodate the temperature induced fatigue, it may further cause a decrease in the RMSE value. The following revised cracking model is proposed:

$$FC = (\frac{d}{60})\frac{C_4}{1+e^{-2C_2+C_2\log(D\%)}} \tag{35}$$

where $C_2 = -2.40874a - 39.748b(1+h)^{-2.856c}$

Four regression constants have been added as *a*, *b*, *c* and *d*. Correlating the measured cracking data using Eq. 35, in different trials, the regression coefficients (*a*, *b*, *c* and *d*) were obtained. The regression coefficients and the corresponding RMSE are presented in

Table 11. Here, the unity value of the regression coefficient is assumed; the rest of the values are obtained from the best fit simulations. It can be observed that only by introducing the regression constant, *a* (keeping everything else unchanged), the RMSE decreases by 24%. The incorporation of four regression coefficients (*a*, *b*, *c* and *d*) the RMSE decreases by 29%.

Table 11. Optimizing the cracking model (Eq. 35) to minimize the error

Trial No.	*a*	*b*	*c*	*d*	RMSE	Decrease in RMSE (%)
1	1	1	1	1	4.1514	13.7
2	1.23	1	1	1	3.6678	23.8
3	1.148	1.742	1	1	3.6058	25.1
4	1.161	2.332	1.085	1	3.6141	24.9
5	1.858	15.86	1.585	4.172	3.4404	28.5

The prediction of alligator cracking using four regression coefficients (Trial 5 in Table 11) is shown in Fig. 51. It shows that the prediction is much close to the measured data; the RMSE is 3.44. This means the error decreases by 29% after revising the regression constants in cracking model presented in Eq. 35.

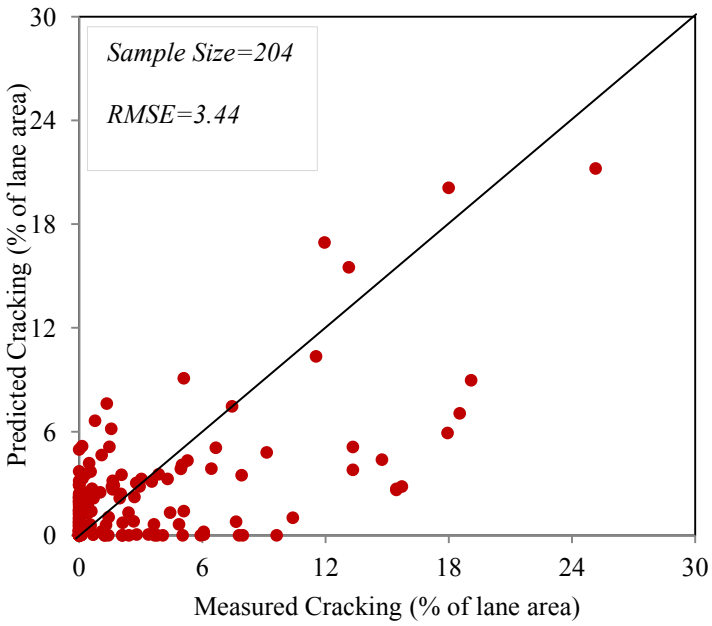

Figure 51. Prediction of cracking using the proposed cracking model (Eq. 35)

CHAPTER SEVEN

CONCLUSIONS AND RECOMMENDATION

7.1 General

Traffic-induced fatigue damage occurs due to tensile strain at the bottom of AC. After certain level of damage accumulation, bottom-up fatigue cracking initiates and forms alligator cracking at the surface. Like traffic loading, repeated day-night temperature cycle may cause some damages due to cyclic thermal expansion and contraction of AC. The recent AASHTOWare Pavement ME Design Software does not consider the cyclic thermal strain due to day-night temperature fluctuation due to the fact that there is no closed-form solution or model available for calculating thermal fatigue damage. This study for the first time, developed a fatigue model to determine the fatigue life of AC due to day-night temperature fluctuation. The model was developed based on laboratory fatigue testing and calibrated to field condition. The developed model was then evaluated for its performance using measured alligator cracking data from 34 LTPP sections.

7.2 Conclusions

Like traffic loading day-night temperature fluctuations cause fatigue damage in AC. A thermal fatigue damage model was developed in this study. The AASHTOWare Pavement ME Design approach can be improved for the better prediction of alligator cracking by considering the developed thermal fatigue damage with the traffic-induced fatigue damage. The thermal fatigue model can enhance the accuracy of the fatigue cracking prediction by any pavement design software. Specific finding from this research are listed below:

- The temperature-induced fatigue model developed in this study is represented by the following:

$$N_{ft} = 1.4423x10^{-8}(\frac{1}{E})^{0.4168}(\frac{1}{\varepsilon})^{3.458} \quad \text{or}$$

$$N_{ft} = 1.4423x10^{-8}(\frac{1}{E})^{0.4168}(\frac{1}{\alpha(\Delta T)})^{3.458} \quad \text{or}$$

$$N_{ft} = 1.272x10^{-6}(\frac{14.696}{E(atm)})^{0.4168}(\frac{1}{\alpha(\Delta T)})^{3.458}$$

where N_{ft} is the allowable day-night temperature cycle, E is the stiffness of AC (psi) at 1.16x10^{-5} Hz; *E(atm)* is the stiffness of AC in atmospheric pressure at 1.16x10^{-5} Hz; ε is the thermal strain due to day-night temperature fluctuation; α is the coefficient of thermal expansion and contraction; and ΔT is the day-night temperature fluctuation in AC.

- If the developed temperature-induced fatigue model in this study is combined with the traffic-induced fatigue model that is available in the AASHTOWare Pavement ME Design Guide, the error in the prediction of alligator cracking decreases by 14%.
- The damage in a single cycle of loading while conducting beam fatigue test using mechanical loading is statistically equal with the damage produced while conducting axial fatigue test using thermal loading.
- The fatigue life of AC decreases with the decrease in frequency of loading; however, becomes stable at the frequency of 0.01 Hz or less.
- CTC and CTE values of asphalt mixture are non-linear with temperature. CTC value is concave downward and CTE value is concave upward. The temperature-

dependent α-value (με/°C) (average of CTC and CTE) can be presented by the following equation:

$$\alpha = -0.006T^2 + 0.356T + 22.633$$

- CTC and CTE values of AC are not affected by the sample's cross-anisotropy, air void and aggregate gradation; however, aggregate type has a significant effect on CTC and CTE values.

7.3 Recommendations for Further Study

This study proposes a closed form equation to calculate the allowable number load repetition for day-night temperature fluctuation. In spite of limited limitations (such as number of mixtures, number of tests, calibration data) this study shows the importance of incorporating the thermal fatigue damage in pavement design. Some future researches can be recommended as follows:

- Only three mixtures were used to develop the thermal fatigue model. The fourth mixture was used to validate the model. In future, wider range of mixtures can be used to improve the developed thermal fatigue model in this study.
- The developed model was calibrated to field conditions using a single pavement on I-40 in New Mexico. Several instrumented pavement sections with different climate conditions can be used to improve the model.
- While calibrating the model in the field, the effects of aging, freeze-thaw, moisture damage, healing etc. were ignored. Further testing on damage behavior of field AC due to environmental factors can be pursued in future studies.

- The samples were clamped with wood while applying actual temperature loading on restrained samples. In future studies, zerodur material can be used instead of wood to examine the full restraining effect on temperature-induced fatigue damage. Also, the thermal fatigue damage can be monitored using the acoustic emission test at different cycles of temperature-conditioned samples in the laboratory.
- The pavement AC slab was considered one-dimensional in this study. Biaxial tension in AC slab was not considered in the current study. Biaxial or three-dimensional analysis can be conducted in a future study.
- The developed model can be used to determine the fatigue damage due to day-night temperature loading which contributes to the longitudinal top-down cracking. It is well known that the longitudinal top-down crack occurs in AC pavement due to both traffic-induced fatigue and temperature-induced fatigue damages. The traffic-induced fatigue model that is available in the AASHTOWare Design Software can be used to determine the traffic related fatigue damage. The AASHTOWare Design Software uses the bottom-up traffic model to determine the top-down fatigue damage of AC. This is because no top-down traffic fatigue model is still available in the literature. The top-down traffic fatigue model can be developed in the laboratory by the axial push-pull fatigue testing. The reason for the axial push-pull fatigue test is that the top-down traffic fatigue damage occurs due to the tensile strain developed close to the vehicle tire. Thus, the axial push-pull fatigue testing can be conducted in tension mode to develop the traffic-induced fatigue model for top-down fatigue model.

REFERENCES

AASHTO (2008). "Mechanistic-Empirical Pavement Design Guide." A Manual of Practice, July 2008, Interim Edition, American Association of State Highway and Transportation Officials, Washington D.C.

AASHTO T 166-07. (2007). "Bulk Specific Gravity of Compacted Hot Mix Asphalt using Saturated Surface-Dry Specimens." *Standard Specifications for Transportation Materials and Methods of Sampling and Testing,* 27th Edition, American Association of State Highway and Transportation Officials, Washington, D.C.

AASHTO T 209-05. (2007). "Theoretical Maximum Specific Gravity and Density of Hot Mix Paving Mixtures." *Standard Specifications for Transportation Materials and Methods of Sampling and Testing,* 27th Edition, American Association of State Highway and Transportation Officials, Washington, D.C.

AASHTO T 312-07. (2007). "Preparing and Determining the Density of Hot-Mix asphalt (HMA) Specimens by Means of the Superpave Gyratory Compactor." *Standard Specifications for Transportation Materials and Methods of Sampling and Testing,* 27th Edition, American Association of State Highway and Transportation Officials, Washington, D.C.

AASHTO T 84-00. (2007). "Specific Gravity and Absorption of Fine Aggregate." *Standard Specifications for Transportation Materials and Methods of Sampling and Testing,* 27th Edition, American Association of State Highway and Transportation Officials, Washington, D.C.

AASHTO T 85-91. (2007). "Specific Gravity and Absorption of Coarse Aggregate." *Standard Specifications for Transportation Materials and Methods of Sampling and Testing,* 27th Edition, American Association of State Highway and Transportation Officials, Washington, D.C.

AASHTO T 321-07. (2007). "Determining the Fatigue Life of Compacted Hot-Mix Asphalt Subjected to Repeated Flexural Bending." *Standard Specifications for Transportation Materials and Methods of Sampling and Testing, 27th Edition*, American Association of State Highway and Transportation Officials, Washington, D.C.

Ahmed, M., Tarefder, R. A., and Islam, M. R. (2013). "Effect of Cross-Anisotropy of Hot-Mix Asphalt Modulus on Falling Weight Deflections and Embedded Sensor Stress-Strain." *Journal of the Transportation Research Record,* Vol. 2369, pp. 20–29.

Ahmed, M., Tarefder, R. A. and Islam, M. R., Rahman, M. (2014). "A Study on Cross-anisotropy of Unbound Layers of Pavement Considering Nonlinearity." *International Journal of Pavement Research and Technology*, Vol. 7, No. 4. pp. 263–272.

Al-Ostaz, A. (2007). "*Effect of Moisture Content on the Coefficient of Thermal Expansion of Concrete*." Report No. FHWA/MS-DOT-RD-07-187 (Final Report), Submitted to the Mississippi Department of Transportation, Jackson, MS, USA.

Al-Qadi, I., Hassan, M. and Elsefi, M. (2005). "Field and Theoretical Evaluation of Thermal Fatigue Cracking in Flexible Pavements," *Journal of the Transportation Research Record*, Vol. 1919, pp. 87–95.

Al-Qadi, I. L., Wang, H. and Tutumluer, E. (2010). "Dynamic Analysis of Thin Asphalt Pavements by Using Cross-Anisotropic Stress-Dependent Properties for Granular Layer." *Journal of the Transportation Research Record*, Vol. 2154, pp. 156–163.

Appea, A. K. (2003). "*Validation of FWD Testing Results at the Virginia Smart Road: Theoretically and by Instrument Response*." PhD dissertation. Virginia Polytechnic Institute and State University, Blacksburg, VA., 2003.

Arabzadeh, A., Karakaya, Y. and Guler, M. (2015). "Thermal Fatigue Behavior of Asphalt Concrete Under Constant Amplitude Strain Loading." *Transportation Research Board Annual Meeting 2015*, Washington, DC. USA, Paper ID: 15–4338.

Bayat, A. and Knight, M., (2010). "Measurement and Analysis of Flexible Pavement Thermal-Induced Strains," *Transportation Research Board Annual Meeting* 2010, Washington, D.C., Paper No. 10–3654.

Carslaw, H. S. and Jaeger, J. C. (1959). *Conduction of Heat in Solids*, 2nd Ed., Oxford University Press, 1959, London.

Carvalho, R. L., and Schwartz, C. (2006). "Comparisons of Flexible Pavement Designs: AASHTO Empirical Versus NCHRP Project 1-37A Mechanistic–Empirical." *Journal of the Transportation Research Record*, Vol. 1947, pp. 167–174.

Diefenderfer, B. (2002). *Moisture Content Determination and Temperature Profile Modeling of Flexible Pavement Structures*, Ph.D. Thesis, Virginia Polytechnic Institute and State University, Virginia.

Domaschuk, L., Skarsgard, P. and Christianson, R. (1964). Cracking of Asphalt Pavement due to Thermal Contraction, *Proc., Canadian Good Roads Association,* pp. 395–402.

El-Basyouny, M. and Witczak, M. (2005a). "Verification of the Calibrated Fatigue Cracking Models for the 2002 Design Guide." *Journal of Association of Asphalt Paving Technologists,* Vol. 74, pp. 653–696.

El-Basyouny, M. and Witczak, M. (2005b). "Calibration of Alligator Fatigue Cracking Model for 2002 Design Guide." *Journal of the Transportation Research Record*, Vol. 1919, pp. 77–86.

Hardin, J. C. (1995). "Physical Properties of Asphalt Cement Binders." *ASTM International, Technology & Engineering,* No. 1241.

Howard, I. L., and Warren, K. A. (2009). "Finite-Element Modeling of Instrumented Flexible Pavements Under Stationary Transient Loading." *Journal of Transportation Engineering*, Vol. 135, No. 2, pp. 53–61.

Huang Y. (2004). *Pavement Analysis and Design*, 2nd Edition, 2004, Pearson Education International, Upper Saddle River, N.J., USA.

Islam, M. R., Rahman, M. T. and Tarefder, R. A. (2012). "Laboratory Investigation of the Stiffness and the Fatigue Life of Glass Grid Reinforced Asphalt Concrete." *International Journal of Pavements*, Vol. 11, No. 1, pp. 82–91.

Islam, M. R., and Tarefder, R. A. (2013a). "Evaluating the Longitudinal and the Transverse Horizontal Strains at the Bottom of Hot Mix Asphalt." *Int. J. Sci. Eng. Res.*, Vol. 4, No. 3, pp. 1–5.

Islam, M. R., and Tarefder, R. A. (2013b). “Measuring Thermal Effect in the Structural Response of Flexible Pavement Based on Field Instrumentation.” *International Journal of Pavement Research and Technology*, Vol. 6, No. 4, pp. 274–279.

Islam, M. R. and Tarefder, R. A. (2014a). “Quantifying Traffic and Temperature Induced Fatigue Damages of Asphalt Pavements.” *Journal of Transportation Infrastructure Geotechnology*, Springer, DOI: 10.1007/s40515-014-0014-3.

Islam, M. R. and Tarefder, R. A. (2014b). “Determining Coefficients of Thermal Contraction and Expansion of Asphalt Concrete Using Horizontal Asphalt Strain Gauge.” *ASTM Journal of Advances in Civil Engineering Materials*, Vol. 3, No. 1, pp. 204–219.

Islam, M. R. and Tarefder, R. A. (2014c). "Tensile Strength of Asphalt Concrete due to Moisture Conditioning." *International Journal of Civil, Architectural, Structural and Construction Engineering,* Vol. 8, No. 9, pp. 942–945.

Islam, M. R. and Tarefder, R. A. (2014d). “Determining Thermal Properties of Asphalt Concrete Using Field Data and Laboratory Testing.” *Construction and Building Materials,* ELSEVIER, Vol. 67, pp. 297–306.

Islam, M. R., Rahman, M. T. and Tarefder, R. A. (2014a). "Evaluating Sample Orientation in Flexural Stiffness and Temperature Load in Fatigue Life of Asphalt Concrete." *Geotechnical Special Publication (ASCE),* Vol. 239, pp. 90–99.

Islam, M. R., Ahmed, M. and Tarefder, R. A. (2014b). “Measuring the Cross-Anisotropy of Hot-Mix Asphalt.” *International Journal of Pavement Engineering,* Taylor and Francis, DOI. 10.1080/10298436.2014.993186.

Islam, M. R., and Tarefder, R. A. (2015a). "Thermal Fatigue Damage of Asphalt Pavement: Model Development and Evaluation." *Transportation Research Board Annual Meeting 2015*, January 11-15, 2015, Washington, D.C., Paper No. 15–5673.

Islam, M. R., and Tarefder, R. A. (2015b). "Coefficients of Thermal Contraction and Expansion of Asphalt Concrete in the Laboratory." *ASCE Journal of Materials in Civil Engineering*. DOI. 10.1061/(ASCE)MT.1943-5533.0001277.

Islam, M. R. and Tarefder, R. A. (2015c). "Effects of Large Freeze-Thaw Cycles on Stiffness and Tensile Strength of Asphalt Concrete." *ASCE Journal of Cold Regions Engineering,* DOI. 10.1061/(ASCE)CR.1943-5495.0000094.

Islam, M. R., and Tarefder, R. A. (2015d). "A Study of Asphalt Aging Through Beam Fatigue Test." *Journal of the Transportation Research Record*, (in press)

Islam M. R., Ahsan, S. and Tarefder, R. A. (2015a). "Modeling Temperature Profile of Hot-Mix Asphalt in Flexible Pavement." *International Journal of Pavement Research and Technology*. Vol. 8, No. 1, pp. 47–52.

Islam, M. R., Ahmad, M. and Tarefder, R. A. (2015b). "Effect of Loading Rate on the Properties of Asphalt Concrete using Three-Point Bending Test." *Advanced Materials Research*, Vol. 1096, pp 553–556.

Islam, M. R., Faisal H. and Tarefder, R. A. (2015d). "Determining Temperature and Time Dependent Poisson's Ratio of Asphalt Concrete Using Indirect Tension Test." *Journal of Fuel*, ELSEVIER, Vol. 146, pp. 119–124.

Jahangirmejad, S., Buch, N., and Kravchenko, A. (2009). "Evaluation of Coefficient of Thermal Expansion Test Protocol and Its Impact on Jointed Concrete Pavement Performance." *ACI Materials Journal*, Vol. 106, No. 1, pp. 64–71.

Jones, M., Darter, I. and Littlefield, G. (1968). Thermal Expansion-Contraction of Asphaltic Concrete, *Proceedings of the Association of Asphalt Paving Technologists,* Vol. 37, pp. 56–100.

Kallas, B. F. (1966). "Asphalt Pavement Temperatures." *Highway Research Record*, Vol. 150, pp. 1–11.

Khadrawi, A., Al-Shyyab, A., and Abo-Qudais, S. (2012). Transient Thermal Behaviour of Hot Mix Asphalt Pavement, *Applied Mechanics and Materials*, Vol. 110-116, pp. 400–407.

Kirkner, D. J. and Shen, W. (1999). "Numerical Simulation of Thermal Cracking of Asphalt Pavements," *Transportation Research Board Preprint*, Washington, D.C.

Littlefield, G. (1967). Thermal Expansion and Contraction Characteristics Utah Asphaltic Concretes, *Proc., of the Association of Asphalt Paving Technologists*, Denver, Colorado, Vol. 36, pp. 673–702.

Long-Term Pavement Performance Program (LTPP). (2015). 6300 Georgetown Pike, HRDI-13, McLean, VA, (www.infopave.com).

Mamlouk, M., Witczak, M., Kaloush, K. and Hasan, N. (2005). "Determination of Thermal Properties of Asphalt Mixtures." *Journal of Testing and Evaluation,* Vol. 33, No. 2, pp. 1–9.

Mannan, U. A., Islam, M. R., and Tarefder, R. A. (2015). "Fatigue Behavior of Asphalt Containing Recycled Asphalt Pavements Under Different Strain Levels and Loading Frequencies." *International Journal of Fatigue,* ELSEVIER (in press)

Marasteanu, M., Li X., Clyne, T., Voller, V., Timm D. and Newcomb, D. (2004). "Low Temperature Cracking of Asphalt Concrete Pavements." MN/RC – 2004-23, Final Report 1999-2004, Minnesota Department of Transportation, St. Paul, Minnesota.

Metha, Y., Stoffels, A. and Christensen, W. (1999). "Determination of Thermal Contraction of Asphalt Concrete Using IDT Hardware." *Journal of Association of Asphalt Paving Technologists,* Vol. 68, pp. 349–369.

Naik, T., Kraus, R. and Kumar R. (2011). "Influence of Types of Coarse Aggregates on the Coefficient of Thermal Expansion of Concrete." *Journal of Materials in Civil Engineering,* Vol. 23, No. 4, pp. 467–472.

NCHRP. (2004). "*Guide for Mechanistic–Empirical Design of New and Rehabilitated Pavement Structures*." Final report, 1-37A. Transportation Research Board of the National Academies, Washington, D.C.,

Prowell, B., Brown, E. R., Daniel, J., Bhattacharjee, S., Von Quintus, H., Carpenter, S. H., Shen, S., Anderson, M., Swamy, A. K. and Maghsoodloo, S. (2008). "*Endurance Limit of Hot Mix Asphalt Mixtures to Prevent Fatigue Cracking in Flexible Pavements*." Final Report, NCHRP 9-38, National Cooperative Highway Research Program, Washington, D.C.

Rajbonshi, P. and Das, A. (2009). "Estimation of Temperature Stress and Low-Temperature Crack Spacing in Asphalt Pavements." *Journal of Transportation Engineering,* Vol. 135, No. 10, pp. 745–752.

Schwartz, C., Li, R., Ceylan, H., Kim, S. and Gopalakrishnan, K. (2013). "Global Sensitivity Analysis of Mechanistic–Empirical Performance Predictions for Flexible Pavements." *Journal of the Transportation Research Record*, Vol. 2368, pp. 12–23.

Shahin, M. and McCullough, B. (1974). "Damage Model for Predicting Temperature Cracking in Flexible Pavements." *Journal of the Transportation Research Record*, Vol. 521, pp. 30–46.

Stoffels, S. and Kwanda, F. (1996). "Determination of the Co-efficient of Thermal Contraction of Asphalt Concrete Using the Resistance Strain Gauge Technique." *Journal of Association of Asphalt Paving Technologists,* Vol. 65, pp. 73–93.

Tarefder, R. A. and Barlas, G. (2013). "*Determining Fatigue Endurance Limits of New Mexico Asphalt Mixes for Designing Perpetual Pavements and Implementation of MEPDG to Its Full Capacity*." Final Report, NM11MSC-02, 2013, New Mexico Department of Transportation, Albuquerque, NM.

Tarefder, R. A. and Islam, M. R. (2013). "Measuring Fatigue Damage From an Instrumented Pavement Section due to Day-Night and Yearly Temperature Rise and Fall in Desert Land of the West." *Climatic Effects on Pavement and Geotechnical Infrastructure, ASCE,* pp. 78–88.

Tarefder, R. A., Ahmed, M. U. and Islam, M. R. (2013). "Impact of Cross-Anisotropy on Embedded Sensor Stress–Strain and Pavement Damage." *European Journal of Environmental and Civil Engineering*, Taylor and Francis, Vol. 18, No. 8, pp. 845–861

Tarefder, R. A., Ahmed, M., Islam, M. R. and Rahman, M. (2014). "Finite Element Model of Pavement Response under Load Considering Cross-Anisotropy in Unbound Layers." *ASTM Journal of Advances in Civil Engineering Materials,* Vol. 3, No. 1, pp. 57–75.

Timm, D., Guzin B. and Voller, V. (2003). "Prediction of Thermal Crack Spacing." *International Journal of Solids and Structures*, 40 (2003) 125–142

Timm, D., Turochy, R. and Davis, K. (2010). "*Guideline for M-E Pavement Design Implementation.*" Final Report (Project No. 930-685), Submitted to Alabama Department of Transportation (ALDOT), Auburn, AL, USA.

Wang, D. (2012). Analytical Approach to Predict Temperature Profile in a Multilayered Pavement System Based on Measured Surface Temperature Data, *Journal of Transportation Engineering,* Vol. 138, No. 5, pp. 674–679.

Won, M. (2005). "Improvements of Testing Procedures for Concrete Coefficient of Thermal Expansion." *Journal of the Transportation Research Record,* Vol. 1919, pp. 23–28.

Xu, Q. and Solaimanian, M. (2008). "Measurement and Evaluation of Asphalt Concrete Thermal Expansion and Contraction." *Journal of Testing and Evaluation,* Vol. 36, No. 2, pp. 140–149.

Yavuzturk, C., and Ksaibati, K. (2002). *Assessment of Temperature Fluctuations in Asphalt Pavements due to Thermal Environmental Conditions Using a Two-Dimensional, Transient Finite Difference Approach*, Report submitted to United States Department of Transportation, Laramie, WY.

Zeng, M. and Shields, D. (1999). "Nonlinear Thermal Expansion and Contraction of Asphalt Concrete." *Canadian Journal of Civil Engineering,* Vol. 26, No. 1, pp. 26–34.

Zubeck, H. and Vinson, T. (1996). "Prediction of Low-Temperature Cracking of Asphalt Concrete Mixtures with Thermal Stress Restrained Specimen Test Results." *Journal of Transportation Research Record*, Vol. 1545, pp. 50–58.

APPENDIX A

SAMPLE CALCULATION FOR DETERMINING ALLIGATOR CRACKING INCLUDING THERMAL FATIGUE DAMAGE

An example is presented here to show how thermal-fatigue damage has been calculated. In addition, it shows how alligator cracking was determined including the temperature-induced fatigue damage. A LTPP pavement section from Arizona, 04-0113, has been chosen randomly. The measured cracking on this section was obtained from the LTPP database. The predicted alligator cracking using the AASHTOWare Pavement ME Design Software was determined first. Then, the alligator cracking using the thermal fatigue damage with the AASHTOWare Pavement ME Design Guide was calculated.

Description of the Section

The general information of the Section is provided in Table A1. It is located in Arizona with latitude of 35.392° and longitudinal of 114.255°. The construction of the pavement started in June 1993; the design life was 6 years. It had three layers: AC layer of 4.5 in. thickness, granular base of 7.5 in. thickness and then semi-infinity subgrade. The climate of the test section can be generated using the AASHTOWare Pavement ME Design Software using interpolation of several weather stations nearby. It needs the latitude, longitude, elevation and ground water table as the inputs to extract the nearby weather station data.

Table A1. General information of the 04-0113 section

Location	AZ
LTPP ID	04-0113
Design Life	6 years
Base/Subgrade construction:	June, 1993
Pavement construction:	August, 1993
Traffic open:	August, 1993
Type of design	Flexible
Latitude North (degrees)	35.392
Longitude West (degrees	114.255
Elevation (ft)	3580
Groundwater Table Depth1 (ft)	>20
Layers	AC: 4.5 in Base Layer: 7.5 in
Unbound Layers' Stiffnesses	Base Layer: 40000 psi Subgrade: 38000 psi

Measured Alligator Cracking Data

The measured alligator cracking data obtained from the LTPP database is presented in Table A2. The survey was started in February 1995. The survey report presented the measured amount of cracking in ft^2. Then, the percentage of lane area cracked was calculated considering the total lane area of 6000 ft^2 (500 ft section with 12 ft wide lane). The cumulative percentage lane area cracked was calculated with the survey period.

Table A2. Measured alligator cracking data from the LTPP

Survey Date	Measured Cracking (ft^2)	Percentage of total Lane Area
2/21/1995	0	0
3/30/1995	0	0
8/17/1995	0	0
11/8/1995	0	0
2/7/1996	0	0
4/3/1996	0	0
7/10/1996	0	0
8/14/1996	0	0
1/8/1998	0	0
1/13/1998	0	0
4/20/1998	9.700	0.1617
6/11/1998	9.700	0.3233
10/22/1998	9.700	0.4850
2/16/1999	36.600	1.0950
1/13/2000	28.000	1.5617

AASHTOWare Predicted Alligator Cracking Data

The AASHTOWare Pavement ME Design Software has been used to predict the alligator cracking of the section. The inputs of the section were obtained from the LTPP database. Typically, the software needs three types of inputs:

a) General inputs (Geometry of the section, design criteria etc.)

b) Climate (Temperature and moisture data)

c) Traffic (Axle weight and distribution)

The general inputs of the section are listed in Table A1. The climate data was obtained by interpolation of the several weather stations data nearby. The traffic data was been extracted from the LTPP database. The design two-way (total of 4 lanes) Annual Average

Daily Truck Traffic (AADTT) was 600 with a compound growth rate of 4%. The monthly adjustment factors of the traffic are presented in Table A3.

Table A3. Monthly traffic adjustment factor on the section of 04-0113

Month	Vehicle Class									
	Class 4	Class 5	Class 6	Class 7	Class 8	Class 9	Class 10	Class 11	Class 12	Class 13
January	0.58	0.80	1.23	0.00	0.79	0.97	1.21	0.76	0.95	0.00
February	0.52	0.79	0.77	0.00	0.88	0.93	1.38	0.75	0.84	0.00
March	0.58	0.99	1.02	0.00	1.24	0.92	1.05	2.18	0.95	0.00
April	0.93	1.12	1.08	0.00	1.29	1.05	1.38	1.52	1.16	0.00
May	1.05	1.05	1.03	0.00	1.13	0.97	0.70	0.84	1.16	0.00
June	1.40	1.25	1.33	0.00	1.13	1.13	1.05	0.93	1.05	0.00
July	1.39	1.19	1.02	0.00	0.98	0.92	0.70	0.73	1.05	0.00
August	1.40	1.16	1.00	0.00	0.93	0.99	0.70	0.80	0.84	0.00
September	1.28	1.07	1.28	0.00	0.95	0.97	1.04	0.84	1.05	0.00
October	1.28	1.01	0.89	0.00	1.05	1.03	1.04	0.91	0.95	0.00
November	0.81	0.81	0.71	0.00	0.87	1.08	0.70	0.86	1.05	0.00
December	0.81	0.75	0.63	0.00	0.73	1.03	1.05	0.89	0.95	0.00

The vehicle class distribution is shown in Table A4. It shows that most of the traffic is class 9 vehicle with the percentage of 61.2%. The AASHTOWare Pavement ME default values have been used for which site specific data is not available in the LTPP.

Table A4. Vehicle class distribution

Class	Weightage
Class 4	1.4%
Class 5	17.4%
Class 6	2.9%
Class 7	0.0%
Class 8	8.4%
Class 9	61.2%
Class 10	0.4%
Class 11	6.8%
Class 12	1.5%
Class 13	0.0%

After the simulation, the damage ratio and percentage of the total lane area cracked were obtained with the service life. The values on the survey dates are presented in Table A5.

Table A5. Predicted alligator cracking data from the AASHTOWare output

Date	Damage Ratio (%)	Percentage of total Lane Area
2/21/1995	0.735	1.75
3/30/1995	0.765	1.77
8/17/1995	1.05	1.92
11/8/1995	1.18	2.00
2/7/1996	1.23	2.04
4/3/1996	1.31	2.10
7/10/1996	1.51	2.29
8/14/1996	1.58	2.38
1/8/1998	2.29	4.60
1/13/1998	2.29	4.60
4/20/1998	2.38	5.16
6/11/1998	2.53	6.25
10/22/1998	2.79	8.56
2/16/1999	2.87	9.35
1/13/2000	3.15	12.09

Prediction of Alligator Cracking including Thermal Fatigue Damage with the AASHTOWare

The procedure to determine the alligator cracking incorporating the thermal fatigue damage with the AASHTOWare Pavement ME Design can be described as follows:

Step 1: Take the average temperatures at the different periods (say, months) of analysis (Column 2 of Table A6).

Step 2: Calculate the α-values at the different periods of analysis using Eq. 16 (Column 3 of Table A6).

Step 3: Predict the maximum temperature (y_{max}) (Eq. 18) and the minimum temperature (y_{min}) (Eq. 20) at the bottom of AC using the surface maximum and the minimum temperatures obtained from the AASHTOWare Pavement ME Design output. Then, the average temperature fluctuation for that period can be determined by $\Delta T = y_{\max} - y_{\min}$ (Column 6 of Table A6).

Step 4: Determine the developed thermal strain, $\varepsilon = \alpha \Delta T$ (Column 7 of Table A6).

Step 5: Take the stiffness of AC from the AASHTOWare Pavement ME Design output. It is ideal to determine the stiffness for 1.16×10^{-6} Hz (Column 8 of Table A6).

Step 6: Predict the allowable number of load repletion for temperature fluctuations for a specific period using the developed model ($N_{ft} = 1.4423 x 10^{-8} (\frac{1}{E})^{0.4168} (\frac{1}{\varepsilon})^{3.458}$) (Column 9 of Table A6).

Table A6. Determining allowable load repetition under thermal fatigue

	Average Temp. Below AC	α	Surface Min. Temp	Surface Max. Temp	Temp Fluctuations (ΔT)	Strain ε	E	N
	°C	με/°C	°F	°F	°C	με	ksi	
Jan.	10.29	26	33.4	68.8	10.8	276	177	190
Feb.	11.11	26	35.6	73.2	11.7	301	156	148
Mar.	15.72	27	40.5	86.9	15.6	416	98	59
Apr.	20.33	27	47.1	96.5	16.5	453	58	55
May.	27.67	28	57.6	109	16.7	467	46	54
Jun.	32.50	28	67	116.7	15.2	425	39	80
July.	34.61	28	71.7	119.9	14.2	394	37	107
Aug.	34.22	28	73.7	118.3	12.3	342	39	171
Sep.	29.06	28	64.2	110.4	13.8	384	47	106
Oct.	20.94	27	50.3	96.1	14.6	400	72	77
Nov.	13.22	26	38.8	78.6	12.5	328	178	104
Dec.	7.83	25	31.5	65.6	10.3	257	197	232

Step 7: Determine the damage ratio ($D_2 = \sum_{i=1}^{q} \frac{n_i}{N_{ft,i}}$) for thermal fatigue damage (Column 2 of Table A7).

Step 8: Apply the damage shift factor from Table A2. This is because, it is applied by the AASHTOWare Pavement ME Design in the traffic related fatigue damage Then, calculate the cumulative damage (Columns 3-5 of Table A7).

Step 9: Determine the total damage index ($D = D_1 + D_2$) (Column 4 of Table A8).

Step 10: Determine the amount of alligator cracking ($FC = (\frac{1}{60}) \frac{C_4}{1 + e^{-2C_2 + C_2 \log(D\%)}}$) (Column 5 of Table A8). This value can be modified to increase the reliability.

Table A7. Determining damage under thermal fatigue loading

	Raw Damage Ratio (%)	Shift Factor	Shifted Damage Ratio (%)	Cum. Damage Ratio (%)
2/21/1995	538	0.004	2.2	2.3
3/30/1995	575	0.004	2.3	2.5
8/17/1995	715	0.004	2.9	3.1
11/8/1995	798	0.004	3.2	3.4
2/7/1996	889	0.004	3.6	3.8
4/3/1996	945	0.004	3.8	4.0
7/10/1996	1043	0.004	4.2	4.5
8/14/1996	1078	0.004	4.3	4.6
1/8/1998	1590	0.004	6.4	6.8
1/13/1998	1595	0.004	6.4	6.8
4/20/1998	13.22	0.004	6.8	7.2
6/11/1998	7.83	0.004	7.0	7.5

Table A8. Determining the alligator cracking using the thermal fatigue

Date	Damage Ratio (%) (Traffic)	Damage Ratio (%) (Thermal)	$D = D_1 + D_2$	Predicted Percentage of total Lane Area
2/21/1995	0.735	2.2996	3.0346	1.5988
3/30/1995	0.765	2.4577	3.2227	1.7143
8/17/1995	1.05	3.0561	4.1061	2.2680
11/8/1995	1.18	3.4109	4.5909	2.5787
2/7/1996	1.23	3.7998	5.0298	2.8633
4/3/1996	1.31	4.0392	5.3492	3.0722
7/10/1996	1.51	4.4581	5.9681	3.4806
8/14/1996	1.58	4.6077	6.1877	3.6266
1/8/1998	2.29	6.7961	9.0861	5.5878
1/13/1998	2.29	6.8175	9.1075	5.6024
4/20/1998	2.38	7.2321	9.6121	5.9482
6/11/1998	2.53	7.4543	9.9843	6.2038
10/22/1998	2.79	8.0228	10.8128	6.7736
2/16/1999	2.87	8.5229	11.3929	7.1730
1/13/2000	3.15	9.9377	13.0877	8.3406

APPENDIX B

LTPP DATA FOR CHOSEN PAVEMENT SECTION

The AASHTOWare Pavement ME Design input data for the 34 chosen LTPP sections were collected from the LTPP database. These input data are listed in Table B1 to B10.

Table B1. Analysis conditions

Section	State Code	SHRP ID	State	Project Type	Base/Subgrade Construction Completion Date	Asphalt Construction Completion Date	Traffic Opening Date	Design Period (years
01-1001	01	1001	Alabama	GPS	8/1/1980	10/1/1980	10/1/1980	19
01-1019	01	1019	Alabama	GPS	8/1/1986	10/1/1986	10/1/1986	13
01-4126	01	4126	Alabama	GPS	2/1/1988	4/1/1988	4/1/1988	11
02-1001	02	1001	Alaska	GPS	5/1/1983	7/1/1983	7/1/1983	16
02-1002	02	1002	Alaska	GPS	8/1/1984	10/1/1984	10/1/1984	15
04-0113	04	0113	Arizona	GPS	6/1/1993	8/1/1993	8/1/1993	6
04-0114	04	0114	Arizona	GPS	6/1/1993	8/1/1993	8/1/1993	6
04-1024	04	1024	Arizona	GPS	5/1/1977	7/1/1977	7/1/1977	22
09-1803	09	1083	Connecticut	GPS	5/1/1985	7/1/1985	7/1/1985	14
12-3995	12	3995	Florida	GPS	10/1/1975	12/1/1975	12/1/1975	24
12-3997	12	3997	Florida	GPS	4/1/1974	6/1/1974	6/1/1974	25
12-4107	12	4107	Florida	GPS	4/1/1986	6/1/1986	6/1/1986	13
20-1009	20	1009	Kansas	GPS	11/1/1984	1/1/1985	1/1/1985	14
25-1003	25	1003	Massachusetts	GPS	7/1/1974	9/1/1974	9/1/1974	25
26-1001	26	1001	Michigan	GPS	7/1/1971	9/1/1971	9/1/1971	28
27-1087	27	1087	Minnesota	GPS	11/1/1978	1/1/1979	1/1/1979	20
29-1008	29	1008	Missouri	GPS	2/1/1986	4/1/1986	5/1/1986	13
34-1031	34	1031	New Jersey	GPS	7/1/1973	9/1/1973	9/1/1973	26
35-0101	35	0101	New Mexico	GPS	9/1/1995	11/1/1995	11/1/1995	4
35-1112	35	1112	New Mexico	GPS	4/1/1984	6/1/1984	6/1/1984	15
37-1024	37	1024	NC	GPS	9/1/1980	11/1/1980	11/1/1980	19
37-1802	37	1802	NC	GPS	12/1/1989	2/1/1990	2/1/1990	9
40-4087	40	4087	Oklahoma	GPS	2/1/1986	4/1/1986	7/1/1986	13
40-4165	40	4165	Oklahoma	GPS	4/1/1984	6/1/1984	6/1/1984	15
42-1599	42	1599	Pennsylvania	GPS	6/1/1987	8/1/1987	8/1/1987	12
45-1011	45	1011	SC	GPS	4/1/1985	6/1/1985	7/1/1985	13
47-3104	47	3104	Tennessee	GPS	4/1/1986	6/1/1986	6/1/1986	13
48-1077	48	1077	Texas	GPS	11/1/1981	1/1/1982	1/1/1982	17
48-1169	48	1169	Texas	GPS	6/1/1972	8/1/1972	8/1/1972	27
48-1174	48	1174	Texas	GPS	10/1/1973	12/1/1973	5/1/1975	24
48-3749	48	3749	Texas	GPS	1/1/1981	3/1/1981	3/1/1981	18
48-9005	48	9005	Texas	GPS	5/1/1986	7/1/1986	9/1/1986	13
50-1002	50	1002	Vermont	GPS	6/1/1984	8/1/1984	11/1/1984	15
53-1008	53	1008	Washington	GPS	9/1/1978	11/1/1978	11/1/1978	21

Table B2. Pavement lane properties

Section	Lane Width (ft)	Pavement Slope (%)	Initial IRI (m/km)1	Thermal Conductivity (BTU/hr-ft-ºF)	Heat Capacity (BTU/lb-ºF)	Surface Short Wave Absorptivity
01-1001	12	1.5	150	0.67	0.22	0.85
01-1019	12	1.5	150	0.67	0.22	0.85
01-4126	12	1.5	150	0.67	0.22	0.85
02-1001	12	1.5	150	0.67	0.22	0.85
02-1002	12	1.5	150	0.67	0.22	0.85
04-0113	12	1.5	150	0.67	0.22	0.85
04-0114	12	1.5	150	0.67	0.22	0.85
04-1024	12	1.5	150	0.67	0.22	0.85
09-1803	12	1.5	150	0.67	0.22	0.85
12-3995	12	1.5	150	0.67	0.22	0.85
12-3997	12	1.5	150	0.67	0.22	0.85
12-4107	12	1.5	150	0.67	0.22	0.85
20-1009	12	1.5	150	0.67	0.22	0.85
25-1003	12	1.5	150	0.67	0.22	0.85
26-1001	12	1.5	150	0.67	0.22	0.85
27-1087	12	1.5	150	0.67	0.22	0.85
29-1008	12	1.5	150	0.67	0.22	0.85
34-1031	12	1.5	150	0.67	0.22	0.85
35-0101	12	1.5	150	0.67	0.22	0.85
35-1112	12	1.5	150	0.67	0.22	0.85
37-1024	12	1.5	150	0.67	0.22	0.85
37-1802	12	1.5	150	0.67	0.22	0.85
40-4087	12	1.5	150	0.67	0.22	0.85
40-4165	12	1.5	150	0.67	0.22	0.85
42-1599	12	1.5	150	0.67	0.22	0.85
45-1011	12	1.5	150	0.67	0.22	0.85
47-3104	12	1.5	150	0.67	0.22	0.85
48-1077	12	1.5	150	0.67	0.22	0.85
48-1169	12	1.5	150	0.67	0.22	0.85
48-1174	12	1.5	150	0.67	0.22	0.85
48-3749	12	1.5	150	0.67	0.22	0.85
48-9005	12	1.5	150	0.67	0.22	0.85
50-1002	12	1.5	150	0.67	0.22	0.85
53-1008	12	1.5	150	0.67	0.22	0.85

Table B3. Environmental / climatic properties

Section	Latitude North (degrees)	Longitude West (degrees	Elevation (ft)	Groundwater Table Depth (ft)	Source of Information
01-1001	32.533	85.080	495	31	NCHRP (2004)
01-1019	31.353	88.032	61	12	
01-4126	34.179	86.875	760	30	
02-1001	60.650	149.492	1310	>20	
02-1002	60.759	149.239	839	10	
04-0113	35.392	114.255	3580	>20	
04-0114	35.392	114.255	3580	>20	
04-1024	35.279	113.131	5456	>20	
09-1803	41.395	72.027	165	5.9	
12-3995	26.501	80.078	19	9	
12-3997	30.087	81.706	21	10	
12-4107	27.393	80.459	26	16.8	
20-1009	37.998	98.747	1922	15.0	
25-1003	42.201	71.335	128	11	
26-1001	44.31	84.916	1154	19	
27-1087	44.807	93.228	1118	7.8	
29-1008	37.296	94.579	860	34	
34-1031	39.544	75.062	85	5	
35-0101	32.678	107.071	5117	>20	
35-1112	32.632	103.520	3760	>20	
37-1024	35.296	83.18	2125	>20	
37-1802	36.316	78.516	500	>20	
40-4087	34.638	99.288	1350	7.5	
40-4165	36.391	98.291	1319	8.7	
42-1599	41.433	76.713	1500	20	
45-1011	32.822	80.03	12	19	
47-3104	36.24	83.762	1230	>20	
48-1077	34.539	100.435	1835	10.9	
48-1169	32.196	94.803	430	8.0	
48-1174	27.789	97.873	109	>8.3	
48-3749	27.930	98.556	570	20.0	
48-9005	29.517	98.721	910	>20	
50-1002	44.120	73.180	283	4.2	
53-1008	47.558	117.394	2356	55	

Table B4. Pavement structure

Section	No. of Layers	Layer Number	Layer Type1	Representative Thickness (in)
01-1001	5	1	AC	1.6
		2	AC	1.6
		3	GB	6.2
		4	GS	19.1
		5	SS	-
01-1019	6	1	AC	1.1
		2	AC	2.6
		3	AC	3
		4	GB	5.5
		5	SS	252
		6	BR	-
01-4126	5	1	AC	1.4
		2	AC	11.7
		3	GB	18.4
		4	SS	132
		5	BR	-
02-1001	3	1	AC	3
		2	GB	6.3
		3	SS	-
02-1002	4	1	AC	3.3
		2	GB	6
		3	GS	7.5
		4	SS	-
04-0113	3	1	AC	4.5
		2	GB	7.5
		3	SS	
04-0114	3	1	AC	6.8
		2	GB	12
		3	SS	
04-1024	3	1	AC	10.8
		2	GB	6.3
		3	SS	
09-1803	4	1	AC	2.9
		2	AC	4.3
		3	GB	12
		4	SS	-
12-3995	4	1	AC	5
		2	GB	12.8
		3	GS	12
		4	SS	-
12-3997	4	1	AC	3.1
		2	GB	11.6
		3	GS	15
		4	SS	-
12-4107	3	1	AC	2.7
		2	GB	12
		3	SS	-
20-1009	3	1	AC	2.4
		2	AC	8.7
		3	SS	
25-1003	5	1	AC	1.2
		2	AC	5.4
		3	GB	12.7
		4	SS	41
		5	BR	-

Table B4. Pavement structure (contd.)

26-1001	3	1 2 3	AC GB SS	2.2 10.9 -
27-1087	2	1 2	AC SS	15.7 -
29-1008	4	1 2 3 4	AC AC GB SS	1.8 9.6 4.4 -
34-1031	4	1 2 3 4	AC AC GB SS	1.8 5.5 11 -
35-0101	3	1 2 3	AC GB SS	7.2 8.6 -
35-1112	3	1 2 3	AC GB SS	6.3 5 -
37-1024	3	1 2 3	AC GB SS	4.8 12 -
37-1802	4	1 2 3 4	AC AC GB SS	2.2 2.3 8.2 -
40-4087	4	1 2 3 4	AC ATB TS SS	2.2 7.9 6
40-4165	3	1 2 3	AC AC SS	2.7 5.4
42-1599	5	1 2 3 4 5	AC AC GB SS BR	3 9.3 12 300 -
45-1011	3	1 2 3	AC GB SS	3.2 10.1 -
47-3104	4	1 2 3 4	AC GB SS BR	1.3 8.7 300 -
48-1077	4	1 2 3 4	AC AC GB SS	1.4 3.7 10.4
48-1169	4	1 2 3 4	AC GB SS BR	1.1 11.3 240
48-1174	4	1 2 3 4	AC AC GB SS	1.4 3.3 13.2

Table B4. Pavement structure (contd.)

48-3749	4	1 2 3 4	AC GB TS SS	1.8 8.1 8.8
48-9005	4	1 2 3 4	AC GB SS BR	1.15 9.4 300
50-1002	4	1 2 3 4	AC AC GB SS	3 5.5 25.8 -
53-1008	4	1 2 3 4	AC GB GS SS	3.4 3.1 9.8 -

AC: Asphalt Concrete
ATB: Asphalt Treated Base
GB: Granular Base
SS: Subgrade
BR: Bedrock

Table B5. Aggregate gradation for asphalt mixtures

Section	Layer Number	Layer Type1	% Retained 3/4" Sieve	% Retained 3/8" Sieve	%Retained #4 Sieve	% Passing #200 Sieve
01-1001	1	AC	8	33	52	0.1
	2	AC	5	35	54	7.8
01-1019	1	AC	0	12	36	4
	2	AC	7	30	57.5	4
	3	AC	11.5	35	52.5	2.7
01-4126	1	AC	0	21	43	5.8
	2	AC	14	43.5	53	5.2
02-1001	1	AC	0.5	28	51	9.3
02-1002	1	AC	4	28.5	49.5	8.2
04-0113	1	AC	1.8	21.5	39.8	6.3
04-0114	1	AC	1.8	21.5	39.8	6.3
04-1024	1	AC	5.0	33.0	54.0	7.1
09-1803	1	AC	0	33	48	4.8
	2	AC	21.5	45.5	56.5	5.4
12-3995	1	AC	0	7.5	39	4.8
12-3997	1	AC	0	7.5	35	4.1
12-4107	1	AC	0	8	34	4.8
20-1009	1	AC	0.0	16.5	34.5	8.0
	2	AC	0.0	15.5	34.0	7.5
25-1003	1	AC	0	16	44.5	5.7
	2	AC	4	43.5	59.5	3.1
26-1001	1	AC	0	22	43.5	6.9
27-1087	1	AC	7.5	26	39.5	6.7
29-1008	1	AC	0	10	46	6.2
	2	AC	4	31.5	54	9.6
34-1031	1	AC	0	3.5	37	4.2
	2	AC	11	43.5	56.5	5.2
35-0101	1	AC	2	23	43	5.5
35-1112	1	AC	0	20	36.5	7.8
37-1024	1	AC	5.5	38.5	53	5.2
37-1802	1	AC	0	3	20	7.5
	2	AC	5	34	49	5
40-4087	1	AC	0.0	15.0	34.0	7.3
	2	ATB	12.0	29.5	38.5	7.8
40-4165	1	AC	0.0	5.9	27.5	7.2
	2	AC	9.5	57.0	52.0	5.4
42-1599	1	AC	0	1.5	37.5	6.6
	2	AC	22	51	77	4.5
45-1011	1	AC	1	36.5	57	6.7
47-3104	1	AC	0	22	35	9.2
48-1077	1	AC	0.0	3.0	46.0	4.0
	2	AC	22.0	32.0	43.0	7.0
48-1169	1	AC	0.0	0.0	38.0	4.0
48-1174	1	AC	0.0	21.9	38.6	3.0
	2	AC	17.5	31.5	45.5	7.5
48-3749	1	AC	0.0	2.5	32.0	5.1
48-9005	1	AC	0.0	7.0	34.0	4.0
50-1002	1	AC	0.5	21	41.5	3.7
	2	AC	25.5	47.5	63.5	2.9
53-1008	1	AC	0	14	39	6.9

Table B6 Effective binder content

Section	Layer Number	Layer Type1	P_b (%)	G_b	G_{mb}	G_{mm}	G_{sb}	G_{se}	V_{be} (%)
01-1001	1	AC	6.2	1.028	2.365	2.45	2.682	2.697	13.82
	2	AC	4.5	1.028	2.36	2.523	2.67	2.709	9.13
01-1019	1	AC	5.8	1.028	-	-	2.59	-	11.6
	2	AC	4	1.028	2.281	2.493	-	2.65	8.0
	3	AC	3.85	1.028	2.191	2.554	2.95	2.598	7.94
01-4126	1	AC	5.3	1.033	2.196	2.327	2.634	2.502	15.42
	2	AC	3.4	1.033	2.345	2.523	2.666	2.658	7.98
02-1001	1	AC	6.5	1.014	2.238	2.436	2.63	2.682	12.03
02-1002	1	AC	6.35	1.014	2.396	2.461	2.722	2.724	14.94
04-0113	1	AC	4.25	1.040	2.288	2.520	2.653	2.690	8.21
04-0114	1	AC	4025	1.040	2.218	2.520	2.653	2.690	7.96
04-1024	1	AC	4.20	1.012	2.304	2.589	2.704	2.778	7.38
09-1803	1	AC	4.95	1.01	2.297	2.552	-	2.772	9.9
	2	AC	3.55	1.01	2.3	2.527	-	2.675	7.1
12-3995	1	AC	5.6	1.03	2.214	2.371	2.489	2.569	9.43
12-3997	1	AC	6.8	1.03	2.071	2.305	2.44	2.533	10.76
12-4107	1	AC	6.6	1.03	2.226	2.305	2.426	2.525	10.89
20-1009	1	AC	4.50	1.018	2.328	2.430	2.600	2.599	10.31
	2	AC	4.55	1.018	2.298	2.428	2.600	2.600	10.28
25-1003	1	AC	6	1.026	2.544	2.585	2.85	2.862	14.52
	2	AC	4.4	1.026	2.513	2.645	2.85	2.852	10.71
26-1001	1	AC	5.1	1.024	2.391	2.447	2.69	2.644	13.38
27-1087	1	AC	4.65	1.02	2.369	2.531	2.77	2.727	12.07
29-1008	1	AC	4.15	1.017	2.449	2.484	2.635	2.649	9.51
	2	AC	4.2	1.017	2.385	2.477	2.635	2.643	9.59
34-1031	1	AC	5	1.025	2.452	2.57	2.785	2.791	11.79
	2	AC	4.15	1.025	2.507	2.566	2.852	2.745	13.45
35-0101	1	AC	4.8	1.001	2.205	2.39	2.53	2.57	9.29
35-1112	1	AC	5.05	1.015	2.31	2.577	-	2.807	10.1
37-1024	1	AC	5.1	1.01	2.288	2.515	2.821	2.736	14.02
37-1802	1	AC	6.35	1.01	2.08	2.361	2.66	2.596	14.87
	2	AC	4.8	1.01	2.215	2.467	2.66	2.66	10.53
40-4087	1	AC	4.75	0.995	2.391	2.496	2.710	2.698	11.77
	2	ATB	4.50	1.010	2.373	2.498	2.723	2.684	11.77
40-4165	1	AC	4.45	1.029	2.262	2.483	-	2.658	8.90
	2	AC	3.88	1.029	2.260	2.530	-	2.689	7.77
42-1599	1	AC	7	1.024	2.246	2.552	2.739	2.875	11.75
	2	AC	3.93	1.024	2.294	2.26	2.754	2.761	8.65
45-1011	1	AC	4.4	1.032	2.391	2.488	2.717	2.66	11.99
47-3104	1	AC	5.6	1.02	2.196	2.481	2.65	2.711	10.29
48-1077	1	AC	4.8	0.985	2.249	2.443	-	2.64	9.6
	2	AC	4.35	0.985	2.303	2.45	2.614	2.628	9.73
48-1169	1	AC	5	1.028	-	-	-	-	10
48-1174	1	AC	5.3	1.01	-	-	-	-	10.6
	2	AC	6.26	1.01	1.914	2.213	-	2.403	12.5
48-3749	1	AC	6	1.028	2.121	2.266	2.402	2.454	10.62
48-9005	1	AC	4.7	1.024	2.162	2.402	-	2.573	9.4
50-1002	1	AC	5.95	1.01	2.338	2.456	2.664	2.701	12.65
	2	AC	3.8	1.01	2.484	2.597	2.806	2.769	10.49
53-1008	1	AC	5.8	1.01	2.389	2.506	2.745	2.757	13.37

Table B7. Original air voids and total unit weight

Section	Layer Number	Layer Type	MAAT (ºF)	Original Viscosity (MPoises)	Original Air Void (%)	Total Unit Weight (pcf)
01-1001	1	AC	64.91	1.36	8.92	147.26
	2	AC	94.91	1.36	10.19	147.26
01-1019	1	AC	65.5	1.89	8	150
	2	AC	65.54	1.89	8.51	150
	3	AC	65.5	1.89	10.74	142
01-4126	1	AC	59.77	1.36	9.16	137.03
	2	AC	59.77	1.36	11.23	146.33
02-1001	1	AC	37.03	0.33	8.11	149
02-1002	1	AC	37.4	0.22	7.3	149.48
04-0113	1	AC	-	-	9.77	142.77
04-0114	1	AC	-	-	9.77	138.4
04-1024	1	AC	53.3	0.93	11	151
09-1803	1	AC	50.5	2.28	9.96	149
	2	AC	50.5	2.28	9	157
12-3995	1	AC	75.06	1.36	10.36	138.16
12-3997	1	AC	69.31	1.29	10.12	140
12-4107	1	AC	73.42	1.36	7.73	138.87
20-1009	1	AC	56.03	1.36	8.16	145.27
	2	AC	56.03	1.36	10.17	143.4
25-1003	1	AC	49.33	1.36	7.92	148.76
	2	AC	49.33	1.36	11.44	146.32
26-1001	1	AC	43.54	0.62	9.95	149.17
27-1087	1	AC	45.4	1.33	10.39	147.83
29-1008	1	AC	57.64	2.24	6	152.82
	2	AC	57.64	2.24	6.41	148.79
34-1031	1	AC	54.5	1.36	8.5	152.99
	2	AC	54.5	1.36	8.07	156.46
35-0101	1	AC	-	-	7.73	142.4
35-1112	1	AC	60.84	1.09	10.37	150
37-1024	1	AC	56.41	2.01	9	150
37-1802	1	AC	58.2	1.06	11.92	141
	2	AC	58.2	1.06	10.2	144
40-4087	1	AC	62.44	1.36	8.01	149.19
	2	ATB	62.44	1.36	9.36	148.1
40-4165	1	AC	58.7	2.07	8.92	147
	2	AC	58.7	2.07	10.69	147
42-1599	1	AC	45.29	1.68	12	145
	2	AC	45.29	1.68	11.34	163
45-1011	1	AC	66.2	1.36	8.09	149.19
47-3104	1	AC	56.18	2.8	11.48	143
48-1077	1	AC	61.44	.68	7.93	149
	2	AC	61.44	2.61	6	149
48-1169	1	AC	-	2.07	8	147
48-1174	1	AC	-	0.8	9	147
	2	AC	71.63	0.8	13.5	121
48-3749	1	AC	71.78	0.76	10.44	132.35
48-9005	1	AC	-	0.63	10	139
50-1002	1	AC	52.04	1.36	8.71	145.89
	2	AC	52.04	1.36	11.02	154.98
53-1008	1	AC	47.36	0.76	9.13	149.07

Table B8. Asphalt binder grade data (NCHRP 2004)

Section	Layer Number	Layer Type	Viscosity Grade	Pen Grade	Pen 77 ºF	Visc 140 ºF (Poises)	Visc 275 ºF (cStokes)
01-1001	1 2	AC AC	AC-20 AC-20	-	79 76	1993 2043	369 375
01-1019	1 2 3	AC AC AC	AC-20 AC-20 AC-20	-	75 75 75	1997 1997 1997	400 400 400
01-4126	1 2	AC AC	AC-20 AC-20	-	-	-	-
02-1001	1	AC	AC-5	-	163	436	172
02-1002	1	AC	AC-2.5	-	225	288	140
04-0113	1	AC	AC-30	-	36	9761	699.8
04-0114	1	AC	AC-30	-	36	9761	699.8
04-1024	1	AC	-	Pen 85-100	103	944	-
09-1803	1 2	AC AC	-	Pen 60-70 Pen 60-70	69 69	2052 2052	-
12-3995	1	AC	AC-20	-	-	-	-
12-3997	1	AC	-	Pen 85-100	89	1690	-
12-4107	1	AC	AC-20	-	-	-	-
20-1009	1 2	AC AC	AC-20 AC-20	-	-	-	-
25-1003	1 2	AC AC	AC-20 AC-20	-	-	-	-
26-1001	1	AC	-	Pen 120-150	-	-	-
27-1087	1	AC	-	Pen 85-100	-	-	-
29-1008	1 2	AC AC	-	Pen 60-70 Pen 60-70	-	-	-
34-1031	1 2	AC AC	AC-20 AC-20	-	-	-	-
35-0101	1	AC	AC-20	-	56	2793	472
35-1112	1	AC	-	Pen 85-100	96	-	-
37-1024	1	AC	AC-20	-	73	1788	414
37-1802	1 2	AC AC	AC-20 AC-20	-	97 97	2051 2051	683.4 683.4
40-4087	1 2	AC ATB	AC-203 AC-20	-	-	-	-
40-4165	1 2	AC AC	AC-20 AC-20	-	72 72	2233 2233	465 -
42-1599	1 2	AC AC	AC-20 AC-20	-	79 79	2037 2037	452 452
45-1011	1	AC	AC-20	-	-	-	-
47-3104	1	AC	AC-20	-	63	1977	-
48-1077	1 2	AC AC	AC-20 AC-20	-	118 65	1016 2265	590 -
48-1169	1	AC	AC-20	-	72	1870	464
48-1174	1 2	AC AC	AC-10 AC-10	-	110 110	995 995	255 255
48-3749	1	AC	AC-10	-	-	-	-
48-9005	1	AC	AC-10	-	122	1107	280
50-1002	1 2	AC AC	-	Pen 85-100 Pen 85-100	92 92	1144 1144	308 308
53-1008	1	AC	AC-10	-	83	30662	504

Table B9. Unbound materials data

Section	Layer Num	Layer Type	Dry Thermal Conductivity (BTU/hr-ft-°F)	Heat Capacity (BTU/lb-°F)	Liquid Limit (LL)	Plastic Limit (PL)	Plasticity Index (PI)	% Passing #200 Sieve	% Passing #4 Sieve	D_{60} (mm)
01-1001	3	GB	0.30	0.17	0	0	0	9.7	46.5	8.37
	4	GS	0.27	0.17	0	0	0	12.9	63	2.7
	5	SS	0.23	0.17	25	18	7	24.1	76	0.9
01-1019	4	GB	0.27	0.17	0	0	0	14	58	5.05
	5	SS	0.23	0.17	17	15	2	28	98	0.24
	6	BR	0.60	0.20	-	-	0	0	0	1
01-4126	3	GB	0.23	0.17	0	0	0	14.3	59	4.84
	4	SS	0.23	0.17	10.5	9.5	1	29.9	92	0.21
	5	BR	0.60	0.20	0	0	-	0	0	1
02-1001	2	GB	0.3	0.17	0	0	0	9	51	6.22
	3	SS	0.3	0.17	0	0	0	11	50	7.67
02-1002	2	GB	0.3	0.17	0	0	0	7	50	6.63
	3	GS	0.3	0.17	0	0	0	3.9	30	25.44
	4	SS	0.3	0.17	0	0	0	7.6	46	9.96
04-0113	2	GB	0.30	0.17	21	21	0	10.0	57.0	5.61
	3	SS	0.27	0.17	0	0	0	9.0	77.0	2.25
04-0114	2	GB	0.30	0.17	21	21	0	10.0	57.0	5.61
	3	SS	0.23	0.17	24	17	7	18.0	64.05	3.94
04-1024	2	GB	0.22	0.17	28	12	16	11.0	34.0	14.30
	3	SS	0.22	0.17	-	-	22	30.0	72.0	1.15
09-1803	3	GB	0.30	0.17	0	0	0	8	56	5.75
	4	SS	0.23	0.17	0	0	0	12.6	90	0.48
12-3995	2	GB	0.30	0.17	0	0	0	7.6	55.5	4.86
	3	GS	0.30	0.17	0	0	0	6.4	86.5	0.4
	4	SS	0.30	0.17	0	0	0	1.8	99.5	0.27
12-3997	2	GB	0.27	0.17	0	0	0	21	70	1.82
	3	GS	0.23	0.17	0	0	0	12	87	0.13
	4	SS	0.3	0.17	0	0	0	9	99	0.15
12-4107	2	GB	0.27	0.17	0	0	0	8.8	64.5	2.50
	3	SS	0..27	0.17	0	0	0	11.4	99.0	0.29
20-1009	3	SS	0.27	0.17	21	17.5	3.5	30.7	100.0	0.22
25-1003	3	GB	0.27	0.17	0	0	0	8.6	72.5	2.04
	4	SS	0.27	0.17	0	0	0	20.5	68	2.14
	5	BR	0.6	0.2	-	-	-	0	0	1
26-1001	2	GB	0.27	0.17	0	0	0	6.3	58.5	5
	3	SS	0.27	0.17	0	0	0	4	98	0.34
27-1087	2	SS	0.27	0.17	0	0	0	26.4	95.5	0.26
29-1008	3	GB	0.27	0.17	0	0	0	14.4	61	4.1
	4	SS	0.27	0.17	27	16	11	37.8	67	1.2
34-1031	3	GB	0.27	0.17	25	19	6	9.3	75	1.8
	4	SS	0.27	0.17	0	0	0	6.9	92	0.73
35-0101	2	GB	0.3	0.17	0	1	0	5	55	5.1
	3	SS	0.18	0.17	40	18	27	69	93	0.07
35-1112	2	GB	0.27	0.17	23.5	18	5.5	17	70	1.96
	3	SS	0.3	0.17	0	0	0	3	100	0.17
37-1024	2	GB	0.23	0.17	0	0	0	27	48	9.88
	3	SS	0.22	0.17	38	26	12	35	95	0.27
37-1802	3	GB	0.3	0.17	0	0	0	10	52	7.24
	4	SS	0.12	0.17	44.5	28	16.5	57	92	0.12

Table B9. Unbound materials data (Contd.)

40-4087	4	SS	0.12	0.17	44	23	21	88.6	100.0	0.07
40-4165	3	SS	0.23	0.17	0	0	0	29.0	100.0	0.18
42-1599	3	GB	0.3	0.17	16	15	1	12	38	8.63
	4	SS	0.22	0.17	26.5	20.5	6	48	67	1.50
	5	BR	0.60	0.2	-	-	-	0	0	1
45-1011	2	GB	0.27	0.17	0	0	0	21.3	67	2.5
	3	SS	0.23	0.17	0	0	0	16.3	98	0.14
47-3104	2	GB	0.27	0.17	0	0	0	16	48	8.45
	3	SS	0.22	0.17	30.5	20.5	10	58	86	0.09
	4	BR	0.6	0.2	-	-	-	0	0	1
48-1077	3	GB	0.30	0.17	0	0	0	8.0	45.0	10.05
	4	SS	0.22	0.17	0	0	0	63.0	96.0	0.07
48-1169	2	GB	0.23	0.17	0	0	0	27.0	83.0	0.39
	3	SS	0.30	0.17	0	0	0	3.0	100.0	0.20
	4	BR	0.60	0.20	-	-	-	0.0	0.0	1.0
48-1174	3	GB	0.30	0.17	0	0	0	14.0	59.0	4.74
	4	SS	0.12	0.17	55	21.5	33.5	64.0	100.0	0.07
48-3749	2	GB	0.27	0.17	0	0	0	17.8	78.0	1.10
	3	TS	0.12	0.17	40.7	20.5	20.2	49.0	99.0	0.11
	4	SS	0.12	0.17	42	18	24	49.0	99.0	0.11
48-9005	2	GB	0.22	0.17	25	16	9	42.0	74.0	1.75
	3	SS	0.12	0.17	57.5	26.5	31	64.0	80.0	0.07
	4	BR	0.60	0.20	-	-	-	0.0	0.0	1.00
50-1002	3	GB	0.3	0.17	0	0	0	3.3	18	23.54
	4	SS	0.3	0.17	0	0	0	7.0	48	7.74
53-1008	2	GB	0.3	0.17	0	0	0	3.6	50.5	6.04
	3	GS	0.3	0.17	0	0	0	8.6	53.5	5.54
	4	SS	0.3	0.17	22	17	5	8.6	43.5	9.89

Table B10. Unbound materials data

Section	Max. Dry Unit Weight (pcf)	Specific Gravity	AASHTO Class	Ext. Resilient Modulus (psi)
01-1001	139 137.5 121	2 2.65 2.7	A-1-a A-1-b A-2-4	40000 38000 32000
01-1019	-	2.65 2.68 2.6	A-1-b A-2-4 -	38000 32000 750000
01-4126	134 122 -	2.65 2.68 2.6	A-2-4 A-2-4 -	32000 32000 750000
02-1001	-	2.65 2.65	A-1-a A-1-a	40000 40000
02-1002	142 146 141	2.65 2.65 2.65	A-1-a A-1-a A-1-a	40000 40000 40000
04-0113	-	2.65 2.65	A-1-b A-1-a	40000 32000
04-0114	-	2.65 2.69	A-2-4 A-1-a	40000 32000
04-1024	-	2.7 2.72	A-1-b A-26	25500 25500
09-1803	-	2.65 2.65	A-1-a A-2-4	40000 32000
12-3995	130 112 107	2.65 2.65 2.65	A-1-a A-3 A-3	40000 29000 29000
12-3997	-	2.65 2.65 2.65	A-1-b A-2-4 A-3	38000 32000 29000
12-4107	129 118.5	2.65 2.65	A-1-b A-2-4	38000 32000
20-1009	119.5	2.69	A-2-4	32000
25-1003	133.5 128 -	2.65 2.65 2.6	A-1-a A-1-b -	40000 38000 750000
26-1001	138.5 111	2.65 2.65	A-1-a A-3	40000 29000
27-1087	129.5	2.65	A-2-4	32000
29-1008	142.5 124	2.65 2.71	A-1-a A-2-6	40000 17000
34-1031	130.5 124	2.68 2.65	A-2-4 A-1-b	32000 38000
35-0101	-	2.65 2.74	A-2-6 A-1-a	40000 17000
35-1112	-	2.69 2.65	A-1-b A-3	38000 29000
37-1024	-	2.65 2.71	A-2-4 A-2-6	32000 25500
37-1802	-	2.65 2.73	A-1-a A-7-6	40000 8000

Table B10. Unbound materials data (Contd.)

40-4087	108	2.75	A-7-6	8000
40-4165	-	2.65	A-2-4	32000
42-1599	-	2.67 2.71 2.6	A-1-a A-4 -	40000 24000 750000
45-1011	127.5 110	2.65 2.65	A-1-b A-2-4	38000 32000
47-3104	-	2.65 2.72 2.6	A-1-b A-4 -	38000 24000 750000
48-1077	-	2.65 2.65	A-1-a A-4	40000 24000
48-1169	-	2.65 2.65 2.6	A-2-4 A-3 -	32000 29000 750000
48-1174	133.5 103 100	2.65 2.74 2.75	A-1-b A-7-6 A-7-6	38000 8000 8000
48-3749	109.5 106.5 106.5	2.65 2.73 2.73	A-1-b A-7-6 A-7-6	38000 8000 8000
48-9005	-	2.71 2.75 2.6	A-4 A-7-6 -	24000 8000 750000
50-1002	-	2.65 2.65	A-1-a A-1-a	40000 40000
53-1008	146 149.5 125	2.65 2.65 2.63	A-1-a A-1-a A-1-a	40000 40000 40000

APPENDIX C

MEASURED AND PREDICTED ALLIGAOTR CRACKING DATA

The measured, the AASHTOWare Predicted and the AASHTOWare Predicted alligator cracking data including the thermal fatigue are presented in Table C1.

Table C1. Alligator cracking data

Section	Date	Measured Cracking (%)	AASHTOWare Predicted Cracking (%)	Including thermal fatigue with AASHTOWare Predicted Cracking (%)
48-1169	2/26/1990	0	2.40	0.0137
	3/4/1990	0	2.43	0.0138
	9/18/1990	0	2.59	0.0151
	1/16/1991	0	2.74	0.0160
	3/7/1991	0	2.81	0.0164
	6/25/1991	0	2.89	0.0171
	1/30/1992	0	3.40	0.0192
	2/27/1993	0	4.53	0.0234
	8/11/1993	0	4.96	0.0251
	3/3/1995	0	7.39	0.0327
	7/19/1995	0	7.94	0.0347
	7/15/1997	0	11.93	0.0483
	5/27/1999	1.42	12.83	0.0579
48-9005	2/17/1993	2.0983	2.34	0.0022
	4/5/1993	2.4217	3.95	0.0034
	2/20/1995	3.6767	5.49	0.0045
	2/16/1996	4.0717	13.04	0.0104
	7/9/1996	5.0400	13.62	0.0112
	7/2/1997	0.0000	17.43	0.0277
	7/10/1998	7.7850	17.83	0.0404
48-1174	4/10/1991	0.2683	2.12	4.7366
	3/26/1992	0.0000	2.21	5.0623
	2/18/1993	0.6267	2.31	5.3792
	3/31/1993	1.5950	2.49	5.5074
	2/21/1995	2.0617	2.97	6.1972
	3/21/1995	3.8733	2.99	6.2253
	1/12/1996	6.4383	3.32	6.5268
	4/22/1997	14.7450	3.89	6.9844
	3/20/1998	0.2683	2.12	4.7366

Table C1. Alligator cracking data (contd.)

Section	Date	Measured Cracking (%)	AASHTOWare Predicted Cracking (%)	Including thermal fatigue with AASHTOWare Predicted Cracking (%)
48-3749	4/9/1991	0	7.94	0.2162
	8/29/1991	0	7.94	0.2192
	3/16/1992	0	9.06	0.2332
	2/16/1993	0	9.72	0.2426
	2/21/1993	0	10.80	0.2614
	3/31/1993	0	12.67	0.2959
	2/21/1995	3.8033	14.88	0.3552
	3/21/1995	5.9200	14.88	0.3555
	3/28/1997	7.9700	15.07	0.3625
04-0113	2/21/1995	0	1.75	1.5988
	3/30/1995	0	1.77	1.7143
	8/17/1995	0	1.92	2.2680
	11/8/1995	0	2.00	2.5787
	2/7/1996	0	2.04	2.8633
	4/3/1996	0	2.10	3.0722
	7/10/1996	0	2.29	3.4806
	8/14/1996	0	2.38	3.6266
	1/8/1998	0	4.60	5.5878
	1/13/1998	0	4.60	5.6024
	4/20/1998	0.1617	5.16	5.9482
	6/11/1998	0.3233	6.25	6.2038
	10/22/1998	0.4850	8.56	6.7736
	2/16/1999	1.0950	9.35	7.1730
	1/13/2000	1.5617	12.09	8.3406
04-0114	2/15/1995	0	1.60	1.3565
	3/30/1995	0	1.60	1.4767
	8/17/1995	0	1.67	1.9303
	11/7/1995	0	1.70	2.1881
	2/6/1996	0	1.71	2.4525
	4/2/1996	0	1.72	2.6280
	7/9/1996	0	1.78	2.9673
	8/13/1996	0	1.80	3.0898
	1/7/1998	0	1.97	4.7804
	4/21/1998	0.7717	1.98	5.1127
	6/12/1998	1.6333	2.03	5.3097
	10/23/1998	3.5350	2.10	5.7823
	2/12/1999	7.9117	2.11	6.1385
	1/13/2000	9.1317	2.27	7.2967

Table C1. Alligator cracking data (contd.)

Section	Date	Measured Cracking (%)	AASHTOWare Predicted Cracking (%)	Including thermal fatigue with AASHTOWare Predicted Cracking (%)
04-0115	2/15/1995	0.0000	1.45	4.1355
	3/30/1995	0.4133	1.45	4.1634
	1/7/1998	0.4133	1.45	4.8198
	2/11/1999	0.4133	1.45	5.0776
	1/12/2000	0.4133	1.45	5.2927
04-1007	9/20/1991	0.6283	1.55	5.4524
	2/2/1993	1.6333	1.63	6.1764
	9/16/1994	5.0067	1.75	7.0674
04-1024	11/3/1989	0	2.48	3.1240
	8/26/1990	0	2.61	3.6246
	10/29/1992	0	3.08	4.2913
	3/28/1995	0	3.86	4.9916
	7/17/1995	0	4.09	5.0986
	8/22/1995	0.1967	4.21	5.1418
	11/9/1995	0.1617	4.39	5.2156
	4/4/1996	0.2683	4.48	5.3090
	6/13/1996	1.9733	4.68	5.3781
	8/15/1996	2.6917	5.06	5.4675
	4/22/1998	15.4467	6.54	5.9660
	6/15/1998	15.4467	6.94	6.0342
	10/26/1998	15.7150	7.89	6.1914
40-4087	1/17/1990	0	1.45	0.8902
	10/13/1991	0	1.45	1.7160
	10/15/1991	0	1.45	1.7189
	11/6/1992	0	1.45	2.3187
	2/8/1993	0	1.45	2.4737
	11/3/1994	0	1.45	3.6062
	2/9/1995	0.5383	1.45	3.7945
	6/18/1997	5.0950	1.45	5.5751
40-4165	10/13/1994	0.0533	1.63	4.1391
	4/18/1995	0.1067	1.63	4.3413
	6/20/1995	0.1600	1.64	4.4149
	4/22/1996	0	1.66	4.7615
	11/8/1996	0	1.68	4.9990
	5/23/1997	0.6983	1.68	5.2123

Table C1. Alligator cracking data (contd.)

Section	Date	Measured Cracking (%)	AASHTOWare Predicted Cracking (%)	Including thermal fatigue with AASHTOWare Predicted Cracking (%)
01-1001	9/2/1991	0.1250	1.74	2.0669
	4/2/1992	0.3400	1.77	2.2056
	7/24/1992	0.5550	1.79	2.2916
	1/15/1993	1.3083	1.83	2.4225
01-1019	5/15/1989	0.0000	1.46	3.7102
	4/16/1990	0.0000	1.47	5.0865
	1/15/1991	0.0000	1.47	6.2062
	6/19/1991	13.3300	1.47	6.8358
	3/31/1992	13.3300	1.48	7.9890
	3/29/1993	18.5317	1.48	9.4351
01-4126	6/5/1989	0	1.45	1.8574
	3/3/1991	0	1.45	4.7002
02-1001	5/31/1990	0	1.45	0.1941
	8/21/1991	0	1.45	0.2430
	8/26/1993	0	1.45	0.3294
	6/15/1995	0	1.45	0.4123
	8/22/1997	0	1.45	0.5198
	8/26/1998	0.0533	1.45	0.5715
	6/24/1999	2.7983	1.45	0.6147
02-1002	5/30/1990	0	1.45	0.2007
	8/22/1991	0.1033	1.45	0.2606
	8/25/1993	0.1033	1.45	0.3649
	6/14/1995	0.1033	1.45	0.4646
	8/21/1997	0.1033	1.45	0.5940
	5/14/1998	0.1033	1.45	0.6378
47-3104	8/23/1989	1.2383	1.46	0.0015
	11/1/1989	1.2383	1.46	0.0017
	5/6/1991	2.1000	1.62	0.0050
	8/13/1991	9.6167	1.66	0.0056
50-1002	8/17/1994	5.0950	1.45	10.9953
	4/27/1995	11.5350	1.45	11.7344
	10/17/1996	13.1317	1.45	14.3218
	5/15/1997	11.9483	1.45	14.9550
	10/23/1997	17.9933	1.45	16.2508
	6/9/1998	25.1517	1.45	16.6811

Table C1. Alligator cracking data (contd.)

Section	Date	Measured Cracking (%)	AASHTOWare Predicted Cracking (%)	Including thermal fatigue with AASHTOWare Predicted Cracking (%)
35-0101	5/1/1997	0	1.45	1.5068
	3/19/1999	0	1.45	3.5767
	10/8/1999	0	1.46	4.1962
35-1112	12/5/1989	0	1.49	4.0905
	1/22/1991	0	1.50	4.9781
	3/27/1991	0	1.51	5.1145
09-1803	7/31/1989	0	1.45	1.1658
	9/5/1990	0	1.45	1.5059
	8/22/1991	0	1.45	1.8068
	9/30/1992	0.1250	1.45	2.1568
	5/12/1994	3.6417	1.45	2.6696
	5/25/1995	7.6417	1.46	3.0009
	10/8/1996	10.4050	1.46	3.4428
37-1802	3/10/1991	0.5917	1.70	3.7295
	10/10/1992	2.0267	1.83	5.0177
26-1001	7/19/1988	0	1.45	5.5620
	9/7/1989	0	1.45	6.1620
	7/21/1990	0	1.45	6.6324
	7/16/1991	0.5567	1.45	7.1790
	9/27/1991	1.0233	1.45	7.2934
	9/1/1992	1.6867	1.45	7.8228
	6/7/1993	3.0317	1.45	8.2640
	6/9/1993	4.3050	1.45	8.2672
	5/12/1995	5.2733	1.45	9.4047
	7/5/1996	6.6550	1.45	10.1023
	8/5/1999	7.4450	1.45	12.0187
12-3997	8/15/1990	0.7717	1.57	8.9334
	10/4/1991	1.3450	1.59	9.6055
	3/8/1993	19.0883	1.60	10.4486
34-1031	4/6/1992	4.8617	1.49	2.6772
25-1003	8/4/1989	0	1.45	4.7871
	9/6/1990	0	1.45	5.1532
	8/23/1991	0.4667	1.46	5.4757
	9/30/1992	2.9417	1.46	5.8469
	10/27/1995	4.9517	1.47	6.8739
53-1008	7/4/1991	0.5567	1.51	6.3723
	6/28/1993	1.4717	1.53	7.6000
	6/16/1994	17.9400	1.54	8.2102

Table C1. Alligator cracking data (contd.)

Section	Date	Measured Cracking (%)	AASHTOWare Predicted Cracking (%)	Including thermal fatigue with AASHTOWare Predicted Cracking (%)
45-1011	3/18/1992	0	6.18	2.4092
	10/24/1992	0	9.11	2.7388
27-1087	10/25/1991	0	1.45	1.8712
	5/11/1993	0	1.45	2.1202
	10/5/1994	0.0533	1.45	2.3465
	6/25/1996	0.2683	1.45	2.6245
	8/3/1999	2.1167	1.45	3.1255
	9/4/2000	2.6550	1.45	3.3011
29-1008	2/16/1992	0.6817	1.62	0.6020
	3/5/1993	3.3733	1.65	0.7174
	3/26/1993	6.0650	1.65	0.7218
	3/29/1993	6.0650	1.65	0.7225
	4/17/1996	6.0650	1.75	1.0713
	2/1/2000	6.0650	1.92	1.5487
	2/16/1992	0.0000	1.45	7.5114
42-1599	8/29/1989	1.0950	1.45	1.6205
	9/27/1990	0	1.45	2.4983
	3/1/1993	0	1.45	4.4710
	9/1/1994	0	1.45	5.6798
	6/21/1995	0	1.45	6.3182
	7/19/1996	0	1.45	7.1692
	3/26/1998	0.1433	1.45	8.4778
37-1024	11/3/1989	2.7800	1.49	5.7470
12-4107	12/6/1989	0	1.45	0.7664
	2/5/1991	0	1.45	0.9838
	7/18/1991	0	1.45	1.0714
12-3995	4/15/1992	0	2.11	2.8387
	3/9/1994	1.4350	2.29	3.2483
	1/17/1996	2.4033	2.56	3.6699
	1/21/1996	4.4300	2.56	3.6715

APPENDIX D

DETERMINING THERMAL PROPERTIES OF ASPHALT CONCRETE

Several thermal properties such as thermal conductivity (k) and specific heat capacity (C) are needed in the AASHTOWare Pavement ME Design Software as inputs to predict pavement distresses such as thermal cracking and aging. The determination of the parameters, k and C are discussed herein. In addition, a Finite Element Model (FEM) was also developed to determine the temperature variation at any depth of AC which is described. It is mentionable that the FEM method was not used in the study to predict the temperature fluctuation at the bottom of AC; rather, the regression models discussed in the main body were used.

DETERMINATION OF *C* IN THE LABORATORY

Laboratory Testing

A foam ice box was used as a calorimeter as shown in Fig. D1. This box was considered to be thermally insulator material. To confirm, hot water of 50.5 °C was kept inside the box and the temperature was monitored for 3 hours with a thermometer inserted into the box. The decrease in temperature was measured to be 1.9 °C per hour (≈ 0.1 °C per three minutes) in first hour and 1.7 and 1.6 °C for the second and the third hour respectively. Then, hot water of 50.5 °C was taken and the mass of water was measured carefully. A cylindrical sample was prepared and cut into small pieces in the laboratory. The same mixture of the instrumented section was used to prepare the sample. Details of sample

preparation are described in next section. The weight of these cut samples were measured and the body temperature was recorded. Prior to measuring the temperature, the samples were conditioned in room temperature for at least 24 hours. Then sample was then immersed in water very quickly and the bowl was covered. One thermometer was inserted into the box to measure the sample-water temperature. Then, the decrease in temperature was monitored to determine the stable temperature.

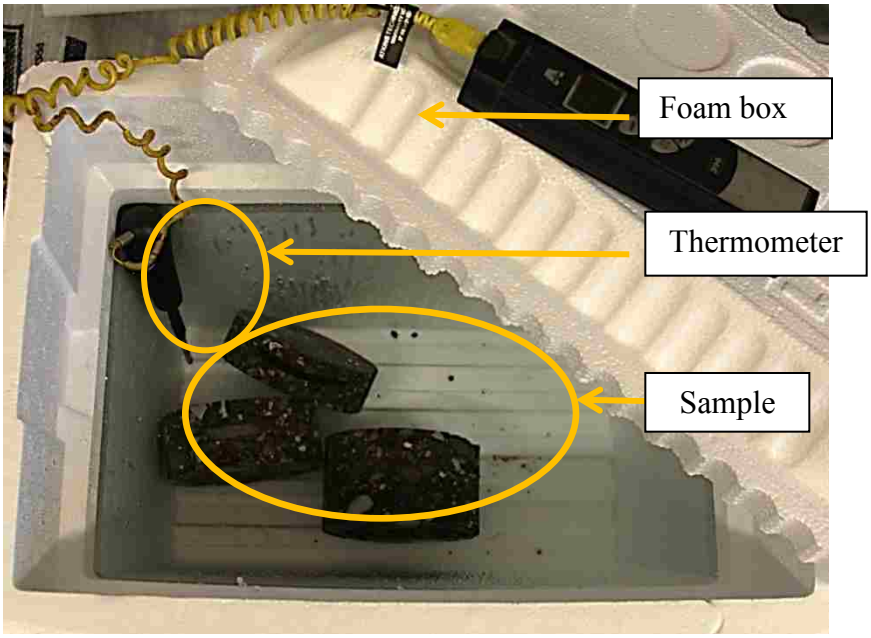

Figure D1. Test setup for determining the *C* of the AC

Calculation for determining the C

The test was stopped when the temperature reached to a stable condition. It took 42 minutes to reach to the stable position. Even though, the test was continued up to 1 hour to ensure the accuracy of reading. The heat loss of 1.9 °C was compensated for

calculating the final stable temperature. Then, using Eq. D1 the C value of the AC was determined.

$$C = \frac{m_w C_w (\theta_w - \theta_f)}{m_{AC} (\theta_f - \theta_{AC})} \tag{D1}$$

where m_w, C_w and θ_w are the mass, specific heat capacity and initial temperature of water, m_{AC}, θ_{AC} are the mass and initial temperature of the AC respectively and θ_f is the final temperature of the mix. In this test, 2.525 kg of AC of 20.6 °C was mixed with the 4.019 kg of water of 50.1 °C. The final temperature was 44.8 °C after applying the temperature correction. The laboratory C of the AC is measured to be 1464 J/(kgK).

DETERMINATION OF THE *k*

The k value was determined through FEM analysis using laboratory data. Thermal gradient was applied in a cylindrical sample in the laboratory. Increase in temperature with time at the colder end of the sample was recorded. Based on the laboratory determined C value a FEM model was developed for the cylindrical sample and k value is assigned on trial and error basis. The increase in temperature at the colder end of the model sample was compared with the increase in temperature of the laboratory sample to determine the optimum k value. Using k and C values in FEM, field AC temperatures at 90 mm depth were predicted from morning to afternoon and compared with measured values.

Sample Preparation

Some plant mix was collected from the instrumentation construction site in corporation with the NMDOT. The mix was compacted to prepare a 150 mm diameter and 170 mm height cylindrical sample using a gyratory compactor at 150 °C. Prior to the compaction a steel pin was inserted up to 70 mm depth at the top of it. The pin was carefully pulled out just after the compaction. No pin was inserted in the sample which was prepared to determine the *C* value. The sample was then cored into a 100 mm diameter sample using laboratory coring tool and the two edges remained uncut to avoid the cut edge effect. The air void and density of both samples were measured to be 4.3%. Prior to the testing, the sample was oven dried for 24 hours at 40 °C.

Laboratory Testing

The sample was covered with felt, an insulating material, as shown in Fig. D2. This insures no loss and gain of heat through the curved surfaces. Such a boundary condition represents the field condition, one-dimensional vertical downward flow. One end of the sample was immersed in hot water in a constant water temperature bath. The other end of the beam was kept open for heat convection to air to simulate heat flow or transmission of AC layer to the base layer in a pavement. Specifically, the top surface of the beam was kept open for heat convection to the laboratory air.

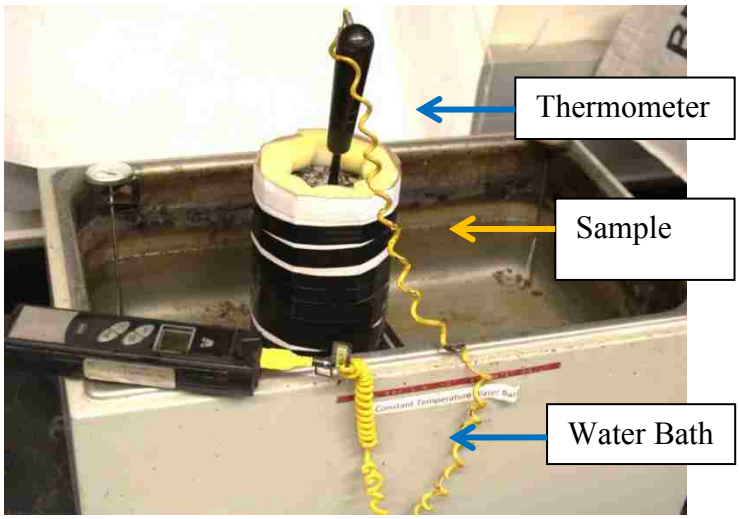

Fig. D2. Testing the sample for measuring temperature increase at the colder end

The temperature of the hot water was stabilized before placing the specimen. A thermometer was inserted replacing the steel pin. The temperature of the hot water was maintained 43.1 °C and the laboratory air temperature was 22.5 °C, a total temperature differential of 20.6 °C. The increase in temperature at the colder end of the beam was recorded every 15 minutes. This test data was used to compare with FEM output for determining the k value of the asphalt concrete.

Determination of k using FEM

The *C* value was determined in the laboratory and used as a input in FEM. The *k* value was assigned as trial and error basis and the laboratory measured temperature was matched with FEM results to obtain the optimum *k*. A three-dimensional FEM was developed in commercial finite element software, ANSYS. In the FEM analysis, the one dimensional transient heat transfer analysis is conducted. This method uses the basic transient heat transfer Fourier Equation (Eq. D2).

$$k\frac{\partial^2 T}{\partial x^2} = \rho C\frac{\partial T}{\partial t} \tag{D2}$$

where: *k*, *C* and ρ are the thermal conductivity, specific heat capacity and density of the AC respectively. *T, t* and *x* denote temperature, time and the length of the sample respectively. Carslaw and Jaeger (1959) derived the analytical solution of this partial equation and is given as in Eq. D3:

$$T(x,t) = \frac{4}{\pi}\sum_{n=1}^{\infty}\frac{1}{(2n+1)}\sin(2n+1)\pi x e^{-\sigma(2n+1)^2\pi^2 t} \tag{D3}$$

where *n* is the number steps required for the convergence, i.e., 1, 2, 3 and so on, σ is the thermal diffusivity (m^2/s). A solid cylinder of 100 mm diameter and 90 mm height was modeled. The laboratory sample height was 170 mm but the thermometer was inserted at 90 mm depth. Therefore, the effective length of the sample was 90 mm. A linear thermal property was assumed for asphalt concrete. A solid 87 element, readily available in

ANSYS, was used to idealize an AC element. The solid 70 and solid 90 elements were also evaluated and observed to be consistent, though SOLID 87 is finally used in this study. No heat convection was assumed at the curved surface. A temperature of 20.6 °C was applied on one edge and the other edge was kept at 0 °C to simulate the laboratory condition.

Several trails values of *k* were assigned in the FEM model. The optimum solution was obtained for the *k* value of 2.11 W/(mK). At the colder end, the increase in temperature was 1.39 °C after 30 minutes for maintaining 20.6 °C temperature at the hot end. Variations of the temperature for FEM and laboratory testing are shown in Fig. D3. The initial part of the plot has the exact match and with time it deviates a little. However, these *k* and *C* values were validated with the field measured data.

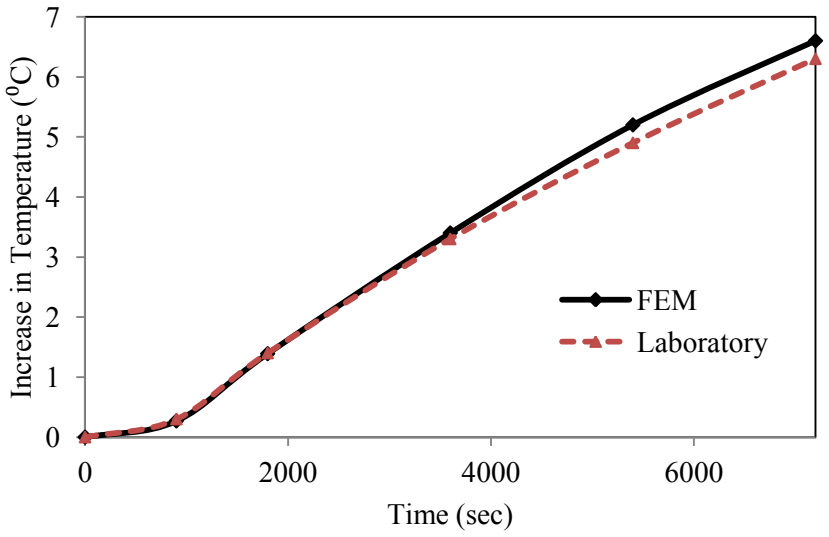

Fig. D3. Variations of temperature with time

VALIDATION OF LABORATORY *C* AND FEM *k* VALUES

Using the determined *k* and *C* values in FEM model the temperature at 90 mm depth of the AC was predicted. The predicted value was compared with measured temperature from morning to afternoon on October 16, 2012. The surface temperature was the minimum around 8:15 am and maximum around 3:15 pm; whereas these values were at 9:15 am and 4:45 pm respectively at 90 mm depth. The half an hourly surface temperature on the pavement was assumed constant. The increase in surface temperature form 8:15 am to 8:45 am was 0.56 °C as shown in Table D1.

This increase in temperature heated up the pavement material up to 8:45 am (30 minutes). Similarly, the increased in temperature from 8:45 am to 9:15 am (i.e. 1.31 °C) heated up the pavement up to 9:15 am. Similarly, all the half an hourly increase in temperature with reference to the 8:15 am temperature (minimum temperature) were calculated and durations of heating were considered 30 minutes.

When the temperature started to decrease after reaching the peak at 3:15 pm the increase (negative values) in temperature was calculated with reference to the temperature at 3:15 pm. This increase in temperature was assigned at one end of the modeled sample and the other end was maintained at 0 °C. The corresponding temperature increase at the colder end after 30 minutes was calculated and summed up with the minimum temperature at 90 mm depth (16.83 °C). The cumulative sum of the produced temperature was considered the predicted temperature at 90 mm depth. The predicted and the measured temperature at 90 mm depth are shown in Fig. D4. A promising agreement between these two values

was observed. Therefore, conclusion can be drawn that the simplified numerical analysis and the practice ready, low cost laboratory procedure measure the thermal properties accurately.

Table D1. Measured temperature at 90 mm depth on October 16, 2012

Time	Surface Temperature (°C)	Temperature Increase (°C)
08:15 am	12.92	0.00
08:45 am	13.48	0.56
09:15 am	14.23	1.31
09:45 am	16.66	3.73
10:15 am	19.51	6.58
10:45 am	21.44	8.52
11:15 am	23.26	10.33
11:45 pm	25.99	13.07
12:15 pm	28.50	15.58
12:45 pm	28.82	15.90
01:15 pm	30.44	17.52
01:45 pm	32.00	19.08
02:15 pm	33.28	20.36
02:45 pm	34.11	21.19
03:15 pm	34.50	21.58
03:45 pm	34.28	-0.22
04:15 pm	33.83	-0.67
04:45 pm	33.06	-1.44

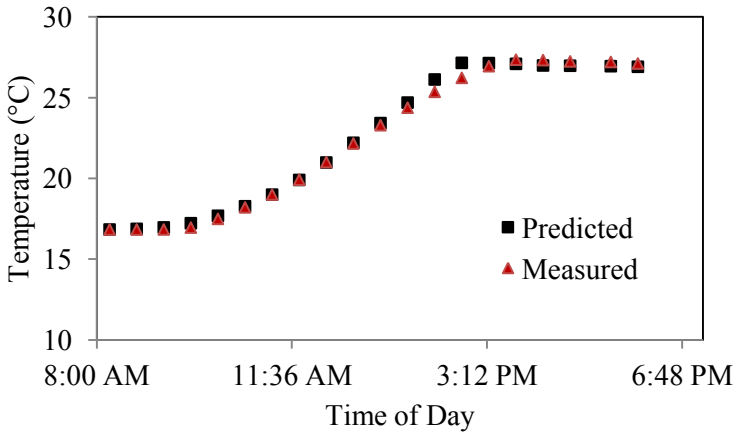

Fig. D4. Predicted and measured temperatures at 90 mm depth

CONCLUSIONS

This study determines thermal properties of AC using a single mixture. The results are presented in the study of Islam and Tarefder (2014d). Based on the current study the following conclusions can be made:

- The *C* value of the AC mixture used in the study is 1464 J/(kgK).
- This study also determines *k* value from FEM analysis using cylindrical sample using the laboratory determined *C* value; the resulted *k* value is 2.11 W/(mK).

BIOGRAPHY

Md Rashadul Islam was born in Bangladesh where he received his B.S. in Civil Engineering from the Bangladesh University of Engineering and Technology (BUET) in 2007. Dr. Islam obtained his M.S. from the University of Minho (Portugal) and the Technical University of Catalonia (Spain) in 2008. After then, Dr. Islam served as a Faculty of Civil Engineering in the Stamford University Bangladesh for two years. As of July 2015, Dr. Islam has authored/coauthored 32 journal articles, 7 special publications/book chapters, 27 articles in conferences, and 1 major research report. Dr. Islam's service to the civil engineering community includes being the members of TRB, ASCE, ACI, and ITE.